

DTIC FILE COPY

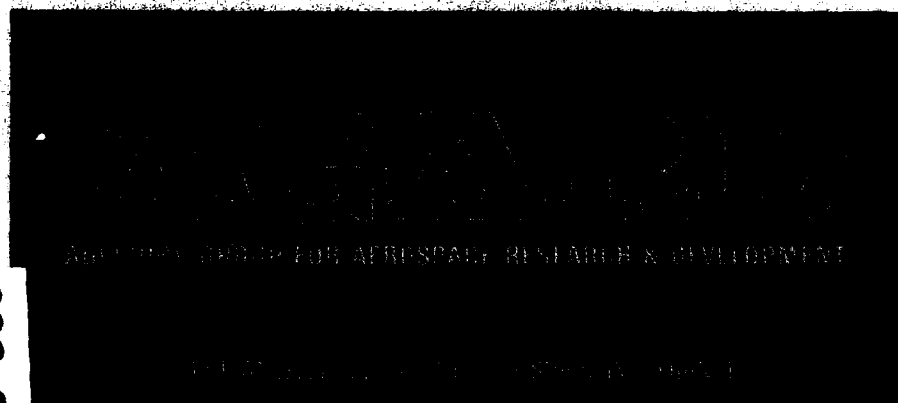
①

AGARD-AR-255

AGARD-AR-255

AD-A223 936

CALCULATION OF 3D SEPARATED TURBULENT FLOWS IN BOUNDARY LAYER LIMIT.



AGARD ADVISORY REPORT No.255

Fluid Dynamics Panel
Working Group 10

on

Calculation of 3D Separate Turbulent Flows in Boundary Layer Limit

(Le Calcul des Ecoulements Turbulents, Décollés
Tridimensionnels en Couche Limite)

DTIC
ELECT
JUN 28 1964
S Co B



DISTRIBUTION AND AVAILABILITY
ON BACK COVER

90 06 27 129

Approved for public release
Distribution Unlimited

NORTH ATLANTIC TREATY ORGANIZATION
ADVISORY GROUP FOR AEROSPACE RESEARCH AND DEVELOPMENT
(ORGANISATION DU TRAITE DE L'ATLANTIQUE NORD)

AGARD Advisory Report No.255

Report of the Fluid Dynamics Panel Working Group 10

Calculation of 3D Separated Turbulent Flows in Boundary Layer Limit

(Le Calcul des Ecoulements Turbulents Décollés
Tridimensionnels en Couche Limite)

This Advisory Report was prepared at the request of the Fluid Dynamics Panel of AGARD.

Document
Reproduced From
Best Available Copy

The Mission of AGARD

According to its Charter, the mission of AGARD is to bring together the leading personalities of the NATO nations in the fields of science and technology relating to aerospace for the following purposes:

- Recommending effective ways for the member nations to use their research and development capabilities for the common benefit of the NATO community;
- Providing scientific and technical advice and assistance to the Military Committee in the field of aerospace research and development (with particular regard to its military application);
- Continuously stimulating advances in the aerospace sciences relevant to strengthening the common defence posture;
- Improving the co-operation among member nations in aerospace research and development;
- Exchange of scientific and technical information;
- Providing assistance to member nations for the purpose of increasing their scientific and technical potential;
- Rendering scientific and technical assistance, as requested, to other NATO bodies and to member nations in connection with research and development problems in the aerospace field.

The highest authority within AGARD is the National Delegates Board consisting of officially appointed senior representatives from each member nation. The mission of AGARD is carried out through the Panels which are composed of experts appointed by the National Delegates, the Consultant and Exchange Programme and the Aerospace Applications Studies Programme. The results of AGARD work are reported to the member nations and the NATO Authorities through the AGARD series of publications of which this is one.

Participation in AGARD activities is by invitation only and is normally limited to citizens of the NATO nations.

The content of this publication has been reproduced directly from material supplied by AGARD or the authors.

Published May 1990

Copyright © AGARD 1990
All Rights Reserved

ISBN 92-835-0560-3



*Printed by Specialised Printing Services Limited
40 Chigwell Lane, Loughton, Essex IG10 3TZ*

Preface

Working Group No.10 of the AGARD Fluid Dynamics Panel (FDP) was formed to investigate the limits of boundary layer methods, both the integral and field type formulation, for the calculations of three-dimensional turbulent separate flows.

Since the first meeting in late 1985 various difficulties arose with regard to technical and organizational problems and the present report reflects this in some respect. However, it is hoped that the results presented give the reader sufficient inspiration to appreciate the work performed by the various members of the Working Group and their co-workers.

The participants' names are given below.

* * *

Le groupe de travail No.10 du Panel AGARD de la dynamique des fluides a été constitué pour examiner les limitations des méthodes de calcul appliquées à la couche limite, tant à formulation du type intégral que du type champ, pour le calcul des écoulements turbulents décollés tridimensionnels.

Depuis la première réunion, organisée vers la fin de l'année 1985, un certain nombre de problèmes d'ordre technique et logistique se sont posés et le présent rapport en témoigne dans une certaine mesure. Cependant, il est à espérer que les résultats qui y sont présentés permettront aux lecteurs de se rendre compte de l'amplitude des travaux entrepris par les différents membres du groupe et leurs collaborateurs.

La liste des participants s'établit comme suit:

J.Cousteix	France
C.Gleyzes	France
J.C.Le Balleur	France
E.H.Hirschel	Germany
H.-P.Kreplin	Germany
H.U.Meier	Germany
F.Menter	Germany
H.W.Stock	Germany
A.G.Panaras	Greece
D.Papailiou	Greece (FDP Member)
M.Onorato	Italy (FDP Member)
B. van den Berg	The Netherlands
J.I. van den Berg	The Netherlands
J.P.F.Lindhout	The Netherlands
H.Norstrud	Norway (FDP Member, Chairman)
A.Pagano	United Kingdom
P.D.Smith	United Kingdom
T.Cebeci	United States
L.Roberts	United States
J.Steger	United States
H.Yoshihara	United States
D.A.Humphreys	Sweden



Accession For	
NTIS GRA&I	<input checked="" type="checkbox"/>
DTIC TAB	<input type="checkbox"/>
Unannounced	<input type="checkbox"/>
Justification	
By _____	
Distribution/	
Availability Codes	
Dist	Avail and/or Special
A-1	

Contents

	Page
PREFACE	iii
1. BACKGROUND AND OVERVIEW	1
2. PHYSICAL ASPECTS OF 3D SEPARATED BOUNDARY LAYER FLOWS	4
2.1 Topological Features of Separated Flows	4
2.2 Turbulence Modelling of Separated Flows	6
3. THEORETICAL FORMULATION	10
4. NUMERICAL PROCEDURES	13
4.1 Integral Methods	13
4.1.1 The integral equations	13
4.1.2 Particular methods of solution	13
4.1.2.1 RAE method	14
4.1.2.2 RAE method using Cross's profiles	14
4.1.2.3 ONERA method	14
4.1.2.4 ONERA/CERT method	14
4.1.3 Numerical methods	15
4.2 Field Methods	16
4.2.1 Turbulence models	17
4.2.2 Numerical methods	19
4.2.3 Computational grids and computing effort	19
5. TEST CASE DATA BASE	22
5.1 Experimental	22
5.1.1 Description of the DFVLR prolate spheroid and its instrumentation	22
5.1.2 Lockheed/NASA-Ames Wing C	28
5.2 Thin-Layer Navier-Stokes Solution	34
6. RESULTS	51
6.1 Integral Methods	51
6.1.1 The ellipsoid at 10° incidence	51
6.2 Field Methods	73
6.2.1 The ellipsoid at 10° incidence	73
6.2.2 The C-wing	75
7. CONCLUSIONS	128
APPENDIX – NLR Calculations	129

CHAPTER 1. BACKGROUND AND OVERVIEW

H. Yoshihara, Office of Naval Research, Liaison Office,
Far East, APO San Francisco 96503-0007

1. INTRODUCTION

Flow separation plays a dominant role in the high lift performance of combat aircraft, invariably limiting takeoff and transonic maneuver performance. Such separations arise in two forms. The first is in the form of free shear layer separations which for example arises in the well known fashion along highly swept, sharp-nosed wings at large angles of attack. The second is the bubble-type separation where the separated flow is confined within the separation bubble as in the case of shock-induced separations on an unswept wing in the transonic regime. To treat such viscous vortical flows, it is essential that properly modeled viscous flow equations be used, which for relevant cases will be turbulent.

With the recent availability of vector supercomputers with their large speeds and memories, there has been impressive progress in computations using the Reynolds-averaged Navier/Stokes equations. Despite use of sophisticated algorithms programmed in effective vector formats, the computation costs have been so large as to preclude their use by the aerospace community. A viable affordable alternative is needed for design applications, and this is provided at large Reynolds numbers by the boundary layer procedure, either in the differential (field) or integral formulations.

In the boundary layer method the problem is divided into two parts, the boundary layer/wake and the equivalent inviscid flow. In the direct formulation the equivalent inviscid flow problem is first solved assuming the viscous effects to be negligible. The resultant surface pressure and flow direction distributions are then inputted into the turbulent equations simplified by the boundary layer approximation. Calculation of the boundary layer equations then yields the familiar displacement thickness or its equivalent the surface transpiration velocity. Either of the latter is then inputted into the equivalent inviscid flow to update the configuration tangency condition to reflect the viscous displacement effects. The above cycle is then repeated until convergence of the iterative cycle is achieved. In the absence of separation, the above direct formulation was found to be convergent with the solution in most cases comparing closely with experiments.

In the direct mode described above, the field equations are of mixed parabolic/hyperbolic type, whereas the integral equations in most formulations are fully hyperbolic. In the presence of flow separation, the above iterative procedure in the direct mode ceased to converge when a marching direction, successful in the direct mode, was used to solve the boundary layer problem. The primary cause of the difficulty was an instability of the boundary layer procedure (in both the field and integral methods) due to the finite difference marching not being in the proper downwind direction. Moreover, in the field method a "saddle-point" type ill-conditioning has been experienced for near-unswept separations.

Additionally, in the integral formulation, when the form factor H ("delta star/theta") assumed values in the range 2-3, a singularity arose due to the form factor modeling, halting the marching. Since the form factor is in most cases less than the "singular value" for free shear layer separations, the above difficulty was confined to the more severe bubble type separations, for example, arising in the transonic case. It is not clear whether a form factor relation, free of the singularity, can be evolved using improved velocity profiles. For this purpose, appropriate Navier/Stokes solutions should be examined for guidance.

To circumvent the problems described above for separated flows, the boundary layer problem, both in the field and integral forms, was posed in one of several inverse forms where two of the boundary layer variables were used as inputs instead of the surface pressure and flow direction. In cases where the inverse formulation permitted a marching (cases not partially elliptic), a reorientation of the "downwind" direction then permitted the use of the convenient marching used in the direct mode. Additionally, the form factor singularity in the integral formulation was removed. A difficulty that then arose with the inverse formulation was the loss of the input/output compatibility between the boundary layer and equivalent inviscid flow problems which then precluded the classical iterative procedure of the direct mode. In the inverse mode, the output from both problems was the surface pressure and flow direction which in general would not be the same. An update procedure was then required to determine improved inputs to both problems as a function of the pressure/flow direction mismatch. Simplified local update procedures successful in the planar problem (see for example LeBalleur, Ref. 1), were found to be inadequate in the 3D cases when significant separation was present (Ref. 2).

The simplifications due to the boundary layer approximation are 1. simplification and stiffness reduction of the equations, and 2. the decoupling of the inviscid and viscous portions of the flow. The same simplifications can be achieved without incurring the above update problem by patching the boundary layer flow to the outer inviscid flow using a multiblock mesh. Here the multiblock mesh from the NASA/Ames transonic N/S (TNS) code (Ref. 3) might be used in which the inner blocks

embed the configuration with its boundary layer and wake and the outer blocks contain the inviscid portion of the flow. In the inner blocks the unsteady boundary layer method developed by Van Dalsem and Steger (Ref. 4) would be used. An overlapping of the mesh blocks then provides the framework to impose flow continuity. Another similar approach of promise is the Fortified N/S method proposed by Van Dalsem and Steger (Ref. 5). It avoids the difficulties of the boundary layer approach by overlapping the boundary layer and the outer flow and effecting the coupling through the novel use of a source term.

In summary, the situation for computing separated boundary layer flows is as follows: In the case of the field method, one must march in the proper downwind direction at each level of the boundary layer. For large turning of the flow within the boundary layer as would usually arise in separated flows, care must be exercised in the choice of the proper finite difference marching direction. To ease this task, Van Dalsem and Steger (Ref. 4) used the unsteady formulation, properly biasing the transverse spatial differences. For the case of the integral method, there is not only a need to march in the proper downwind direction, but the form factor singularity must be dispensed with, either by posing the problem in the inverse mode, or in a more difficult fashion, by employing a compatibility condition to neutralize the singularity (Ref. 2). In the inverse mode, the difficulty then arises of a need of an yet-to-be evolved update procedure to permit iterations between the boundary layer and equivalent inviscid flows. The use of a flow patching with a multiblock mesh and the use of the Fortified N/S method is then suggested as means to avoid this difficulty.

2. FLUID DYNAMICS PANEL WORKING GROUP 10

In view of the prospects of treating significant separated flows with greatly reduced computing costs relative to the Navier/Stokes method, the AGARD Fluid Dynamics Panel (FDP) established Working Group (WG) 10 "3D Viscous Flows-Boundary Layer Limit" with the following Objective and Scope.

Objective

The primary objective is to develop procedures to calculate compressible turbulent separated flows over lifting bodies and wings in the high Reynolds Number limit to be carried out in two steps:

1. Develop techniques to solve the boundary layer equations for separated flows prescribing appropriate direct or inverse input functions.
2. Develop techniques to couple the resulting boundary layer problem with the equivalent inviscid flow problem.

Scope

The WG will be confined to steady turbulent flows using both the field and integral boundary layer equations. In the former, the emphasis will be on algebraic turbulence models though differential equation models may also be considered. The primary goal here will not be on the validation of the turbulence model, but on the development of the mechanics of the boundary layer procedure and its coupling with the inviscid flow method.

Two test cases to be considered are the DFVLR 6:1 prolate spheroid and the Lockheed/NASA-Ames Wing C Fighter Wing for which experimental data are available. The Navier/Stokes solutions will also be used as a comparison data base.

There was great interest among the NATO member countries in the WG 10, but there was initial concern as to how to approach the tasks with the wide disparity in the stage of development in the various countries. It was therefore agreed upon that the WG would function as a clinic whereby the participants would exercise their methods at their respective stages and share their experiences, particularly with respect to the numerical difficulties encountered and their cures. This cooperative spirit would be carried out, respecting the proprietary requisites of the participating groups. Members of the WG 10 were as follows:

Mr. J. C. LeBalleur
ONERA-Chatillon

Dr. B. van den Berg
NLR-Amsterdam

Prof. T. Cebeci
CSU-Long Beach

Dr. C. Gleyzes
ONERA-Cert

Prof. E. H. Hirschel
MBB-Ottobrun

Mr. D. Humphreys
FFA-Stockholm

Dr. H. U. Meier
DFVLR-Göttingen

Prof. H. Norstrud
University of Trondheim

Prof. M. Onorato
Politecnico di Torino

Mr. A. Pagano
British Aerospace-Filton

Dr. A. Panaras
Athens (NASA-Ames)

Prof. L. Roberts
Stanford University

Dr. P. D. Smith
RAE-Farnborough

Dr. J. Steger
NASA-Ames

Dr. H. W. Stock
Dornier GmbH

Dr. H. Yoshihara
Boeing Company

The first chairman of the WG was Dr. H. Yoshihara, who in turn was succeeded by Dr. A. Panaras and Prof. H. Norstrud. (This change in the chairmanship was necessitated by the AGARD policy requiring the chairman to be a member of the Fluid Dynamics Panel.) The term of the WG was from September 1985 to June 1988. WG meetings were held over two days during the week preceding the FDP business meeting. Meeting were held as follows: Fall 1985 (AGARD HQ, Paris); Spring 1986 (Politecnico di Torino, Torino); Fall 1986 (Stanford University, Palo Alto); Spring 1987 (London); Fall 1987 (Naples); and Spring 1988 (Lisbon). Tasks were carried out by the following Committees:

1. Data Base: Chairman, Dr. B. van den Berg
 - a. 6:1 Prolate Spheroid, Dr. H. U. Meier
 - b. Wing C, Dr. A. Panaras
 - c. Navier/Stokes Solutions, Dr. J. Steger
2. Integral Methods: Chairman, Dr. P. D. Smith
3. Field Methods: Chairman, Dr. T. Cebeci
4. Inviscid/Viscid Interaction: Chairman, Mr. J. C. Le Balleur
5. Coordination with Eurovisc Committee and "Stanford II" Committee (Prof. G. Lilley): Mr. D. Humphreys

The remainder of the report is organized as follows:

- Chapter 2. Physical Aspects of 3D Separated Flows
Dr. B. van den Berg
- Chapter 3. Theoretical Formulation
Mr. J. C. LeBalleur* and Prof. Dr. E. H. Hirschel
- Chapter 4. Numerical Procedures
 - a. Integral Methods
Dr. P. D. Smith*, Dr. C. Gleyzes, and Dr. H. Stock
 - b. Field Methods
Mr. D. Humphreys*, Dr. T. Cebeci, and Dr. B. van den Berg
- Chapter 5. Data Base for Test Cases
 - a. Experimental Cases
Dr. H. U. Meier*, and Dr. H. Yoshihara
 - b. Navier/Stokes Calculations
Dr. J. Steger*, and Dr. A. Panaras
- Chapter 6. Summary of Results and Computational Guidelines
Dr. L. Roberts*, and Mr. D. Humphreys
 - a. Integral Methods
Dr. P. Smith*, Mr. J. C. LeBalleur, Dr. C. Gleyzes, and Dr. H. Stock
 - b. Field Methods
Dr. T. Cebeci*, Dr. B. van den Berg, Prof. Dr. E. H. Hirschel, Mr. D. Humphreys, and Dr. F. Menter
- Chapter 7. Conclusions.
Prof. Dr. H. Norstrud*, and Dr. H. Yoshihara

The asterisks denote the principal authors.

3. REFERENCES

1. LeBalleur, J. C., Numerical Flow Calculation and Viscid/Inviscid Interaction Techniques, Recent Advances in Numerical Methods in Fluids, Vol. III, Viscous Flows, Pineridge Press, 1984.
2. Wai, J. C., Baillie, J., and Yoshihara, H., Computations of Turbulent Separated Flows Over Wings, Proceedings 3rd Symposium on Numerical and Physical Aspects of Aerodynamic Flows, Springer Press, 1985.
3. Kaynak, U., Holst, T., and Cantwell, B., Computation of Transonic Separated Wing Flows Using an Euler/Navier-Stokes Zonal Approach, NASA TM 88311, 1986.
4. Van Dalsem, W., and Steger, J., The Efficient Simulation of Separated Three Dimensional Viscous Flows using the Boundary Layer Equations, AIAA Paper 85-4064.
5. Van Dalsem, W. R., and Steger, J. L., Using the Boundary Layer Equations in Three Dimensional Viscous Flow Simulation, AGARD CP, 1986.

CHAPTER 2

PHYSICAL ASPECTS OF 3D SEPARATED BOUNDARY LAYER FLOWS

B. van den Berg, National Aerospace Laboratory, NLR,
Anthony Fokkerweg 2, 1059 CM Amsterdam, The Netherlands

In this chapter two subjects will be discussed more specifically. In the first place a description will be given of 3D separated flow patterns in general. This means that attention will be focussed on the topological features of the flow. It is important to understand these features for the calculation process to be followed and for the interpretation of the results. As practical flows are generally turbulent and an exact description of turbulence is far beyond reach at this moment, an approximate mathematical model for the turbulence terms in the equations has to be employed in calculations. These empirical models are at least partly based on general physical notions and they are the second subject to be discussed in this chapter.

When referring to calculations, field methods for the viscous flow have been assumed here, as they relate more simply to the physics. Integral methods, which solve the boundary layer equations in a global way, actually do a comparable job, but the turbulence model is hidden in global empirical assumptions. Also the discussion on the topology of 3D separated flows is not basically different for integral methods, including the properties near separation (Cousteix & Houdeville 1981).

2.1 Topological features of separated flows

It may be useful to start recapitulating shortly the features of separation in 2D stationary flows. Separation is then simply identified with a line with skin friction $\tau_w = 0$, indicating the beginning of a reverse flow region, which is inaccessible for fluid from upstream. Further features are that the boundary layer thickness grows generally rapidly at and downstream of the separation line and that the interaction between the viscous and inviscid flow becomes large. It is well known that solutions of the laminar boundary layer equations with pressure distribution prescribed produce a singularity, $\tau_w \sim x^{1/2}$, near separation. Similar behaviour may be expected for turbulent boundary layer calculations, dependent on the turbulence model. However, regular solutions can be obtained when prescribing other boundary conditions such as the boundary layer displacement thickness variation (e.g. Catherall & Mangler 1966). These, as well as full Navier-Stokes solutions, indicate that the physical flow behaves regularly, $\tau_w \sim x$, near separation.

In 3D flows the skin friction $\tau_w = 0$ only at singular points and not generally along a line on the surface. Close to such a point the skin friction components τ_{wx} and τ_{wy} in the orthogonal directions x and y may be written in case of regular behaviour: $\tau_{wx} = a_{xx}x + a_{xy}y$ and $\tau_{wy} = a_{yx}x + a_{yy}y$, retaining only the lowest-order terms in the series expansion, which means that the discussion will be restricted here to first-order singularities. Dependent on the sign and magnitude of the coefficients $a_{xx}, a_{xy}, a_{yx}, a_{yy}$, different types of singular points are obtained (e.g. Lighthill 1963). Figure 2.1 shows patterns of the skin friction lines or wall streamlines near such points for some typical cases. If $J = a_{xx}a_{yy} - a_{xy}^2 > 0$ an infinite number of wall streamlines pass through the singular point. The singular point is called a node in this case. If $\Delta = a_{xx} + a_{yy} > 0$ it is a node of attachment as sketched in figure 2.1.a. When changing the direction of the arrows of the wall streamlines in the sketch a node of separation, $\Delta < 0$, is obtained. Clearly on an isolated three-dimensional body at least one node of attachment and one node of separation must be present. If $\Delta^2/4 - J < 0$ the wall streamlines approach the singular point asymptotically in spirals. Such a node is called a focus, see figure 2.1.b. The presence of a focus of separation generally marks the development of a vortex in the flow. If $J < 0$ the wall streamlines, except two, do not pass through the singular point. Such a point is called a saddle and if $\Delta < 0$ it is a saddle point of separation as sketched in figure 2.1.c. Finally it seems useful to mention in this short survey a well-known topological rule, which states that the number of nodal points (nodes and foci) exceeds the number of saddle points by two on bodies with no multiply connected surfaces (Lighthill 1963).

Nodes are either sources or sinks of wall streamlines, as contrasted with saddles. The special feature of a saddle is that it partitions the wall streamlines coming from both sides towards the saddle. The two wall streamlines leaving the saddle act, at least locally, as a barrier between wall streamlines coming from opposite directions. An exceptionally efficient barrier occurs in the degenerate case of a line with saddle points of separation. Such a line corresponds to what is called a separation line in 2D flows. Analogously one might call the wall streamlines leaving a saddle point separation lines in 3D flows. More precisely Lighthill (1963) has proposed to define as separation lines wall streamlines, which issue from a saddle point of separation and disappear in a node of separation. It should be noted, however, that many of the physical features attending 2D separation, as summarized earlier, do not apply here. The differences will be discussed in some detail in the next paragraphs.

In the first place in 3D flows the skin friction is not zero except at the saddle point itself. Further it is not generally true that the wall streamlines issuing from a saddle point act as a complete barrier between flow from "upstream" and "downstream", as a 2D separation line does. This is illustrated in figure 2.2, which shows some simple wall flow patterns near one or two nodes and saddles. It is evident from figures 2.2.b and c that the wall streamlines issuing from the saddle points and disappearing in the foci, do not constitute a complete barrier. Actually the wall streamlines directed towards the saddle point from downstream all originate upstream, which means that the whole surface is accessible from upstream. Figure 2.2.a, showing the flow pattern for a saddle with a node downstream, provides an example where the wall streamlines issuing from the saddle indeed constitute a complete barrier. Even in this case, however, this holds only for the wall streamlines and not necessarily for any other streamline away from the wall, since the external streamline attaching to the downstream node normally does not originate at the upstream saddle, see figure 2.2.a. A closed region with separated fluid, which is inaccessible for fluid from upstream, as in 2D separations, does not exist in the case shown. In general it may be stated that closed separation regions probably are earlier an exception than the rule in 3D flows (Hunt et al. 1978). The fact that 3D flow separations, due to the extra dimension, generally tend to be open separations, seems not to be always sufficiently well appreciated.

In 2D flows, separation is accompanied with rapid boundary layer growth. Such a rapid growth does not necessarily occur in 3D flows near wall streamlines issuing from saddle points of separation. To evaluate the growth, the continuity equation for the flow near the surface will be considered. Assuming $U \sim r_z$, one obtains $r_z \Delta n = \text{constant}$, where z is the wall distance and Δn is the distance between two neighbouring wall streamlines. In 2D flows $\Delta n = \text{constant}$, but $r_z \rightarrow 0$ at separation, so that the wall distance z must grow very rapidly to satisfy continuity. In 3D flows the skin friction does not go to zero, except at the singular points, and rapid boundary layer growth along special wall streamlines is not evident. Rapid growth must come in that case from a fast decrease of Δn , i.e. from a strong flow convergence. Strong flow convergence does not always occur along wall streamlines issuing from saddle points. On the other hand experimental evidence indicates that strong flow convergence may occur along wall streamlines, which do not issue from a saddle point, and which do not distinguish themselves in any fundamental aspect from other wall streamlines. Further downstream along such a wall streamline a very thick boundary layer will have developed with many of the physical features that are generally associated with separation. This has led Wang (1976) to call this an "open separation". The terminology is confusing, however, since most 3D separations are open, as argued in the preceding paragraph. The important conclusion is that separation-like flow features may start to develop along a wall streamline at a position, which is not well defined and is not a singular point, while along wall streamlines issuing from a saddle point separation-like features may not become very evident at all.

Since the boundary layer thickness increases rapidly at and downstream of a 2D separation line, the viscous effect on the inviscid flow will be large. On the other hand small changes of the pressure gradient imposed by the inviscid flow on the viscous flow may have large effects as the velocities in 2D separation regions are small. This is a physical explanation for the strong viscous-inviscid interaction in these conditions. Because rapid boundary layer growth does not always occur in 3D flows along the lines which may be defined as separation lines, and because the velocities are not always small in 3D separation regions, strong viscous-inviscid interaction does not necessarily occur here on physical grounds. A mathematical reason for strong viscous-inviscid interaction may be singular behaviour of the solution near the separation line, like in 2D flows when the boundary layer equations are solved with the pressure distribution prescribed. The behaviour of the solution of the 3D boundary layer equations near special lines like wall streamlines issuing from saddle points, has not been investigated thus far in detail for the general case. For quasi-two-dimensional flows some conclusions can be drawn, however, from a simple analysis to be discussed hereafter.

In the analysis laminar boundary layers will be assumed, but the results are likely to hold also for turbulent flows as with the normal turbulence models the equations are similar to a fairly high order of approximation close to the wall, which is the region of interest here. For quasi-two-dimensional laminar boundary layers, as occur on infinite swept wings, the so-called independence principle holds (e.g. Schlichting 1979). The independence principle states that the velocity component normal to the lines of invariance (e.g. the infinite swept wing leading edge) can be solved independently from the velocity component parallel to these lines. This means that that part of the solution is identical to the 2D solution. It can be concluded, therefore that in that case with the pressure distribution prescribed the skin friction component normal to the separation line $\tau_{\perp} \sim x^{1/2}$ near separation, as in 2D. The other component $\tau_{\parallel} = \text{constant}$. Consequently the skin friction of wall streamlines touch in cusp-like manner the separation line, which is then an envelope of wall streamlines. The solution thus obtained is singular at the separation line. Like in 2D flows, however, regular solutions may be obtained when employing more appropriate solution techniques, applying other boundary conditions or solving the full Navier-Stokes equations. In such calculations the skin friction near separation will vary as $\tau_{wx} \sim x$, $\tau_{wy} = \text{constant}$, which means that the separation line is an asymptote of wall streamlines.

The question, whether a 3D separation line, issuing from a saddle point and disappearing in a node, is an envelope or an asymptote of wall streamlines, has received continual attention in the literature (e.g. Maskell 1955, Lighthill 1963, Brown & Stewartson 1969, Wang 1976, Hornung & Perry 1984). If the foregoing quasi-two-dimensional analysis may be generalized, it is clear that a separation line is not an envelope of wall streamlines, neither in physical reality nor in proper calculations. This conclusion should not be surprising, since singularities, as occur at cusps, can not be expected to exist in reality. The occurrence of cusps at separation in boundary layer calculations is due to improper boundary conditions and may be dependent also on the marching direction. In fully 3D flows the wall streamlines probably do not really approach the separation line asymptotically, but all touch the separation line at the downstream node, where it terminates. Surface flow visualizations seem to suggest that separation lines are envelopes of wall streamlines, but obviously rigorous conclusions can never be drawn from such observations.

It will be evident from the foregoing that the definition of the separation line in 3D flows poses problems. An unambiguous definition is that of Lighthill: a separation line is a wall streamline issuing from a saddle point of separation and disappearing in a node of separation. Many of the physical flow features associated with 2D separations may not occur along such wall streamlines, however. Also, as these lines are no envelopes of wall streamlines, they may not be distinguishable from any other wall streamline apart from their special origin. At the same time wall streamlines, which do not originate at a saddle point, may show many of the physical features generally associated with separation. Since in practice one normally wants to include the latter case in the separated flows, several other definitions for a 3D separation line have been considered, none of them satisfactory (see e.g. Wang 1976). Definitions based on the breakdown of the boundary layer assumptions or rapid boundary layer growth are inadequate as these do not provide precise criteria. Whether singular solutions of the boundary layer equations occur along a separation line depends on the solution technique. Inaccessibility for upstream fluid also does not lead to a satisfactory discrimination as mostly the whole flow is accessible in the 3D case. It seems that the separation line concept adopted from 2D flows is not simply transferable to 3D flows.

If the term separation is yet employed for 3D flows, as is usual practice, it is profitable to distinguish two types of separation lines: wall streamlines issuing from saddle points and lines of convergence not involving singular points. There is considerable diversity in the terminology for the two types of separation in the literature, e.g. bubble vs free-shear-layer separation (Maskell 1955), closed vs open separation (Wang 1976), global vs local separation (Tobak & Peake 1982), while also the term cross-flow separation is used for the latter type (Chapman 1986). Unfortunately all the terms proposed are misleading to some extent due to preconceived ideas about the flow physics, which do not always apply. In

fact the flow area further downstream behind e.g. a saddle and a node (figure 2.2.a) may be indistinguishable from those in two regions of flow convergence involving no singular points. Therefore, it seems most rational to refer to both types of separation on the basis of their elementary distinguishing feature. This suggests the use of terms like saddle point separation and gradual separation respectively. Since in the latter case no singular points are involved and the separation characteristics develop gradually, the term separation is inherently not precise here.

In this report two test cases for boundary layer calculations are considered. These include the 3D turbulent boundary layer flow on an ellipsoid at 10° and at 30° angle of attack and a transonic swept wing flow with a local separation. The flow separations on the ellipsoid at angle of attack are typical gradual separations involving no singular points. Though far downstream on the ellipsoid saddle point separations may occur, the 3D separation in the region of interest here, i.e. the region where boundary layer calculations have been performed, is of the gradual type at both angles of attack (Meier et al 1983). On the swept wing, however, the surface flow visualizations (Keener 1985) indicate the presence of a saddle point separation. Actually a saddle and a focus are clearly recognizable on the wing upper surface at the test case conditions ($M_\infty = 0.85$, $\alpha = 5^\circ$, $Re_\infty = 6.8 \times 10^6$). The separated wall streamline pattern is basically similar to that sketched in figure 2.2.b.

2.2 Turbulence modelling of separated flows

As a universal model for the turbulent shear stresses in the Reynolds-averaged flow equations does not yet exist, and probably will never do, semi-empirical models have to be applied in calculation methods. These semi-empirical models have generally a restricted range of applicability. This leads to turbulence models valid for specific flow zones. In this section turbulence models for separated flows will be reviewed briefly. Actually the emphasis will be on the complexities and the consequent unsatisfactory state of affairs in turbulence modelling, notably for separated flows.

It may be useful to start again, as in section 2.1, with a discussion of the situation for 2D separated flows. When the boundary layer is not separated, the flow properties in the wall region determine to a large extent the 2D turbulent boundary layer development. Since the flow in the wall region seems to behave reasonably well universally (as appears from the wide validity of the law of the wall), simple turbulence models describing at least the wall region correctly produce often satisfactory results. The situation becomes different, however, when the flow separates from the wall. The boundary layer becomes then a free shear layer developing above a recirculation region in which the velocities are comparatively small. As the stabilizing effect of the wall is absent, the turbulence level in the free shear layer tends to increase substantially. When the separated flow reattaches, the free shear layer is splitted into two parts, one part flowing backwards into the recirculation region. This will affect especially the development of the large turbulent eddies. Clearly substantial changes in turbulence level and structure occur in case of a 2D separation (and reattachment). As these changes take place generally comparatively fast, turbulence history effects may be expected to play an important role. In addition, 2D separated flows are often unsteady and the low frequency fluctuations, which probably do not depend on local conditions only, may affect the turbulence structure and can produce a non-negligible direct contribution to the turbulent shear stresses (e.g. Bradshaw 1978). It will be clear that complex turbulence models are needed to describe the phenomena in such flows more or less satisfactory. Actually the accuracy of the turbulence models available up to now for 2D separation regions is inadequate (e.g. Kline et al 1983, Delery & Marvin 1986).

As argued in section 2.1, the physical features attending a 3D separation do not necessarily resemble very closely those of a 2D separation. For instance, if there is a recirculation region downstream of a 3D separation line, the velocities need not to be small in that region as there may be a significant velocity component parallel to the separation line. Moreover, often 3D separations do not feature a distinct recirculation region, the separation region being open. It is also not possible generally to distinguish downstream of a 3D separation line clearly a shear layer away from the wall, as in 2D separations. Actually the flow near and downstream of a 3D separation line may not be very different from a normal attached 3D boundary layer flow. It will be evident from the foregoing that the substantial changes in turbulence level and structure attending 2D separations, do not necessarily occur in the same way in 3D separations. On the other hand the flow is generally strongly three-dimensional near 3D separations and the usual problems associated with turbulence modelling for 3D boundary layers apply here consequently.

It is generally accepted now that simple scalar eddy viscosity turbulence models are inadequate for 3D boundary layers as a considerable eddy viscosity non-isotropy appears to exist. Some experimental values of the ratio of the crosswise to the streamwise eddy viscosity N in three-dimensional boundary layers are collected in figure 2.3. The plot includes the recent experimental data from Anderson and Eaton (1987), which again show that the ratio N may attain values substantially less than one. Though the non-isotropy of the eddy viscosity has attracted most attention, the comparatively low magnitude of the eddy viscosity in 3D boundary layers according to experiments is at least as important to take into account for accurate turbulence modelling. Figure 2.4 shows the considerable decrease of the eddy viscosity magnitude measured in a boundary layer developing from a 2D condition to a 3D separation (Elsenaar & Boelsma 1974).

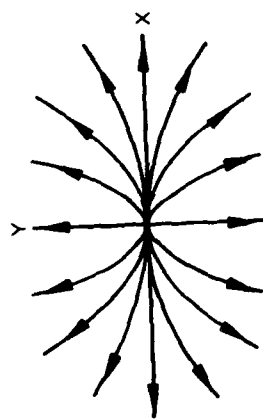
In general experiments indicate that the turbulence level decreases when the flow becomes three-dimensional. Various explanations have put forward. It has been proposed that due to the flow three-dimensionality the large turbulent eddies are hindered in their development as they will topple and that consequently turbulence activity decreases (Bradshaw & Pontikos 1985). Further, history effects may be expected to be responsible for at least part of the effects found (Van den Berg 1982). Three-dimensional boundary layers involve generally also flow convergence or divergence, which are known to lead to a substantial turbulence level decrease or increase respectively (e.g. Patel & Baek 1987). Due to the extra dimension, additional phenomena which affect the turbulence properties occur in 3D flows and complicate accurate turbulence modelling.

It may be concluded that turbulence modelling in 3D separation regions poses different, though not necessarily more difficult problems than in 2D separation regions. In both cases the problems are far from solved, however, and it looks like that in the not too distant future the probably still existing

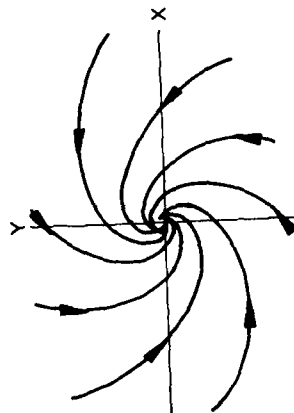
shortcomings of the turbulence models will be the principal factor limiting the accuracy of boundary layer calculations, notably in separation regions.

References

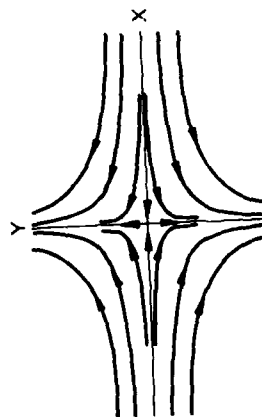
- Anderson, S.D., Eaton, J.K., 1987, "An experimental investigation of pressure driven three-dimensional turbulent boundary layers". Stanford University, Therm. Div. Rep. MD-49.
- Berg, B. van den, 1982, "Some notes on three-dimensional turbulent boundary layer data and turbulence modelling". IUTAM Symposium, Berlin, Eds: H.H. Fernholz, E. Krause.
- Bradshaw, P., 1978, "Structure of turbulence in complex flows". AGARD LS No. 94.
- Bradshaw, P., Pontikos, N.S., 1985, "Measurements in the turbulent boundary layer on an infinite swept wing". J. Fluid Mech. 159, 105.
- Brown, S.N., Stewartson, K., 1969, "Laminar separation". Annual Review of Fluid Mech., Vol. 1, 45.
- Catherall, D., Mangler, K.W., 1966, "The integration of the two-dimensional laminar boundary layer equations past the point of vanishing skin friction" J. Fluid Mech. 26, 163, 1966.
- Chapman, G.T., 1986, "Topological classification of flow separation on three-dimensional bodies". AIAA Paper 86-0485.
- Cousteix, J., Houdeville, R., 1981, "Singularities in three-dimensional turbulent boundary layer calculations and separation phenomena". AIAA J. 19, 8, 976.
- Dechow, R., 1977, "Mittlere Geschwindigkeit und Reynoldsscher Spannungstensor in der dreidimensionalen turbulenten Wandgrenzschicht vor einem stehenden Zylinder". Diss. Un. Karlsruhe, Strömungsmech. & Strömungsmaschinen Heft 21, 1977.
- Delery, J., Marvin, J.G., 1986, "Shock-wave boundary layer interactions". AGARDograph No. 280.
- Elsenaar, A., Boelsma, S.H., 1974, "Measurements of the Reynolds stress tensor in a three-dimensional turbulent boundary layer under infinite swept wing conditions". NLR TR 74096 U.
- Hornung, H., Perry, A.E., 1984, "Some aspects of three-dimensional separation". Part 1: "Stream surface bifurcations". Zeitschrift Flugwiss. & Weltraumforschung 8, 2, 77, 1984.
- Hunt, J.C.R., Abell, C.J., Peterka, J.A., Woo, H., 1978, "Kinematical studies of the flows around free or surface-mounted obstacles; applying topology to flow visualization", J. Fluid Mech. 86, 179.
- Keener, E.R., 1985, "Pressure distribution measurements on a transonic low-aspect ratio wing". NASA TM 86683.
- Kline, A.J., Cantwell, B.J., Lilley, G.M., 1982, "Complex turbulent flows". The 1980-81 Stanford Conf., Vol. 2.
- Lighthill, M.J., 1963, "Attachment and separation in three-dimensional flow". In: L. Rosenhead (ed.): "Laminar boundary layers", Oxford Un. Press.
- Maskell, E.C., 1955, "Flow separation in three dimensions". RAE Aero Report 2565.
- Meier, H.U., Kreplin, H.P., Vollmers, H. 1983, "Development of boundary layers and separation patterns on a body of revolution at incidence", Second Symp. "Numerical and Physical Aspects of Aerodynamic Flows", Ed.: T. Cebeci.
- Patel, V.C., Baek, J.H., 1987, "Boundary layers in planes of symmetry; Part 1: Experiments in turbulent flow". AIAA J. 25, 4, 550.
- Pontikos, N.S., 1982, "The structure of three-dimensional turbulent boundary layers". Ph.D. Thesis, Imperial College, London.
- Schlichting, H., 1979, "Boundary layer theory". McGraw - Hill.
- Tobak, M., Peake, D.J., 1982, "Topology of three-dimensional separated flows". Annual Review of Fluid Mech., Vol. 14, 61.
- Wang, K.C., 1976, "Separation of three-dimensional flow". Martin Marietta Labs TR-76-54 C.



a NODE OF ATTACHMENT
 $a_{xx} = 1$
 $a_{yy} = 2$
 $a_{xy} = a_{yx} = 0$



b SPIRAL NODE OR FOCUS OF SEPARATION
 $a_{xx} = -1$
 $a_{yy} = -1$
 $a_{xy} = -1$
 $a_{yx} = 1$

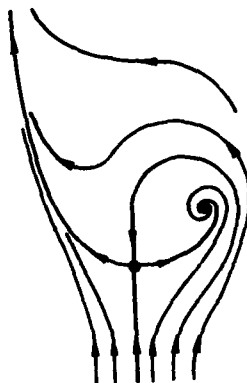


c SADDLE OF SEPARATION
 $a_{xx} = -2$
 $a_{yy} = 1$
 $a_{xy} = a_{yx} = 0$

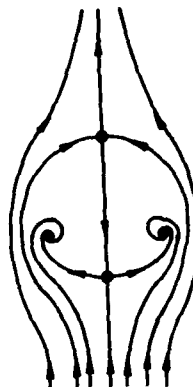
Fig. 2.1 Typical patterns of wall streamlines near singular points



a BUBBLE TYPE
 1 SADDLE
 1 NODE



b VORTEX TYPE
 1 SADDLE
 1 FOCUS



c OWL-FACE
 2 SADDLES
 2 FOCI

Fig. 2.2 Some simple wall streamline patterns near one or two nodes and saddles

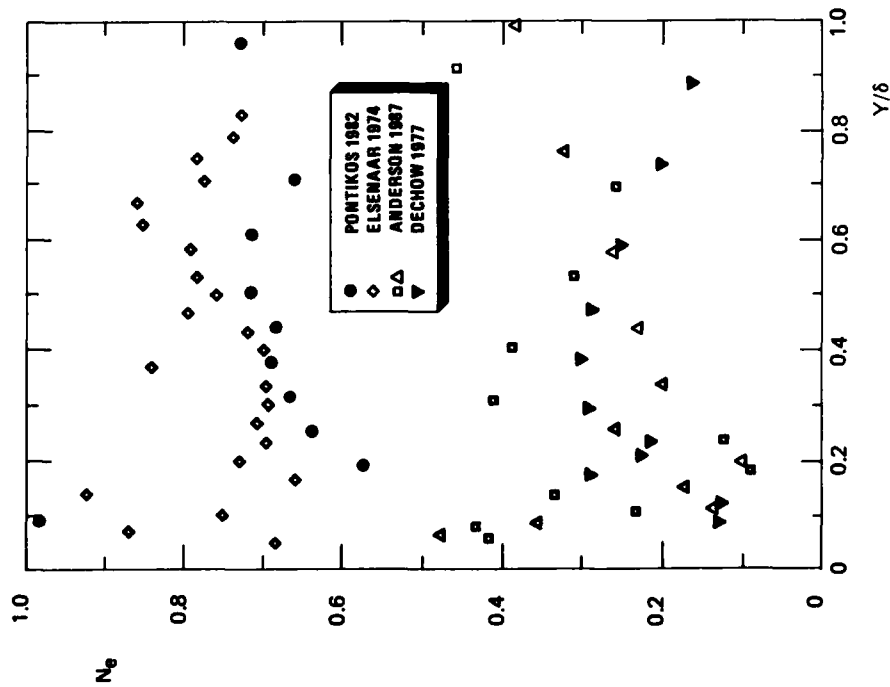


Fig. 2.3 Ratio of local crosswise to streamwise eddy viscosity N_e according to various measurements in 3D boundary layers close to separation

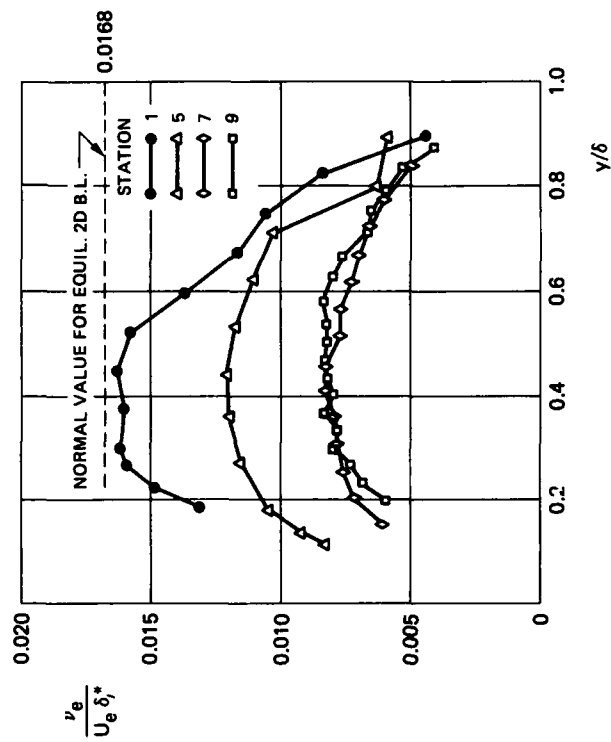


Fig. 2.4 Eddy viscosity according to turbulence measurements.
Station 1: 2D constant-pressure boundary layer
Station 9: 3D boundary layer separation

CHAPTER 3. THEORETICAL FORMULATION

E.H.Hirschel, MBB Flugzeuge-LKE 122,
Postfach 801160, 8000 München 80, Federal Republic of Germany

The Navier-Stokes equations are believed to describe any phenomenon of continuum flow, even turbulence. Discrete numerical solutions of the Navier-Stokes equations are available today, but, except for some special cases, actually the Reynolds-averaged equations are solved for non-laminar flow. The special cases concern large-eddy or direct simulation of turbulent flow, which is possible on a research level now (see for instance Ref. 1).

Although the computer power has grown dramatically in the last decade, solutions of the Reynolds-averaged Navier-Stokes equations are much too expensive to be applied in regular aerodynamic design work, Ref. 2. In addition there are still many not sufficiently solved problems with discrete numerical methods, and the big question marks which have to be put to our abilities to model transition laminar-turbulent and turbulence in separating shear flows.

The aerodynamic design engineer traditionally employs a whole palette of flow models and computation methods in his work. Depending on the given design problem he distinguishes:

- inviscid flow,
- inviscid flow with weak interacting viscous effects,
- inviscid flow with strong interacting viscous effects,
- fully viscous flow,

which usually appear, although in different areas, and with different importance, on every aircraft.

Another way to classify flow fields is by distinguishing

- attached flow,
- separated flow.

There is a problem with the concept of separation, because as it usually is used it stems from two-dimensional flows, where it simply is defined by vanishing surface shear. Actually a more general view should be adopted, Refs. 3 and 4. Whether the boundary layer leaves a sharp edge (flow-off separation at the trailing edge of a wing, or at the leading edge of a delta wing at larger angle of attack), or gets separated at the body surface (free-surface or squeeze-off separation, the latter especially in three-dimensional flow situations), in each case the following effects appear:

- strong interaction of the separating boundary layer with the inviscid flow, which leads to a viscosity induced pressure drag,
- convective transport of vorticity away from the body surface in wakes (vortex sheets) and vortices (the induced drag of a finite-span lifting wing is related to this phenomenon).

If one accepts this more general view it becomes evident at once that separated flow fields in some cases can be treated by means of purely inviscid models, like potential flow models, see for instance Ref. 5, or by Euler models, Ref. 4, see also the very important Ref. 6. The typical application considered in these references is that of delta wings with sharp leading edges at angles of attack, where leading-edge separation appears and hence lee-side vortices.

The scope of the present study is limited to free-surface or squeeze-off separation, where the location of separation is not fixed by sharp edges. The question is whether and how far flow fields with such properties can be handled with some inviscid flow - boundary-layer approach. The basic principle which allows such an approach is the locality principle, Ref. 3.

Experimental and theoretical/numerical results from flowfield investigations on many configurations suggest that a change in body shape or in the flow configuration, for instance by separation, is felt only locally and downstream of that location. This is the reason why in general a boundary-layer computation yields good results compared to experimental results, although usually only inviscid solutions without modelling of the separation phenomena are applied.

The fact that also the location of primary separation lines usually can be predicted to a good degree of accuracy is connected with this principle. The global interaction due to the separating boundary layer obviously is weak in most cases. The local interaction, however, because of the elliptic properties of the flow near a separation line or point, finally makes it impossible to predict exactly the location of separation in the frame of boundary-layer theory.

The locality principle must be used with care. Of course, the flow is changed upstream too, for instance because of the elliptic property of subsonic flow fields. These changes are small as can be seen. They can be significant, if for instance the wake of the body carries kinematically active vorticity. Then a global interaction can occur which may not be significant for the boundary-layer development, but for the global forces on the body. An example for this is the induced drag of wings.

The formulation of boundary-layer computation problems on arbitrary configurations poses no difficulties, Ref. 7. Of course, boundary-layer theory must be valid. It is interesting to note that obviously first-order theory rather early becomes incorrect if the flow is decelerated, even if the boundary-layer thickness, and the longitudinal surface curvature is not large, Ref. 8. Second-order boundary-layer methods, see for instance Ref. 9, allow to treat thick boundary-layers on curved surfaces, where centrifugal pressure corrections must be made, and where the off-surface metric must be taken into account. Of course, then the displacement properties of the boundary-layer must be imposed on the inviscid flow by means of the equivalent inviscid source distribution (Ref. 7), which is done routinely in zonal solutions, Ref. 8. Even hypersonic boundary layers with entropy-layer swallowing can be treated with second-order boundary-layer theory, Ref. 10.

The coupling of a boundary-layer solution with an inviscid solution in order to compute the flow in a separation region or to obtain the global interaction, poses considerable problems. In two-dimensional flow cases inverse or interactive approaches are often used. In general it is possible to extend these to three-dimensional flow cases only if the features of the separated flow allow this. If the flow exhibits a complicated separation topology, then the Reynolds-averaged Navier-Stokes equations have to be employed globally or at least, like in the zonal solution of Ref. 8, locally.

The boundary-layer equations are of parabolic type, Ref. 3 (or in the integral formulation of hyperbolic type), and pose an initial value/boundary-value problem. The streamlines of the boundary layer are characteristics, and therefore the marching direction of the boundary-layer method, and hence the grid must be oriented more or less in main stream direction. A complete orientation along the external inviscid streamlines (streamline coordinates) in general proves to be too complicated to handle, because the external inviscid streamlines converge or diverge in parts of a configuration. Then streamlines have to be deleted or newly to be started (see for instance Ref. 11). A complete configuration orientation of the grid, like in the cross-section oriented grids for fuselages or the percent-line oriented grids on wings, Refs. 7 and 12, also can have drawbacks. Nose or attachment regions, also the regions ahead of primary separation may pose problems with such grids. An interesting approach to combine streamline oriented and configuration oriented grids in so-called hybrid grids was made in Ref. 13. There selected inviscid streamlines form a skeleton in which then a kind of skeleton cross-section grid is constructed. In this way the advantages of both types are combined, while the disadvantages are mostly avoided.

The problem of initial data is closely connected with the grid-orientation problem. Although one-dimensional initial data can be constructed in stagnation points or on attachment lines in chord sections, Ref. 7, in the latter case in the infinite-swept wing mode (or in the locally infinite-swept wing mode, where the correct metric properties of the wing are taken into account), the procedures are quite cumbersome. Usually therefore approximate initial data are employed somewhat downstream of the actual stagnation point or of the actual attachment line. This is possible, because the initial data very fast loose their influence on the downstream solution in favour of the local boundary data if the flow is sufficiently accelerated, Ref. 7. However, if approximate initial data are put in regions of decelerated flow, large errors may build up in the complete downstream solution, unless there again the flow is accelerated, as for instance the flow past automobiles behind the motor hood, Ref. 14.

REFERENCES

1. Schumann U., and Friedrich R. (eds.), Direct and Large-Eddy Simulation of Turbulence, Vol. 15 of Notes on Numerical Fluid Mechanics, Vieweg, Braunschweig-Wiesbaden, 1986.
2. Hirschel E.H., Super Computers Today: Sufficient for Aircraft Design? Experiences and Demands, In: Super Computer '88, H.W. Meuer (ed.), Carl Hanser, München-Wien, 1988, pp. 110-150.
3. Hirschel E.H., Evaluation of Results of Boundary-Layer Calculations with Regard to Design Aerodynamics, In: Computation of Three-Dimensional Boundary Layers Including Separation, AGARD-R-741, 1986, pp. 5-1 to 5-29.
4. Eberle A., Rizzi A., and Hirschel E.H., Numerical Solutions of the Euler Equations for Steady Flow Problems, Vol. 30 of Notes on Numerical Fluid Mechanics, Vieweg, Braunschweig-Wiesbaden, 1990.
5. Hoijmakers H.W.M., and Vaatstra W., Higher-Order Panel Method Applied to Vortex-Sheet Roll-Up, AIAA J., Vol. 21, 1973, pp. 516-523.

6. Elsenaar A., and Eriksson L.E. (eds.), International Vortex-Flow Experiment on Euler Code Validation, FFA Bromma, 1987, ISBN 91-97 0914-0-5.
7. Hirschel E.H., and Kordulla W., Shear Flow in Surface-Oriented Coordinates, Vol. 4 of Notes on Numerical Fluid Mechanics, Vieweg, Braunschweig-Wiesbaden, 1981.
8. Wanie K.M., Schmatz M.A., and Monnoyer F., A Close Coupling Procedure for Zonal Solutions of the Navier-Stokes, Euler and Boundary-Layer Equations, ZFW, Vol. 11, No. 6, 1987, pp. 347-359.
9. Monnoyer F., Calculation of Three-Dimensional Attached Viscous Flow on General Configurations with Second-Order Boundary-Layer Theory, to appear in Zeitschrift für Flugwissenschaften (ZFW), also MBB-S-PUB-345, 1988.
10. Monnoyer, F., Mundt, Ch., and Pfitzner M., Calculation of the Hypersonic Viscous Flow Past Reentry Vehicles with an Euler/Boundary-Layer Coupling Method, AIAA-Paper 90-0417, 1990.
11. Geissler W., Calculation of the Three-Dimensional Laminar Boundary Layer Around Bodies of Revolution at Incidence and With Separation, AGARD CP-168, 1975, pp. 33-1 to 33-11.
12. Hirschel E.H., Boundary-Layer Coordinates on General Wings and Fuselages, ZFW, Vol. 6, No. 3, 1982, pp. 194-202.
13. Grün N., Hybrid Coordinates for 3-D Boundary-Layer Calculations, in: Numerical Grid Generation in Computational Fluid Mechanics '88, S. Sengupta, J. Häuser, P.A. Eise-mann, J.F. Thompson (eds.), Pineridge Press, Swansea, 1988, pp. 835-844.
14. Hirschel E.H., Bretthauer N., and Röhe H., Theoretical and Experimental Boundary-Layer Studies on Car Bodies, J. of the Int. Ass. for Vehicle Design, Vol. 5, No. 5, 1984, pp. 567-584.

CHAPTER 4. NUMERICAL PROCEDURES

4.1 Integral methods

P.D. Smith, AES Division, Royal Aerospace Establishment,
Farnborough, Hants GU14 6TD, United Kingdom

4.1.1 The integral equations

Integral prediction methods for three-dimensional turbulent boundary layers are most readily described in a streamline coordinate system (s, n) which consists of two families of mutually orthogonal curves on the body surface. One family is formed by the projections, onto the surface, of streamlines just external to the boundary layer. The direction(s) of an external streamline is called the streamwise direction and boundary-layer flow in a direction (n) normal to an external streamline and parallel to the surface is called crossflow. For general applicability the equations in the s, n streamline coordinate system are transformed to a general non-orthogonal curvilinear coordinate system; x, y in the surface z normal to the surface with an angle $\lambda(x, y)$ between the x and y directions and an angle $\alpha(x, y)$ between the x and s directions.

The integral equations in streamline coordinates are¹ s momentum integral:

$$\frac{\partial \theta_{11}}{\partial s} + \frac{\partial \theta_{12}}{\partial n} + \theta_{11} \left(\frac{H+2-M_e^2}{U_e} \frac{\partial U_e}{\partial s} - K_s \right) + \theta_{12} \left(\frac{2-M_e^2}{U_e} \frac{\partial U_e}{\partial n} - 2K_n \right) + \delta_2 \left(\frac{1}{U_e} \frac{\partial U_e}{\partial n} - K_n \right) + K_s \theta_{22} = \frac{C_{fs}}{2} \quad (1)$$

n momentum integral:

$$\frac{\partial \theta_{21}}{\partial s} + \frac{\partial \theta_{22}}{\partial n} + \theta_{21} \left(\frac{2-M_e^2}{U_e} \frac{\partial U_e}{\partial s} - 2K_s \right) + K_n \theta_{11} (H+1) + \theta_{22} \left(\frac{2-M_e^2}{U_e} \frac{\partial U_e}{\partial n} - K_n \right) = \frac{C_{fn}}{2} \quad (2)$$

Entrainment or continuity integral:

$$\frac{\partial [\delta - \delta_1]}{\partial s} - \frac{\partial \delta_2}{\partial n} + [\delta - \delta_1] \left[\frac{1-M_e^2}{U_e} \frac{\partial U_e}{\partial s} - K_s \right] - \delta_2 \left(\frac{1}{U_e} \frac{\partial U_e}{\partial n} - K_n \right) = C_E \quad (3)$$

Here U_e is the external velocity in the streamline direction, M_e denotes the Mach number corresponding to U_e , C_{fs} and C_{fn} are the skin friction components in the streamwise and crosswise directions respectively. δ is the boundary-layer thickness, C_E the entrainment coefficient, H the ratio δ_1/θ_{11} and the integral thicknesses are defined as:

$$\begin{aligned} \theta_{11} &= \int_0^\delta \frac{\rho U}{\rho_e U_e^2} (U_e - U) dz, & \theta_{12} &= \int_0^\delta \frac{\rho V}{\rho_e U_e^2} (U_e - U) dz, & \theta_{21} &= \int_0^\delta -\frac{\rho UV}{\rho_e U_e^2} dz, \\ \theta_{22} &= \int_0^\delta -\frac{\rho V^2}{\rho_e U_e^2} dz, & \delta_1 &= \int_0^\delta \frac{(\rho_e U_e - \rho U)}{\rho_e U_e} dz, & \delta_2 &= \int_0^\delta -\frac{\rho V}{\rho_e U_e} dz \end{aligned} \quad (4)$$

and $\theta_{21} = \theta_{12} + \delta_2$. In addition we define $H_1 = (\delta - \delta_1)/\theta_{11}$.

The terms K_s and K_n are the geodesic curvatures of the curves $s = \text{constant}$ (normals) and $n = \text{constant}$ (streamlines) respectively. General expressions for K_s and K_n in terms of the angle α and the geometry of the x, y coordinate system may be found in Reference 1. K_s is a measure of the rate of divergence of the external streamlines whilst if the z component of the vorticity of the external flow is zero $K_n = 1/U_e (\partial U_e / \partial n)$ and some simplification of equations (1) to (3) results.

More general versions of equations (1) to (3) which make allowance for pressure gradients normal to the surface and include terms resulting from the Reynolds normal stresses may be found in References 2, 3 and 13.

4.1.2 Particular methods of solution

The major differences between the integral calculation methods used by the members of the Working Group occur in the assumptions made regarding the entrainment coefficient C_E and the forms assumed for the streamwise and crossflow velocity profiles. These profiles are needed in order to derive relationships between the integral thicknesses (equation (4)) thus reducing the number of unknowns. The major assumptions made are detailed below.

4.1.2.1 RAE method^{4,5}

The method is essentially that of Smith, Reference 4, but since extended to allow for history effects upon the turbulence structure (Reference 5) by calculating the entrainment coefficient by means of the lag equation of Green, Weeks and Brooman (Reference 6) applied along the external streamlines. Power law velocity profiles are used in the streamwise direction and Mager (Reference 7) profiles in the crossflow direction. To improve the prediction of the streamwise flow the $H_1 = H_1(H)$ relationship used is not that which would be given by the power law velocity profiles but instead the $H_1 = H_1(H)$ relationship as given by Lock's (Reference 8) equation (105) is used. This includes allowances for the effects of low Reynolds number and of strong departures from equilibrium. In addition it is necessary to assume a skin friction law for C_{fs} and that of Green et al (Reference 6) is used. The dependent variables of the method are θ_{11} , H and $\beta \equiv \tan^{-1}(C_{fn}/C_{fs})$.

4.1.2.2 RAE method using Cross's⁹ profiles

Here the simple but fairly restricted power law and Mager profiles of Smith's method are replaced by the more satisfactory but complicated profiles suggested by Cross (Reference 9).

$$\begin{aligned}\frac{U}{U_e} &= f_w(\zeta, U_\tau, Re_\delta) \cos \beta + CF_s(\zeta, \chi_s), \\ \frac{V}{U_e} &= f_w(\zeta, U_\tau, Re_\delta) \sin \beta + DF_c(\zeta, \chi_c),\end{aligned}\quad (5)$$

where $\zeta = z/\delta$, $U_\tau = \sqrt{\tau/C_f}$, $Re_\delta = U_e \delta/\nu$ is the Reynolds number based on δ , $\tan \beta = C_{fn}/C_{fs}$ and f_w is the standard law of the wall

$$\begin{aligned}f_w &= \frac{U_\tau}{0.41} [\ln(\zeta U_\tau Re_\delta) + 2.13], \\ F(\zeta, \chi) &= \sin^X(\frac{1}{4}\pi\zeta)\end{aligned}\quad (6)$$

is a modification of the Coles wake function (and allows for strong departures from equilibrium) and C and D are chosen to give $U/U_e = 1$, $V = 0$ at the edge of the boundary layer ($\zeta = 1$). So that

$$\begin{aligned}C &= 1 - \frac{U_\tau}{0.41} \cos \beta [\ln(U_\tau Re_\delta) + 2.13], \\ D &= (C - 1) \tan \beta.\end{aligned}\quad (7)$$

The exponents χ_s and χ_c are as given by Lock's (Reference 8) equation (132) and give improved representation of profiles with large values of β . With this family of profiles all the integral thickness ratios δ_1/δ , θ_{1j}/δ can be expressed as functions of U_τ , Re_δ and β and no additional $H_1(H)$ relationship and skin friction law are required. The dependent variables of the method are δ , U_τ and β .

4.1.2.3 ONERA method

This uses the velocity profiles suggested by Le Balleur^{3,10-14}. He replaces the wake functions F_s and F_c of equation (5) with the single function

$$F(\zeta, \zeta^*) = \left(1 - \frac{\zeta - \zeta^*}{1 - \zeta^*}\right)^{3/2},$$

where ζ^* is a quasi-linear function of δ_1/δ , based upon the computation of the 2D mixing layer, which is non zero only for grossly separated flows ($\beta > 90^\circ$). The dependent variables of the method are δ , δ_1/δ and δ_2/δ . The entrainment coefficient, C_E , is given by an analytic expression deduced from the velocity profiles with a mixing length assumption, and is then based upon equilibrium flows properties. At present, two transport integral equations (Reference 12) for non-equilibrium effects can be used only in two-dimensional flows. Minor corrections are added to C_E at low Reynolds number and low shape parameter. No additional $H_1(H)$ relationship and skin friction law are required.

4.1.2.4 ONERA/CERT method

Here following Cousteix (References 15 and 16) the relationships between the integral thicknesses are obtained from an analysis of similarity solutions. These similarity solutions are constructed by using a mixing length model which has been modified to account for the fact that the turbulent shear stress is not aligned with the mean velocity gradient $\partial q/\partial z$. These effects are represented by a factor T where $T = \tan(\gamma_r - \gamma)/\tan(\gamma_g - \gamma)$; γ , γ_g and γ_r are the directions of the velocity, the velocity gradient and the turbulent shear stress respectively. T is a constant for a particular calculation. The dependent variables of the method are θ_{11} , θ_{21} and $(\delta - \delta_1)$ (or their equivalents in the general x, y coordinate system). The entrainment coefficient is derived from the similarity solutions and once again no additional $H_1(H)$ relationship or skin friction law are required.

4.1.3 Numerical methods

All the integral methods of section 4.2 use the general, non-orthogonal coordinate system (x,y) on the body surface. The results of inserting the assumptions detailed in section 4.2 into equations (1) to (3) and then transforming to the x,y system may be written schematically in matrix form as

$$A_{ij} \frac{\partial F_j}{\partial x} + B_{ij} \frac{\partial F_j}{\partial y} = C_i, \quad (i,j = 1,2,3) \quad (8)$$

where F_j is the vector of unknowns (eg θ, H, δ for Smith's method) and the A_{ij} , B_{ij} and C_i are functions of the unknowns, the geometry of the x,y system and the angle α . The right-hand sides C_i are in addition functions of the external velocity U_∞ which is assumed to be known. For attached flows the system (8) is hyperbolic and can be solved as an initial value problem by a marching procedure. The bounding characteristics of these equations lie roughly in the directions of the external and surface streamlines, ie inclined at angles α and $\alpha + \beta$ respectively to the x axis.

The numerical methods of Smith, RAE, and Gleyzes, ONERA/CERT, are similar in that both are explicit and approximate the y derivatives of equation (8) by finite differences (backward if α and $\alpha + \beta$ are of the same sign, central if α and $\alpha + \beta$ are of opposite sign) and then integrate the resulting systems of ordinary differential equations with respect to x by standard methods (two step Euler, Smith; fourth order Runge Kutta, Gleyzes). In both methods the x step is chosen to satisfy both accuracy and stability (CFL) requirements.

Le Balleur et al, use the second order explicit MacCormack scheme, involving central differences for the y derivatives, which they have found to be more robust than the above method. In addition once either of the characteristic angles, α or $\alpha + \beta$, become large x marching may become impossible and Le Balleur has developed a "Multi-Zonal-Marching" method in which, where necessary, marching in both $\pm x$ and $\pm y$ directions is employed, reference 10.

Usually it is necessary to supply boundary conditions at the lateral (y) boundaries of the computation if any fluid is entering the computational domain through these boundaries. In the case of the ellipsoid, this is not necessary since the flow may either be considered to be periodic in y , or the boundaries may be assumed to be planes of symmetry.

REFERENCES

1. Smith, P.D., "The Numerical computation of three-dimensional boundary layers", IUTAM Symposium on three-dimensional turbulent boundary layers, Berlin 1982, H.H. Fernholz, E. Krause eds. Springer-Verlag 1982.
2. Lock, R.C. and Williams, B.R., "Viscous-inviscid interactions in external aerodynamics", Prog Aerospace Sci, Vol 24, pp 51-171, 1987.
3. LeBalleur, J.C., "Numerical flow calculation and viscous-inviscid interaction technique", Viscous Flow Computational Methods, W.C. Habashi ed, Pineridge Press, Swansea 1984.
4. Smith, P.D., "An integral prediction method for three-dimensional compressible turbulent boundary layers", ARC R&M 3739, 1972.
5. Smith, P.D., "Calculations with the three-dimensional lag-entrainment method", Proc SSPA-ITTC Workshop on Ship Boundary Layers 1980, Lars Larsson ed, SSPA No.90, 1981.
6. Green, J.E., Weeks, D.G. and Brooman, J.W.F., "Prediction of turbulent boundary layers and wakes in compressible flow by a lag-entrainment method", ARC R&M 3791, 1973.
7. Mager, A., "Generalisation of the boundary layer momentum integral equations to three-dimensional flows, including those of rotating systems", NACA Report 1067, 1951.
8. Lock, R.C., "Prediction of the drag of wings at subsonic speeds by viscous/inviscid interaction techniques", AGARD-R-723, Paper 10, 1985.
9. Cross, A.G.T., "Calculation of compressible three-dimensional turbulent boundary layers with particular reference to wings and bodies", BAe (Brough) Report YAD 3379 (1979).
10. Le Balleur, J.C. and Lazareff, M., "A multi-zonal-marching integral method for three-dimensional boundary layer with viscous-inviscid interaction", Proc 9th ICNMF Conf of 1984, Lecture Notes in Physics, Vol 218, Springer-Verlag 1985.
11. Lazareff, M. and Le Balleur, J.C., "Computation of three-dimensional flows by viscous-inviscid interaction using the 'M2M' method", AGARD CP412, Paper 24, 1986.
12. Le Balleur, J.C., "Strong matching method for computing transonic viscous flows including wakes and separations", Lifting airfoils, La Recherche Aerospaciale, 1981-3, pp 21-45, English ed.
13. Le Balleur, J.C., "Viscous-inviscid interaction solvers and computation of highly separated flows", Studies of vortex dominated flows, ICASE Symp 1985, Chap 3, pp 159-192, Springer-Verlag, 1987, Hussaini-Salas ed.
14. Le Balleur, J.C., "Numerical viscous-inviscid interaction in steady and unsteady flows", Proc 2nd Symp Numerical Physical Aspects Aero Flows 1983, Chap 13, Springer-Verlag 1983, Cebeci ed.
15. Cousteix, J., "Theoretical analysis and prediction method for a three-dimensional turbulent boundary layer", ONERA NT 157 (1974) English translation ESA TT-238, January 1976.
16. Cousteix, J., "Three-dimensional boundary layers", Introduction to calculation methods, AGARD Report No.741, 1987.

4.2 Field methods

D.A. Humphreys, B. van den Berg and T. Cebeci

A non-orthogonal curvilinear coordinate system (x,y,z) , useful for discussion purposes, has been defined in section 4a.1 above. Before describing the individual programs though, because one of them is based on rather unconventional assumptions, it might be appropriate to recall here a little of the background to the subject.

The system of boundary layer differential equations solved in field methods is a subset of the exact Reynolds equations. The method of deriving the turbulent boundary layer equations, although well supported by experimental evidence, is necessarily heuristic when the turbulence is represented only by empirical formulae. For laminar flow mathematically rigorous procedures can be applied and in that case lead to the same simplifications as given by the heuristic method.

The essence of the boundary layer concept is probably contained in the observation that, with the very high Reynolds numbers fortunately prevailing in aircraft aerodynamics, diffusion parallel to the wall tangent plane is quite negligible and exactly zero at the surface. The rigorous arguments indicate that after suitable normalising, and supposing the Reynolds number to be large and the wall curvature to be small, the terms which are less than order unity are dominated by terms of order $K\delta$ or δ^2 , where K stands for the maximum curvature of any local perpendicular section through the wall and δ is the local boundary layer thickness. The first order Prandtl equations consist of the $O(1)$ terms alone and the second order equations retain the $O(K\delta)$ terms but reject those of order δ^2 ; this imposes a consistency limit on the magnitude of the permitted wall curvature¹. Both sets of boundary layer equations are parabolic and in steady flow can be solved numerically by space marching, given the requisite flow-defining initial and boundary data. In the second order theory the pressure variation normal to the wall which is associated with the centrifugal force arising through wall curvature emerges as part of the boundary layer calculation, but in general this would not include the pressure field caused by streamline curvature near separation from a flat wall nor that induced for instance by longitudinal vorticity.

A thorough analysis of boundary layer calculation methods as such has recently been carried out in another context². It appears that modern methods are superficially very similar and in order to differentiate clearly one from another it is an advantage to be able to break them down into a series of logical steps and compare how each elementary task is treated. A similar procedure was adopted in a separate document³ prepared as a standardised information source for the present chapter. This document, together with the original references should be consulted if a more complete prescription of a calculation method and its general capabilities are sought. Only essentials will be repeated here, concentrating on what was actually done to obtain the results appearing in this report.

There are five field methods to describe and, as in chapter 4a, the methods will be referred to by the organisation where they were devised: AVA, Göttingen; DAC, Long Beach; FFA, Stockholm; MBB, München, and NLR, Amsterdam. The MBB method solves the second order boundary layer equations whereas the other four treat the usual first order Prandtl equations. Two test configurations have been treated: the ellipsoid at 10° incidence, which since the Mach number is only about 0.16 may be regarded as an incompressible flow, and the NASA wing "C". All five methods were applied to the ellipsoid flow. Only the DAC method was used for wing C and then the energy equation was solved in addition to the compressible Prandtl equations. Towards the rear of the ellipsoid the boundary layer thickness becomes quite appreciable in relation to the radius of the body cross section and the question arises: should the metric coefficients be allowed to vary with distance from the wall as is usual with programs written for axis-symmetric flow over bodies of revolution? In the MBB method the variation was included, but neglected in the others. The principal originator-references where general descriptions of the field methods can be found are AVA [4], DAC [5, 6], FFA [7], MBB [8, 9, 10] and NLR [11].

The next subsection concerns the turbulence models. Then follows a definition of the principal numerical methods used for the computed results. Initial and boundary conditions are reserved for the chapter discussing results, because they constitute the flow definition for computational purposes and say little about the method. On the other hand a note on computational effort, intimately connected with numerics, is appended to the present chapter.

4.2.1 Turbulence models

The turbulence models used were algebraic, all of mixing length or eddy viscosity type. For ordinary attached three-dimensional turbulent boundary layers it is believed that the sophisticated models which are sometimes proposed for practical calculation methods⁴, while certainly implying gross increases in computer time, cannot in general be relied upon to improve the quality of results obtained. However, it is equally certain that simple extensions to three dimensions of the algebraic models developed from observations in undisturbed fully developed two-dimensional flow are not generally adequate¹². The flows under consideration here are at high enough Reynolds numbers for well developed turbulence to be expected but some of the other factors which could generate first order modifications to the turbulence are

"2D": longitudinal pressure gradient
longitudinal wall curvature
transverse wall curvature

"3D": streamline convergence
swirl
eddy viscosity anisotropy

Of these the influence of the pressure gradient was included in the AVA, DAC and NLR methods, not in the other two. None of the remaining effects was modelled. The equations used may be given as follows, assuming streamline coordinates.

AVA and DAC methods [Refs. 13, 5 and 2]

$$z < z_c: \quad \nu_T = \epsilon_1^2 \left[\left(\frac{\partial u}{\partial z} \right)^2 + \left(\frac{\partial v}{\partial z} \right)^2 \right]^{1/2} \quad (4b:1)$$

$$z_c < z: \quad \nu_T = \epsilon_1 r_1 \delta_1^* u_e \quad (4b:2)$$

where

$$\epsilon_1 = \kappa_1 z [1 - \exp -z^+ N_1 / A_1^+] \quad (4b:3)$$

$$\kappa_1 = 0.4 \quad (4b:4)$$

$$z^+ = u_\tau z / \nu \quad (4b:5)$$

$$N_1 = (1 - 11.8 p_1^+)^{1/2} \quad (4b:6)$$

$$A_1^+ = 26.0 \quad (4b:7)$$

$$u_\tau^2 = \tau_w / \rho \quad (4b:8)$$

$$p_1^+ = \frac{\nu u_e}{u_\tau^2} \frac{\partial u_e}{\partial x} \quad (4b:9)$$

$$\epsilon_1 = 0.0168 \quad (4b:10)$$

$$r_1 = [1.0 + 5.5(z/\delta)^*]^{-1} \quad (4b:11)$$

$$\delta_1^* = \left| \int_0^z \left(1 - \frac{u}{u_e} \right) dz \right| \quad (4b:12)$$

$$u_e^2 = u^2 + v^2 \quad (4b:13)$$

τ_w is the total wall shear stress and ν is the kinematic viscosity evaluated at the wall.

FPA method [Refs. 14 and 7]

$$z < z_c: \quad \nu_T = \epsilon_2^* \frac{\partial u_c}{\partial z} \quad (4b:14)$$

$$z_c \leq z: \quad \nu_T = \epsilon_2 \gamma_2 \delta_2^* u_c \quad (4b:15)$$

where

$$\epsilon_2 = \kappa_1 z [1 - \exp -z^+/A_1^+] \quad (4b:16)$$

$$\epsilon_2 = 1/60 \quad (4b:17)$$

$$\delta_2^* = \int_0^z (1 - \frac{u}{u_c}) dz \quad (4b:18)$$

MBS method [Ref. 15]

$$z < z_c: \quad \nu_T = \epsilon_2^* u \quad (4b:19)$$

$$z_c \leq z: \quad \nu_T = \epsilon_1 \gamma_2 \delta_3^* u_1 \quad (4b:20)$$

where

$$\gamma_2 = [1.0 + 5.5(0.3z/z_{\max})^2]^{-1} \quad (4b:21)$$

$$\delta_3^* = 1.6z_{\max} \quad (4b:22)$$

$$u_1 = W \min(1, (u_c/W)^2/4) \quad (4b:23)$$

u is the magnitude of the vorticity, W is the maximum value of the quantity ϵ_2^*/κ_1 (considered as a function of z) and z_{\max} is the location of its maximum.

NLR method [Refs. 11 and 2]

$$\text{All } z: \quad \nu_T = \epsilon_3^* [(\frac{\partial u}{\partial z})^2 + (\frac{\partial v}{\partial z})^2]^{1/2} \quad (4b:24)$$

where

$$\epsilon_3 = \kappa_2 z [1 - \exp -z^+/A_2^+] T_1 \quad (4b:25)$$

$$\kappa_2 = 0.41 \quad (4b:26)$$

$$W_2 = (1 - 10 p_2^+)^{1/2} \quad (4b:27)$$

$$A_2^+ = 24.5 \quad (4b:28)$$

$$p_2^+ = \frac{\nu u_c}{u_\tau^2} \frac{\partial u_c}{\partial x_w} \quad (4b:29)$$

$$T_1 = T(\eta_1) \quad (4b:30)$$

$$T(\eta) = \eta^{-1} \tanh \eta \quad (4b:31)$$

$$\eta_1 = \frac{\kappa_2 z}{0.11 \delta_T} \quad (4b:32)$$

x_w is taken in the direction of the wall shear stress vector and δ_T is the value of z where $u_c = 0.95 u_c$.

4.2.2 Numerical methods

The asymptotic discretisation errors of the calculation methods have the orders of magnitude shown in Table 1.

Table 1 Orders of accuracy

Method	x	y	z
AVA	2	2	2
DAC	2	2	2
FFA	1	1	1
MBS	2	2	1
NLR	1	1	2

As is well known, the orders of accuracy give a measure of how fast the local discretisation error diminishes as the step length goes to zero and do not in themselves carry any information on the size of the local error attached to any individual step length taken in isolation. First order methods can therefore be more accurate in practice than second order ones. It is usually an unfortunate fact that increasing the discretisation error order also reduces stability. The difficult question of numerical stability will not be treated, but some relevant discussion of it can be found in References 2 and 16, for example.

As with the orders of accuracy, the integration algorithms are conveniently summarised in tabular form.

Table 2 Integration schemes

Method	perpendicular	tangential
AVA	KB	ZZ
DAC	KB	CB or SB
FFA	IE	LW
MBS	?	?
NLR	IE	DS or LS

The schemes represented in Table 2 have been abbreviated as follows.

IE = Implicit Euler (Refs 17 and 14)
 KB = Keller box (Ref 18)
 CB = Characteristic box (Ref 19)
 DS = Dwyer/Sanders (Refs 2 and 20)
 LS = Leasonen/Shevelev (Refs 2, 21 and 22)
 LW = Lax/Wendroff type (Refs 23 and 7)
 SB = Standard box (Ref 19)
 ZZ = Zig-zag (Ref 24)

4.2.3 Computational grids and computing effort

In a comparison of boundary layer calculation methods carried out by Eurovisc at the Amsterdam Workshop²⁵, the required computational effort was deemed an important indicator of program performance. As computing power becomes cheaper this is a measure which is receiving less emphasis amongst boundary layer method developers, but nevertheless remains of interest, not least to prospective users. The speed of the computer in applications depends on many factors amongst which may be mentioned the type of operation being carried out and how the program being run is organised. The characteristic speed can be expressed in units of million floating point operations per second (Mflops) and is evaluated by computing standard problems with the same test program on the different machines which are to be compared. It is, however, difficult to devise a test program which is equally fair to all of the various machine architectures. In other words there is a large uncertainty (say a factor of two) associated with the resulting characteristic speeds.

Table 3 is in two parts. First is shown the computers on which the calculation methods were run, together with estimated characteristic machine performance figures for scientific applications. The second part lists the execution time achieved for each representative run and the computational grid to which this time relates. In the last column is the Effort defined as

$$\text{Effort} = \text{Mflops} \cdot \text{time/nodes}$$

(4b:33)

Table 3 Computational effort

Method	Machine	Speed (Mflops)	Execution time (sec)	Grid points			Total nodes	Effort
				x	y	z		
AVA	IBM 4381	0.86	?	100	36	50	180,000	?
DAC	CRAY XMP/2	24.0	60	?	?	60	?	?
FFA	Cyber 170/730	0.22	1750	45	37	48	80,000	0.0048
MBB	VAX 8600	0.84	1500	81	81	51	335,000	0.0038
NLR	Cyber 180/855	2.0	34	40	36	20	29,000	0.0023

The figures for effort are all quite similar but the NLR method seems to stand out and it is indeed true that when it was designed a decade ago computational efficiency was made an important part of the specification. This is not so for the other methods in the table, which are of more recent origin. However, it is an interesting illustration of inherent uncertainties involved that in the Eurovisc exercise²⁵, referred to above, the corresponding Effort obtained for the NLR method on a different computer was found to be 0.0052.

4b REFERENCES

- Goldstein, S., "Modern developments in fluid dynamics", Vol 1. New York, Dover Publications, 1968.
- Humphreys, D.A. and Lindhout, J.P.F., "Calculation methods for three-dimensional turbulent boundary layers". To appear in Prog. Aerospace Sci., 1988.
- Humphreys, D.A., "Field methods for computing high Reynolds number viscous flow". FFA TN 1988-01, 1988.
- Menter, F., "Three-dimensional boundary layer computations for the AGARD Working Group 10". DFVLR IB 222-87 A20, 1987.
- Cebeci, T. and Meier, H.-U., "Turbulent boundary layers on a prolate spheroid". AIAA-87-1299, 1987.
- Cebeci, T. and Su, W., "Separation of three-dimensional laminar boundary layers on a prolate spheroid". To be published in J. Fluid Mech., 1988.
- Humphreys, D.A., "A calculation of the turbulent boundary layer on a slender ellipsoid at low incidence". FFA TN 1988-02, 1988.
- Monnoyer, F., "The effect of surface curvature on three-dimensional, laminar boundary layers". Doctoral Thesis, Université Libre de Bruxelles, 1985.
- Monnoyer, F., "SOB2D, a FORTRAN program for the calculation of two-dimensional boundary layers". MBB-LKE122-AERO-MT 780, 1987.
- Monnoyer, F., "SOBOL, a computer program for the calculation of three-dimensional second order boundary layers". Paper in preparation, 1988.
- Lindhout, J.P.F., Moak, G., de Boer, E. and van den Berg, B., "A method for the calculation of 3D boundary layers on practical wing configurations", NLR MP 79003, 1979.
- van den Berg, B., Humphreys, D.A., Krause, E. and Lindhout, J.P.F., "Three-dimensional turbulent boundary layers. Calculation and experiment". The EUROVISc Berlin Workshop. NLR MP 86023, 1985.
- Cebeci, T. and Smith, A.M.O., "Analysis of turbulent boundary layers". Academic Press, New York, 1974.
- Fanneleop, T.K. and Humphreys, D.A., "The solution of the laminar and turbulent three-dimensional boundary layer equations with a simple finite difference technique". FFA Report 126, 1975.
- Baldwin, B.S. and Lomax, H., "Thin layer approximation and algebraic model for turbulent separated flows". AIAA-Paper 78-257, 1978.
- Humphreys, D.A., "Viscous flow - its analysis and computation." FFA Report 142. Stockholm, 1986.

- 17 Flugge-Lotz, I. and Blottner, F.G., "Computation of the compressible laminar boundary layer flow including displacement thickness interaction using finite difference methods." Stanford University, Division of Engineering Mechanics, Tech. Rep. No. 131, 1962.
- 18 Keller, H.B., "A new difference scheme for parabolic problems." In: Numerical solution of partial differential equations - II. SYNSPADE (Ed: B. Hubbard). pp 327-350. Academic, New York, 1971.
- 19 Cebeci, T., Khattab, A.A. and Stewartson, K., "Prediction of three-dimensional laminar and turbulent boundary layers on bodies of revolution at high angles of attack". Proc. 2nd. Symp. Turbulent Shear Flows, Imperial College, London, 1979.
- 20 Dwyer, H.A. and Sanders, B.R., "A physically optimum difference scheme for three-dimensional boundary layers." Proc. 4th Int. Conf. Num. Meth. Fluid Dyn., Boulder, Colo., June 24-28, 1974. New York, 1975.
- 21 Laasonen, P., "Über eine Methode zur Lösung der Wärmeleitungsgleichung." Acta Mathematica., Vol 18, pp 309-317, 1949.
- 22 Shevelev, Yu.D., "Numerical calculation of the three-dimensional boundary layer in an incompressible fluid." Fluid dynamics, Vol 1, No. 2, pp 77-80, 1966.
- 23 Humphreys, D.A., "Stability domains for a discretisation of the 3D boundary layer Equations." FFA Memorandum, FFAP-A-662, 1986.
- 24 Krause, E., Hirschel, E.H. and Bothmann, T., "Die numerische Integration der Bewegungsgleichungen dreidimensionaler laminarer kompressible Grenzschichten." DVL, Rep. No. 915, 1969.
- 25 Lindhout, J.P.F., van den Berg, B. and Elsenaar, A., "Comparison of boundary layer calculations for the root section of a wing". The September 1979 Amsterdam Workshop test case. NLR MP 80028, 1980.

CHAPTER 5. TEST CASE DATA BASE

5.1 Experimental

5.1.1 Description of the DFVLR prolate spheroid and its instrumentation

H.U.Meier and H.-P.Kreplin, DLR, Institut für Exp. Strömungsmechanik,
Bunsenstr. 10, D-3400 Göttingen, Federal Republic of Germany

INTRODUCTION

The wind tunnel model, especially designed for the investigation of three-dimensional boundary layers essentially consists of a 1:6 prolate spheroid. This configuration was chosen for the following reasons:

- the flow pattern around an inclined prolate spheroid is characteristic for fuselages and missile shapes,
- the geometry of this body of revolution can easily be described applying orthogonal or non-orthogonal coordinate systems,
- the potential flow is given - even for the inclined version - by closed analytical solutions [1],
- the complete instrumentation like probe traversing mechanism, hot film anemometers, pressure transducers etc. can be stored in the model,
- as the model can be turned around its longitudinal axis, the pressure distribution, the wall shear stress, and the boundary layer quantities can be measured in each cross section for arbitrary small steps of the circumferential angle ϕ with the same surface pressure orifice, surface hot film and boundary layer probe, respectively.

1. THE WIND TUNNEL MODEL

The essential construction of the ellipsoid is based on two half-shells of glass fiber reinforced resin with a wall thickness of about 4 mm. The dimensions of the model are given in Fig. 1, which shows the test arrangement in the 3m x 3m Low Speed Wind Tunnel of the DFVLR-AVA.

The model can be turned around its longitudinal axis through $\phi = 0^\circ$ to 360° with a resolution of $\Delta\phi = 0.8^\circ$ by means of a step motor. For one particular investigation in the DFVLR 3m x 3m Low Speed Wind Tunnel a transition strip was mounted at $x_0/2a = 0.2$. The strip was about 20 mm wide and consisted of carborundum (sand paper grain) with an average diameter of 0.7 mm, which was blown onto liquid glue on the model surface (for more details see Ref. [2]).

The construction and manufacturing of a new prolate spheroid for the investigations in the ONERA F1 pressurized wind tunnel, LeFauga, became necessary due to the seven times higher maximum dynamic pressure in the F1 compared to the Göttingen facility. The objectives of the DFVLR-ONERA cooperation were to extend the detailed DFVLR investigations on the prolate spheroid to much higher Reynolds numbers.

2. WALL SHEAR STRESS MEASUREMENTS BY MEANS OF SURFACE HOT FILMS

For the present tests two prolate spheroids built for the DFVLR 3m x 3m Low Speed Wind Tunnel (NWG) and for the ONERA F1 Wind Tunnel were equipped with 12 surface hot films. The x_0 -positions of the flush mounted surface hot films differ only slightly on the two models while the ϕ -positions are completely different, see Fig. 2. The commercially available surface hot film probes, see Fig. 3, were originally designed by McCroskey [3] for the investigation of helicopter rotor blades. Each probe consists of two mutually perpendicular films in V-configuration on a thin plastic foil. The dimensions of the hot films are given in Fig. 3. Extreme care was taken to mount the hot films on the model surface in order to avoid an imposed boundary layer transition caused by artificial roughness. The measured imperfection of the model surface in the regime of the hot films is smaller than 10 μm . The films of the probes were operated simultaneously by 24 Constant Temperature Anemometers developed and built at DFVLR, Göttingen. These anemometers were located inside the prolate spheroid in order to avoid very long probe cables in the bridges. The overheat ratio of the films was adjusted to an operating film temperature of about 120°C.

A block diagram of the electronic equipment and data acquisition system used for the DFVLR and ONERA tests is given in Figs. 4 and 5, respectively. A detailed description of the test set up and measuring procedure in the DFVLR 3m x 3m Low Speed Wind Tunnel is given in Refs. [4], [5] and for the ONERA F1 facility in Refs. [6], [7].

Due to the V-configuration of the films the surface hot film probes can be used for the measurement of the magnitude and direction of the local wall shear stress. Changes in the local wall shear stress (magnitude and/or direction) result in changes of the local hot film transfer, which is indicated by changes of the anemometer voltage E . The heat transfer per unit temperature difference is used in the calibration and data reduction procedure. This quantity is given by:

$$Q = \frac{I^2 R_F}{T_F - T_{Ref}} \quad \text{with } E = I R_F.$$

The average value for the free stream and wall temperatures was used as the reference temperature T_{Ref} . While the hot film resistance R_F and temperature T_F are kept constant by the anemometer, the reference temperature in the wind tunnel may change with time so that the measured free stream and the model wall temperature correction are performed automatically, which is sufficient for temperature changes of a few degrees as observed in the experiments reported here.

According to Ref. [3] the wall shear stress magnitude τ_w is derived from the sum of the heat transfer rates of the films of each probe, $Q_s = Q_1 + Q_2$. The measured values of Q_s were related to calculated wall shear stress values by the following procedure:

For zero angle of incidence the mean values of the hot film signals were measured at different Reynolds numbers ($Re = U_\infty 2a / \nu_\infty$). These measured values were related to theoretical wall shear stress values τ_w , calculated with a boundary layer computer program of J.C. Rotta [8] for the given flow conditions. The calculations were based on the measured pressure distribution and the experimentally determined transition locations. The transition was clearly indicated by the drastic increase of the anemometer voltages and by fluctuations in the hot film signals without a calibration of the probes. Only the laminar and fully turbulent boundary layers were considered for the calibration procedure, because the transition region is not described correctly by the theory. The hot film calibration curves obtained in this axisymmetric boundary layer flow were applied for the evaluation of the local wall shear stress in three-dimensional boundary layer flows. In order to be able to take small variations of the tunnel temperature into account, a calibration of the surface hot films was performed before and after each wall shear stress measurement at a given angle of incidence and free stream Reynolds number.

The directional sensitivity of the hot film probes could not be derived from a direct calibration on the prolate spheroid. For this reason the calibration was carried out on a flat tunnel wall in a two-dimensional turbulent boundary layer. As demonstrated in Ref. [4] a linear relation between the yaw angle γ_w and the hot film output signals was found for $-40^\circ \leq \gamma_w \leq 40^\circ$. This linear relationship was applied to the surface hot film probes in the data reduction procedure.

The error bound for the magnitude of the wall shear stress depends on several parameters like Reynolds number, temperature sensitivity (substrate), surface curvature, pressure gradient, and flow direction. For the reported tests the estimated accuracy of wall shear stress measurements with respect to the magnitude is

$$\Delta c_f \approx 0.1 |c_f|.$$

Of course, the variations of the wall shear stress can be measured much more accurate (within the order of 1 %). The determination of the wall shear stress direction mainly depends on the deviation of the calibration curve from its linearity:

$$\Delta \gamma_w \approx 0.1 |\gamma_w|.$$

WALL PRESSURE MEASUREMENTS

The model was equipped with 42 pressure taps positioned on one meridian in non-equidistant distances, compare Fig. 6. Due to the fact that the model could be rotated around its longitudinal axis in steps of $\Delta\phi \approx 0.8^\circ$ a sufficient spatial resolution in circumferential direction could be achieved.

The pressure taps have a small diameter ($d = 0.3$ mm) in order to avoid any orifice effects on the pressure measurement and to minimize the flow disturbance due to finite roughness. The pressure taps were connected to a pressure scanner (Scanivalve) located inside the model. For the experiments carried out in the Göttingen wind tunnel (NWG) the integration time for the pressure measurements was 2 seconds. The pressure integration started when the measured pressure value was indicated to be constant on an oscilloscope. It was checked that this test condition was reached after 1 second. This resulted in a necessary time for the measurement for all wall pressures on one meridian (42) at a constant circumferential angle ϕ of about 2 minutes. The corresponding pressures were measured with a 1000 Pa pressure-transducer manufactured by Hottinger (B110, 51). The zero shift was detected before each run ($\phi = \text{const}$) and taken into account in the data reduction procedure. Apart from small temperature changes inside the model, the zero shift of the pressure transducer was mainly caused by the change of the transducer position, if the model was rotated or inclined.

Details about the test arrangement for the pressure measurements in the ONERA F1 Wind Tunnel are given in [6].

The pressure distributions were measured in the Reynolds number range of $Re \approx 7 \times 10^6$ (DELTA) to 4×10^6 (ONERA).

pressure coefficient c_p was defined as

$$c_p = \frac{p_w - p_\infty}{\rho U_\infty^2 / 2}$$

where $p_w - p_\infty$ is the measured wall pressure minus the static pressure and $\rho U_\infty^2 / 2$ is the dynamic pressure, respectively (∞ denotes free-stream conditions). The static pressure distribution and misalignment of the free jet in the DFVLR 3m x 3m Low Speed Wind Tunnel, NWG, Göttingen is given in Ref. [9]. The measuring accuracy relative to $c_p = 1$ is:

$$\begin{aligned} \Delta c_p &= 0.005, & \text{ONERA: } p_0 &= 3.85 \text{ bar, } U_\infty &= 75 \text{ m/s} & \text{ and} \\ \Delta c_p &= 0.01, & \text{DFVLR: } p_0 &= 1 \text{ bar, } U_\infty &= 55 \text{ m/s.} \end{aligned}$$

4. BOUNDARY LAYER MEASUREMENTS

The model is equipped with a traversing mechanism, which allows vertical and horizontal movements of the probe. This traversing mechanism is installed inside the model in such a way that the vertical movement relative to the model surface is warranted. The accuracy of the vertical displacement measurement is in the order of 1/100 mm and the horizontal angle measurement is better than 0.4 degree.

The boundary layer measurements were carried out applying a Three-Hole-Direction-Probe with an outer diameter of each single tube of $d = 0.5$ mm and a yaw angle of 45° , compare Ref. [10]. This probe allows the determination of the magnitude and the direction of the local velocity. The directional sensitivity with respect to the angle of incidence α and the yaw angle γ was obtained in a two-dimensional channel flow of the DFVLR Low Turbulence Wind Tunnel. This calibration was checked during the tests positioning the probe in the free stream while the angle of incidence of the prolate spheroid was zero. In Ref. [10] the directional sensitivity of the Three-Hole-Probe for yaw angles of $\gamma = \pm 30^\circ$ and angles of incidence up to $\alpha = 10^\circ$ is given. These results indicated that the directional sensitivity is almost independent of the angle of incidence, as far as they are representative for our test conditions. This is not true for the total pressure measurement (p_t). The uncorrected pressure difference $p_t - p_\infty$, non-dimensionalized with the dynamic pressure, obtained at free-stream conditions, changes considerably as the probe is inclined with respect to the tunnel axis to $\alpha = 10^\circ$. However, for a first approximation in the boundary layer, the streamlines are parallel to the model surface which implies that the corrections can be assumed to be small. Due to the fact that during this test no upwash angles were measured in the boundary layers, an " α -correction" was not applied in the data reduction procedure. At this stage of investigation the static pressure was measured at the model surface and assumed to be constant through the entire boundary layer thickness. Errors could have been revealed, here, if thick boundary layers close to separation were investigated.

The data reduction procedure applied is described in Ref. [10].

Essentially, the resultant velocity can be derived by means of the Bernoulli equation, while the cross-flow angle γ is given by the pressure difference of the two "45 degree tubes". The measurement accuracy of the resultant velocity relative to the maximum velocity is

$$\Delta u_r = 0.01$$

while the directional accuracy is better than

$$\Delta \gamma = 1^\circ$$

in the linear regime of the calibration curve. For wall distances of $z < 1$ mm probe displacement effects have to be taken into account.

REFERENCES

- [1] D.K. Maruhn: Druckverteilung an elliptischen Rümpfen und in ihrem Außenraum. Jahrbuch der Luftfahrtforschung, pp. 135-147, 1941.
- [2] H.U. Meier, H.-P. Kreplin, X. Ming: Problems associated with artificial boundary layer transition. AIAA Paper No. AIAA-83-1673, 1983.
- [3] W.J. McCroskey, E.J. Durbin: Flow angle and shear stress measurements using heated films and wires. ASME J. Basic Eng. 94, pp. 46-52, 1972.
- [4] H.-P. Kreplin, H.U. Meier, A. Maier: Wind tunnel model and measuring techniques for the investigation of three-dimensional turbulent boundary layers. Proc. 10th AIAA Aerodyn. Testing Conf., San Diego, CA, Paper No. 78-781, 1978.
- [5] H.U. Meier, H.-P. Kreplin: Experimental investigations of the boundary layer transition and separation on a body of revolution. Z. Flugwiss. Weltraumforsch. 4, pp. 65-71, 1980.

- [6] J.C. Raynal, Ch. Pelissier: Essai dans la soufflerie F1/CFM d'un ellipsoïde de révolution du DFVLR (Etude 1147 AN 171 G). Procès verbal d'essais 1/7252 ANG, 1983.
- [7] H.-P. Kreplin, H.U. Meier, H. Vollmers: Wall shear stress measurements on an inclined prolate spheroid at zero incidence in the ONERA F1 Wind Tunnel - Data report. DFVLR, IB 222-84 A 34, 1984.
- [8] J.C. Rotta: FORTRAN IV - Rechenprogramm für Grenzschichten bei kompressiblen ebenen und achsensymmetrischen Strömungen. DLR-FB 71-51, 1971.
- [9] H.U. Meier, H.-P. Kreplin, A. Landhäuser: Wall pressure measurements on a 1:6 prolate spheroid in the DFVLR 3m x 3m Low Speed Wind Tunnel ($\alpha = 10^\circ$, $U_\infty = 55$ m/s, artificial transition) - Data report. DFVLR, IB 222-86 A 04, 1986.
- [10] H.U. Meier, H.-P. Kreplin, A. Landhäuser, D. Baumgarten: Mean velocity distributions in three-dimensional boundary layers, developing on a 1:6 prolate spheroid with artificial transition ($\alpha = 10^\circ$, $U_\infty = 55$ m/s, cross sections $x_0/2a = 0.48, 0.56, 0.64, 0.73$) - Data report, DFVLR, IB 222-84 A 11, 1984.



Fig. 1: Prolate spheroid for the investigation of three-dimensional boundary layers in the 3m x 3m Low Speed Wind Tunnel of the DFVLR, Göttingen.

Length of the model $2a = 2.4$ m
 Diameter of the model $2b = 0.4$ m
 Maximum angle of incidence $\alpha = 30^\circ$
 Maximum velocity $U_\infty = 62$ m/s
 Turbulence level $Tu_1 = 0.3$ %

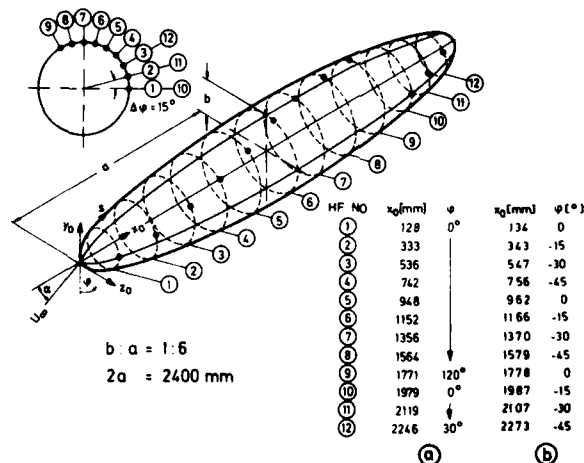


Fig. 2: Locations of the surface hot film probes in different cross sections on the prolate spheroid models used at the DFVLR (a) and ONERA (b) wind tunnels

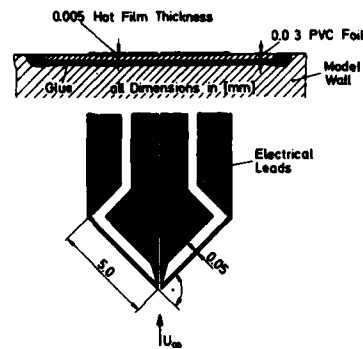


Fig. 3: Systematical sketch of a surface hot film probe

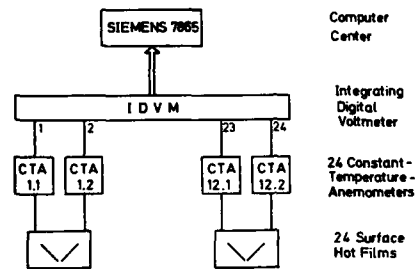


Fig. 4: Block diagram of the electronic equipment and data acquisition system used in the DFVLR 3m x 3m Low Speed Wind Tunnel

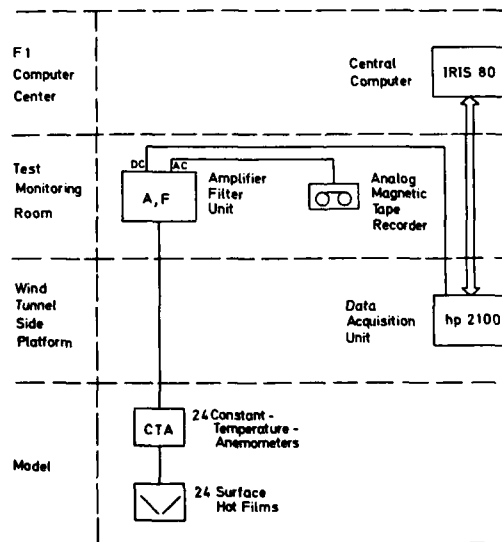


Fig. 5: Block diagram of the electronic equipment and data acquisition system used in the ONERA F1 Wind Tunnel

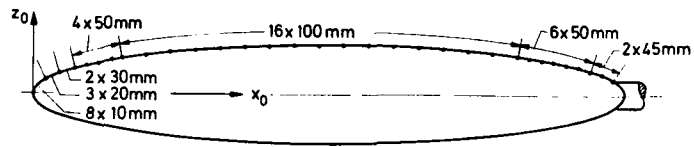


Fig. 6: Arrangement of the pressure taps on the prolate spheroid

5.1.2 Lockheed/NASA-Ames Wing C

H. Yoshihara
Boeing Company
Seattle, Washington

The second case chosen by WG 10 is Wing C at $M = 0.85$, 5 degrees angle of attack, and $Re. no. = 6.8 \times 10^6$ /mean chord. Wind tunnel measurements of the surface pressures and boundary layer velocity profiles have been obtained by Keener (Refs. 1 and 2). In the following the definition of the wing, details of the test, and the plots and tabulation of the test data taken from Refs. 1 and 2 are presented. In addition, calculations with the Transonic Navier/Stokes (TNS) code (Ref. 3) are given to illustrate the possible test/theory mismatches that can be expected.

2.1 Details of the Test and Test Data

The tests were carried out in the Ames 6 x 6 Foot tunnel which is a continuous flow facility having slotted upper and lower surface walls of 6% porosity. Geometric properties of the model are summarized in Figure 1. The wing was defined in terms of the root and tip chords with the intermediate sections defined by a linear development. The root and tip sections are shown in Figure 2, and their coordinates are given in Table 1. Since a definition of the wing tip was not provided, a shape as shown in Figure 1 was postulated. The wing was mounted on the tunnel sidewall directly as a semi-span model. Its semi-span of 0.9 meters resulted in a test-section blockage ratio of 1.3%. Details of the construction tolerances and the aeroelastic properties are given in Ref. 1. Surface pressures were obtained by a transducer-scanivalve system, while the boundary layer velocity profiles were obtained by a 3-hole "cobra head" flow direction probe with the traversing mechanism mounted through the wing. The location of the surface pressure taps and the velocity profile stations are shown in Figure 3. The boundary layer was tripped using sifted glass spherules located at the 4.5% chord station. The final determination of the trip configuration was determined using sublimation tests. On the lower surface and outboard of the 60% span station on the upper surface the trip size was 0.16 mm, while inboard of the 60% span station on the upper surface the trip size was 0.23 mm. Fluorescent oil flow pictures were also obtained.

The test data for $M = 0.85$ and 5° angle of attack are plotted in Figures 4 and 5 and tabulated in Tables 2 and 3.

2.2 Transonic Navier/Stokes Solution

Calculation for the above case using the TNS code was carried out earlier (Ref. 3). The Baldwin/Lomax equilibrium turbulence model was employed, and an approximate symmetry condition was imposed at the root chord plane. The calculations were therefore repeated with the exact symmetry condition implemented using an image plane. In Figure 6 the resulting chordwise pressure distributions are compared to the earlier Ref. 3 result and with the experimental result. Comparison of the two calculated results shows that the suction is significantly higher with the exact symmetry conditions in the upper surface peak and plateau regions with a smaller increase of the suction plateau on the lower surface. These effects of the symmetry condition extend over the entire span, such far-reaching influences being characteristic of high subsonic flows.

Surprisingly the less exact calculations agreed more closely with the experiments so far as the suction peaks and plateaus were concerned. A partial explanation for this is the distortion of the test data by the significant boundary layer displacement effect on the sidewall on which the wing is mounted. Such sidewall displacements will be compressive about the wing leading edge, depressing the suction in the upper surface peak and plateau regions over the entire span in much the same manner as the inexact symmetry conditions. In addition the consequences of the simplifications used in the diagonalization process in the TNS code, particularly in the leading edge region, need to be assessed. The remaining large test/theory mismatches, as at the 70% and 90% span stations, are most probably due to the inadequacy of the turbulence model and to the inadequate treatment of the tip flow. Thus for example the difference of the pressure distribution at the 70% station, namely the calculated single shock distribution compared to the measured double-shock distribution, stems from the inboard displacement of the forward and rear shock intersection by the inadequate turbulence model. The matter of the turbulence modeling, however, falls outside the scope of the WG 10.

The above calculations were carried out by G. Blum and T. Blum of the Boeing Company.

2.3 References

1. Keener, R., "Pressure Distribution Measurements on a Transonic Low-Aspect Ratio Wing," NASA TM 86683, 1985.
2. Keener, E., "Boundary Layer Measurements on a Transonic Low-Aspect Ratio Wing," NASA TM 88214, 1986.
3. Kaynak, U., Holst, T., and Cantwell, B., "Computation of Transonic Separated Wing Flows Using an Euler/Navier-Stokes Zonal Approach," NASA TM 88311, 1986.

POSTULATED TIP SHAPE

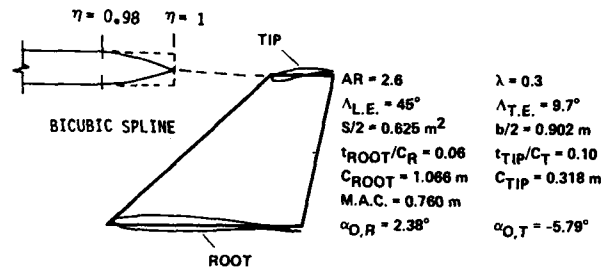


Figure 1. Geometric Definition of Wing C.

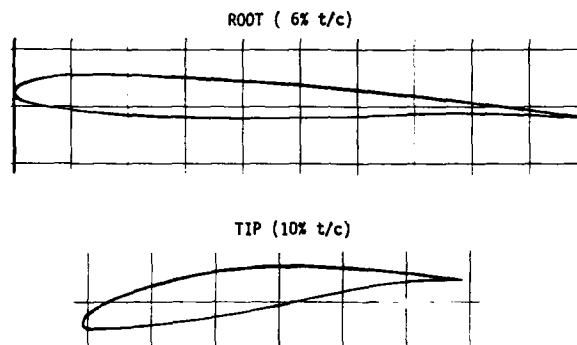


Figure 2. Defining Root and Tip Sections.

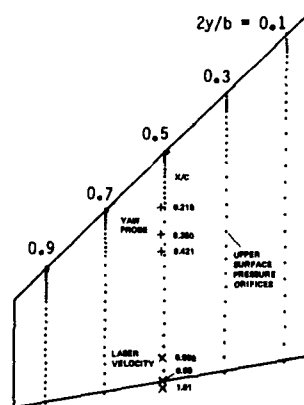


Figure 3. Location of Pressure Taps and Yaw Probes.

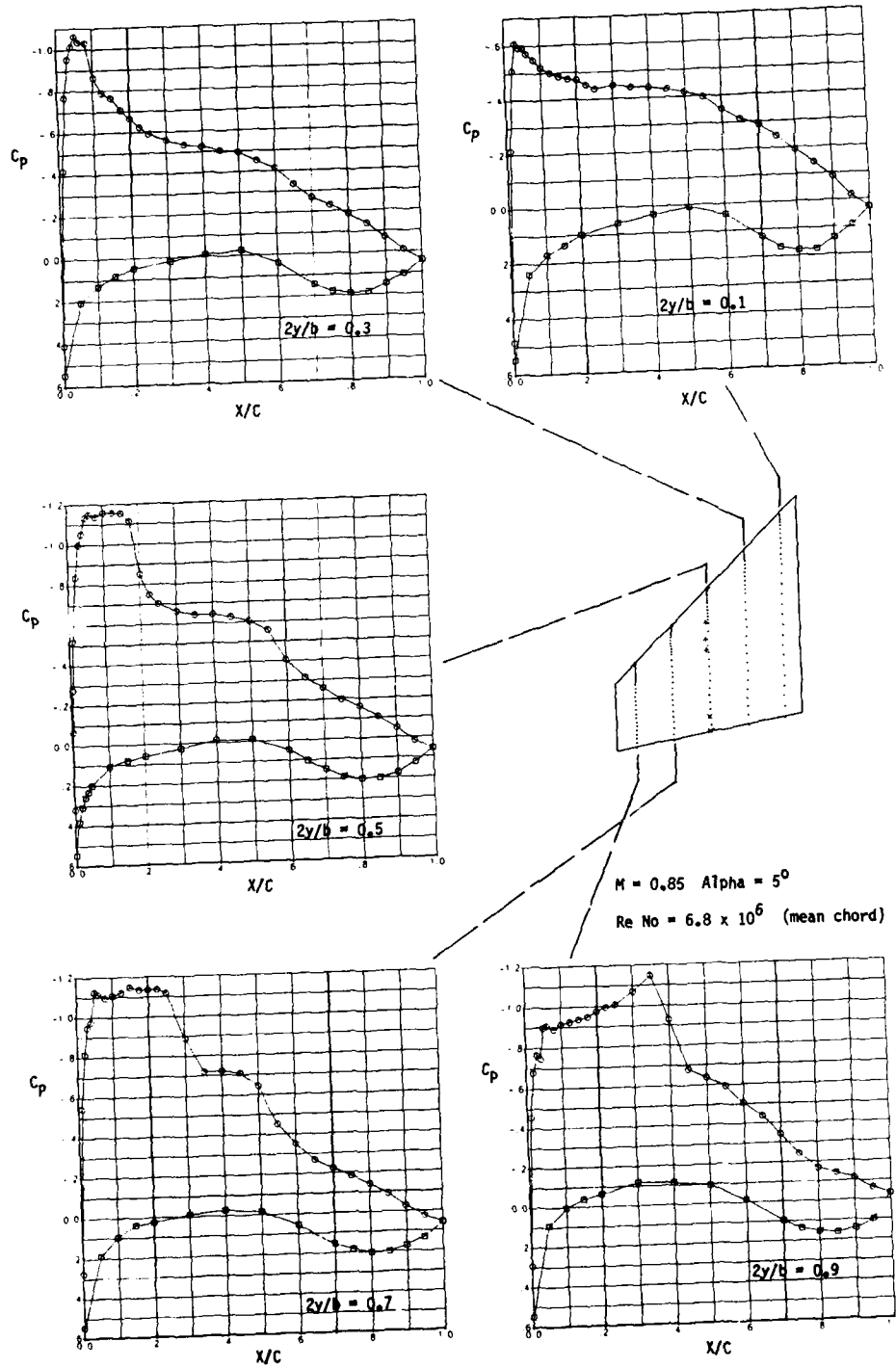


Figure 4. Measured Pressure Distributions - Wing C.

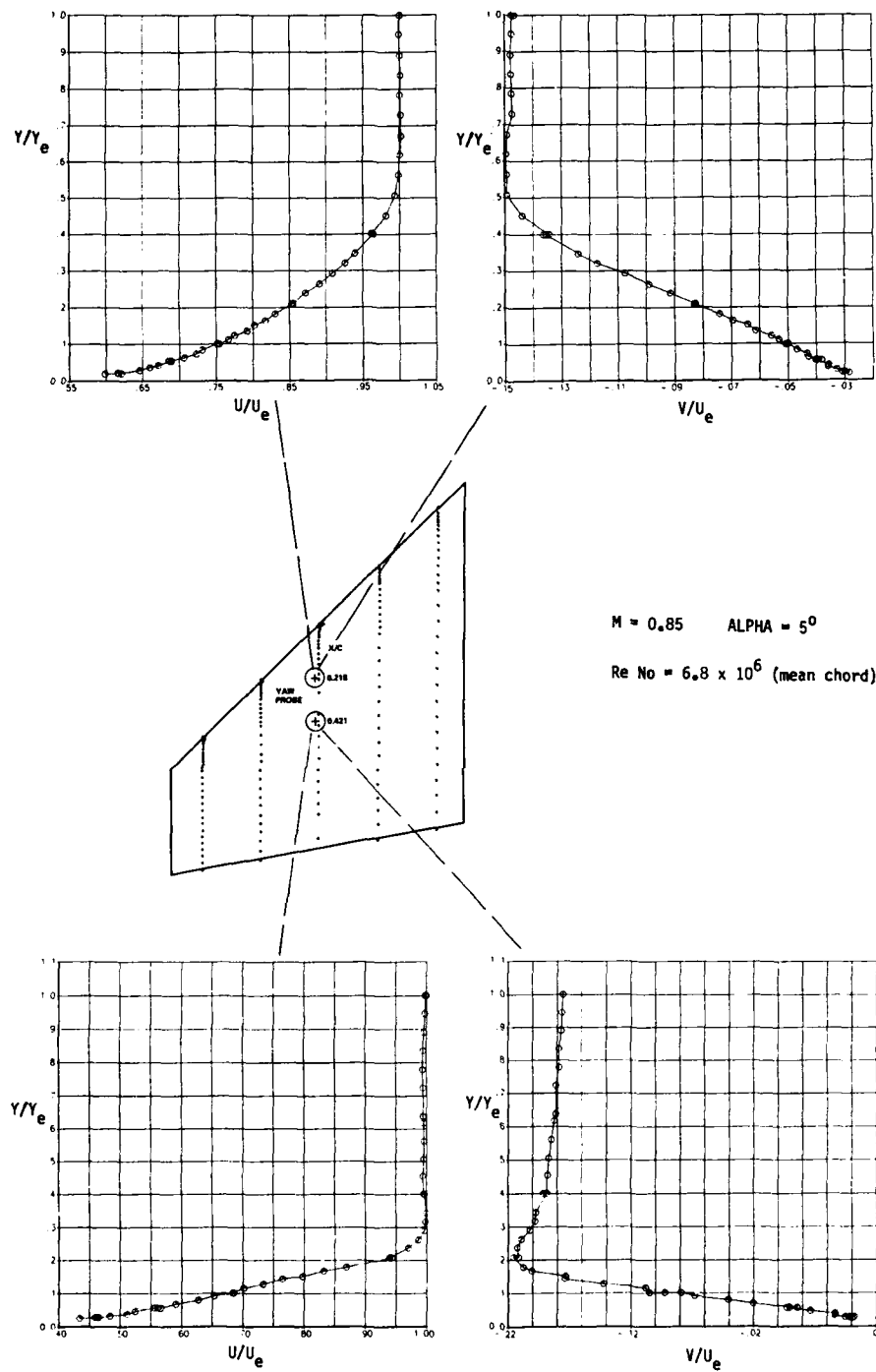


Figure 5. Velocity Profile Measurements ~, Wing C.

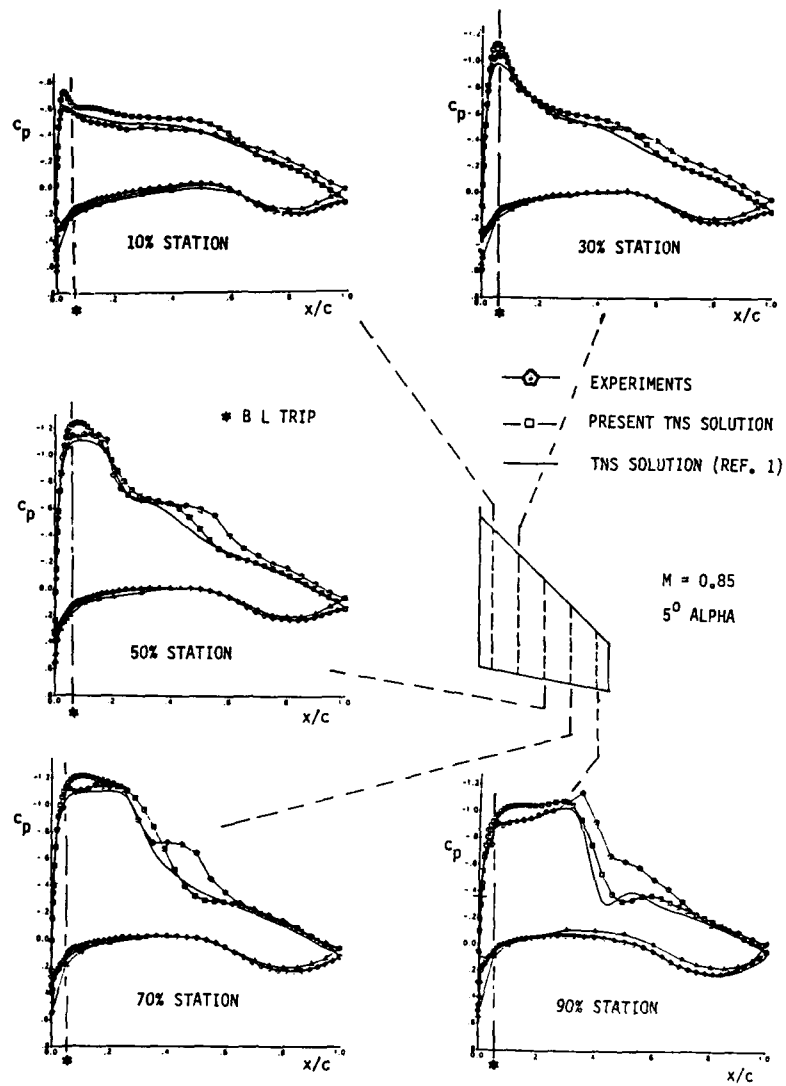


Figure 6. Chordwise Pressure Distributions - Wing C.

N	X/C	Root		Tip	
		Z/C _U	Z/C _L	Z/C _U	Z/C _L
1	0.00000	0.00000	0.00000	0.00000	0.00000
2	.00281	.00730	-.006025	-.00967	-.00503
3	.00961	.01542	-.009709	.01784	-.00941
4	.02153	.02261	-.012482	.02584	-.01284
5	.03806	.02830	-.015382	.03351	-.01480
6	.05904	.03285	-.018439	.04109	-.01696
7	.08427	.03653	-.020903	.04854	-.01863
8	.11349	.03928	-.022924	.05581	-.01995
9	.14645	.04115	-.024471	.06290	-.02089
10	.18280	.04221	-.025486	.06965	-.02130
11	.22221	.04261	-.026195	.07586	-.02142
12	.26430	.04253	-.026280	.08108	-.02101
13	.30866	.04202	-.025949	.08493	-.02023
14	.35486	.04109	-.025082	.08718	-.01884
15	.40245	.03982	-.023888	.08770	-.01704
16	.45099	.03812	-.022217	.08648	-.01462
17	.50000	.03613	-.020079	.08368	-.01172
18	.54901	.03384	-.017094	.07951	-.00798
19	.59755	.03135	-.013470	.07427	-.00362
20	.64514	.02864	-.009348	.06818	-.00112
21	.69134	.02584	-.005664	.06142	.00518
22	.73570	.02298	-.002667	.05418	.00825
23	.77779	.02006	-.000695	.04682	.01003
24	.81720	.01710	.000481	.03956	.01050
25	.85355	.01415	.000802	.03256	.00972
26	.88651	.01124	.000588	.02605	.00807
27	.91573	.00855	.000108	.02016	.00589
28	.94096	.00618	.000269	.01491	.00362
29	.96194	.00422	.000561	.01049	.00142
30	.97847	.00272	.000598	.00701	-.00028
31	.99039	.00172	.000501	.00452	-.00141
32	.99759	.00110	.000698	.00315	-.00233
33	1.00000	.00082	-.000821	.00270	-.00270

TABLE 1
AIRFOIL
COORDINATES

TABLE 3
VELOCITY
PROFILES

X/C= 0.218 YE= 0.346 in, JE= 1215 in/s			X/C= 0.421 YE= 0.345 in UE= 1179 in/s		
Y/YE	U/UE	W/UE	Y/YE	U/UE	W/UE
.0258	.4339	.0608	.0199	.5983	-.0284
.0286	.4623	.0624	.0210	.6164	-.0300
.0286	.4591	.0549	.0207	.6209	-.0308
.0283	.4649	.0579	.0210	.6156	-.0299
.0329	.4837	.0464	.0287	.6457	-.0328
.0386	.5111	.0466	.0362	.6596	-.0350
.0466	.5248	.0263	.0416	.6715	-.0358
.0566	.5558	.0072	.0548	.6891	-.0404
.0563	.5611	.0095	.0551	.6886	-.0398
.0566	.5662	.0157	.0545	.6858	-.0382
.0686	.5904	-.0274	.0637	.7053	-.0429
.0800	.6270	-.0406	.0734	.7224	-.0434
.0922	.6531	-.0680	.0846	.7306	-.0469
.1014	.6852	-.0788	.1003	.7509	-.0500
.1016	.6843	-.0924	.1000	.7527	-.0504
.1014	.6836	-.1047	.0992	.7541	-.0508
.1165	.7018	-.1079	.1115	.7666	-.0532
.1282	.7333	-.1425	.1221	.7747	-.0559
.1441	.7642	-.1742	.1355	.7919	-.0615
.1515	.7970	-.1733	.1518	.8020	-.0642
.1670	.8318	-.2010	.1638	.8171	-.0694
.1789	.8686	-.2079	.1819	.8308	-.0741
.2083	.9435	-.2257	.2091	.8537	-.0830
.2083	.9397	-.2114	.2091	.8535	-.0829
.2377	.9703	-.2125	.2094	.8555	-.0825
.2625	.9862	-.097	.2391	.8722	-.0915
.2879	.9960	-.2026	.2640	.8910	-.0591
.3172	.9976	-.1983	.2927	.9086	-.1075
.3429	.9995	-.1976	.3201	.9260	-.1173
.4000	.9967	-.1885	.3470	.9392	-.1241
.4000	.9962	-.1916	.3997	.9641	-.1354
.4005	.9957	-.1884	.3997	.9633	-.1364
.4550	.9939	-.1881	.4003	.9620	-.1343
.5063	.9955	-.1869	.4512	.9809	-.1440
.5617	.9953	-.1852	.5076	.9935	-.1493
.6176	.9956	-.1825	.5637	.9989	-.1492
.6375	.9948	-.1811	.6199	1.0009	-.1495
.7245	.9943	-.1812	.6722	1.0024	-.1491
.7784	.9936	-.1785	.7285	1.0014	-.1474
.8354	.9949	-.1784	.7844	1.0005	-.1476
.8902	.9960	-.1767	.8374	1.0009	-.1479
.9461	.9971	-.1764	.8912	1.0004	-.1480
1.0006	.9986	-.1753	.9485	.9994	-.1475
1.0000	1.000	-.1753	1.000	1.0001	-.1477
			1.000	1.0000	-.1467

TABLE 2 PRESSURE DISTRIBUTIONS

UPPER SURFACE 2Y/B= 0.1 X/C CP		UPPER SURFACE 2Y/B= 0.3 X/C CP		UPPER SURFACE 2Y/B= 0.5 X/C CP		UPPER SURFACE 2Y/B= .70 X/C CP		UPPER SURFACE 2Y/B= .90 X/C CP	
0.	.483	0.	.408	0.	.319	0.	.276	0.	.292
.01	-.216	.01	-.421	.003	-.068	.01	-.545	.01	-.458
.02	-.508	.02	-.769	.006	-.278	.02	-.816	.02	-.678
.03	-.606	.03	-.955	.01	-.519	.03	-.950	.03	-.764
.04	-.591	.04	-1.012	.02	-.839	.04	-.976	.04	-.748
.05	-.590	.05	-1.059	.03	-1.000	.05	-1.124	.05	-.900
.06	-.571	.06	-1.034	.04	-1.053	.06	-1.113	.06	-.909
.08	-.549	.08	-1.029	.05	-1.135	.08	-1.095	.08	-.891
.1	-.519	.1	-.866	.06	-1.149	.1	-1.108	.1	-.912
.125	-.499	.125	-.787	.08	-1.137	.125	-1.120	.125	-.924
.15	-.486	.15	-.764	.1	-1.160	.15	-1.149	.15	-.936
.175	-.475	.175	-.707	.125	-1.156	.175	-1.136	.175	-.948
.2	-.472	.2	-.664	.15	-1.154	.2	-1.135	.2	-.974
.225	-.453	.225	-.622	.175	-1.117	.225	-1.136	.225	-.998
.25	-.438	.25	-.590	.2	-.849	.25	-1.117	.25	-1.007
.3	-.449	.3	-.559	.225	-.749	.3	-.888	.3	-1.071
.35	-.441	.35	-.534	.25	-.702	.35	-.718	.35	-1.147
.4	-.438	.4	-.525	.3	-.663	.4	-.721	.4	-.927
.45	-.430	.45	-.506	.35	-.642	.45	-.777	.45	-.677
.5	-.417	.5	-.493	.4	-.642	.5	-.643	.5	-.637
.55	-.396	.55	-.450	.45	-.630	.55	-.450	.55	-.592
.6	-.350	.6	-.413	.5	-.603	.6	-.351	.6	-.505
.65	-.312	.65	-.334	.55	-.557	.65	-.269	.65	-.437
.7	-.287	.7	-.268	.6	-.406	.7	-.223	.7	-.343
.75	-.245	.75	-.231	.65	-.313	.75	-.183	.75	-.242
.8	-.192	.8	-.185	.7	-.258	.8	-.140	.8	-.168
.85	-.143	.85	-.136	.75	-.197	.85	-.091	.85	-.142
.9	-.086	.9	-.071	.8	-.161	.9	-.028	.9	-.113
.95	-.017	.95	-.011	.85	-.106	.95	.023	.95	-.064
1.	.028	1.	.041	.9	-.047	1.	.060	1.	-.030
				.95	.017				
				1.	.059				
LOWER SURFACE 2Y/B= 0.1 X/C CP		LOWER SURFACE 2Y/B= 0.3 X/C CP		LOWER SURFACE 2Y/B= 0.5 X/C CP		LOWER SURFACE 2Y/B= .70 X/C CP		LOWER SURFACE 2Y/B= .90 X/C CP	
0.	.547	0.	.547	0.	.547	0.	.547	0.	.547
.05	.240	.05	.205	.01	.381	.05	.189	.05	.090
.1	.171	.1	.129	.02	.306	.1	.093	.1	.005
.15	.136	.15	.081	.03	.258	.15	.036	.15	-.039
.2	.098	.2	.049	.04	.233	.2	.025	.2	-.063
.3	.060	.3	.017	.05	.201	.3	-.011	.3	-.119
.4	.031	.4	-.009	.1	.106	.4	-.028	.4	-.114
.5	.008	.5	-.025	.15	.078	.5	-.016	.5	-.095
.6	.039	.6	.038	.2	.060	.6	.055	.6	-.013
.7	.126	.7	.145	.3	.024	.7	.155	.7	.098
.75	.167	.75	.180	.4	-.011	.75	.185	.75	.138
.8	.180	.8	.189	.5	-.010	.8	.201	.8	.154
.85	.177	.85	.186	.6	.048	.85	.172	.85	.161
.9	.140	.9	.149	.65	.104	.9	.132	.9	.144
.95	.093	.95	.104	.7	.149	.95	.060	.95	.099
1.	.028	1.	.041	.75	.191	1.		1.	-.030
				.8	.202				
				.85	.201				
				.9	.176				
				.95	.123				
				1.	.059				

5.2 Thin-layer Navier-Stokes solution

Argyris G. Panarast, Joseph L. Steger†

†NRC Senior Research Associate*

‡Senior Staff Scientist, Fluid Dynamics Division

NASA Ames Research Center, Moffett Field, California 94035, U. S. A.

1. Introduction

The prolate spheroid is a body of simple geometry that can provide significant understanding of the complex flow that can develop about slender bodies at incidence. A variety of wind tunnel tests have been carried out for a 6:1 prolate spheroid at the DFVLR, at Göttingen, using a glass-fiber model of 4mm wall thickness and having major and minor axis of 2.4m and 0.4m, respectively. The majority of the tests have been carried out at moderate Reynolds numbers but some measurements have also been conducted in collaboration with ONERA, in France, at higher Reynolds numbers.

For the purposes of the Working Group No 10 of the Fluid Dynamics Panel of AGARD, the flow field surrounding a 6:1 prolate spheroid was calculated at the NASA Ames Research Center. Two sets of flow conditions were studied, $\alpha = 30^\circ$, $U_\infty = 75\text{m/s}$, $Re_l = 43 \times 10^6$, corresponding to conditions tested at ONERA, and the transitional flow case of $\alpha = 10^\circ$, $U_\infty = 55\text{m/s}$ and $Re_l = 7.7 \times 10^6$, which the members of the Working Group have used for the boundary-layer calculations. For the calculation of the flow field the code F3D described in Ref. 1 has been used. The code solves a conservative form of the thin-layer Navier-Stokes equations cast in generalized coordinates, so that it can be readily used for computing flows about complex configurations.

Here the results of these calculations and comparisons with the available experimental data are given. The calculated flow fields are similar to the ones obtained experimentally, characterized by the appearance of a pair of symmetrical vortices at the leeward of the body, that originates along the lines of cross-flow separation. Similar computational results for these cases were also recently published by Vatsa et al. (Ref. 2).

2. Numerical method

The conservation equations of mass, momentum, and energy can be represented in a flux-vector form that is convenient for numerical simulation as:

$$\partial_\tau \hat{Q} + \partial_\xi (\hat{F} + \hat{F}_v) + \partial_\eta (\hat{G} + \hat{G}_v) + \partial_\zeta (\hat{H} + \hat{H}_v) = 0 \quad (1)$$

where τ is the time, and the independent spatial variables ξ, η , and ζ are chosen to map a curvilinear body-conforming discretization into a uniform computational space. In the system used in this study, ξ denotes the curvilinear axis in the direction of the main body axis, η denotes the circumferential and ζ the normal to the body direction. As opposed to the inviscid flux terms \hat{F}, \hat{G} , and \hat{H} , the terms \hat{F}_v, \hat{G}_v , and \hat{H}_v are fluxes containing the viscous derivatives. A nondimensional form of the equations is used throughout this work. Lengths are scaled by the length of the body, L , velocity components by the free-stream velocity of sound, a_∞ , the pressure and the total energy per unit volume, (e) , by $\rho_\infty a_\infty^2$. The other quantities, such as T, ρ, μ are scaled by their free-stream values.

For body-conforming coordinates and high-Reynolds number flow the thin-layer approximation can be applied (Ref. 3,4)

$$\partial_\tau \hat{Q} + \partial_\xi \hat{F} + \partial_\eta \hat{G} + \partial_\zeta \hat{H} = Re^{-1} \partial_\zeta \hat{S} \quad (2)$$

where only viscous terms in the normal to the body direction are retained. These have been collected into the vector \hat{S} and the nondimensional Reynolds number Re is factored from the viscous flux term. In the present turbulent computations, the coefficients of viscosity appearing in the right-hand-side terms of Eq. (2) are obtained from the model of Baldwin and Lomax (Ref. 3).

In differencing these equations it is advantageous to difference about a known base solution. If the base state is properly chosen, the differenced quantities can have smaller and smoother variation and therefore less differencing error. If the free-stream is used as the base solution:

$$\begin{aligned} \delta_\tau (\hat{Q} - \hat{Q}_\infty) + \delta_\xi (\hat{F} - \hat{F}_\infty) + \delta_\eta (\hat{G} - \hat{G}_\infty) \\ + \delta_\zeta (\hat{H} - \hat{H}_\infty) - Re^{-1} \delta_\zeta (\hat{S} - \hat{S}_\infty) = 0 \end{aligned} \quad (3)$$

where δ indicates a general difference operator.

An implicit approximately-factored scheme for the thin-layer, Navier-Stokes equations that uses central differencing

* Presently, Agias Elenis 63, Athens 15772, Greece

in the η and ζ directions and upwind differencing in the ξ direction can be written in the form:

$$\begin{aligned} & [I + h\delta_\xi^b(\hat{A}^+)^n + h\delta_\zeta \hat{C}^n - hRe^{-1}\delta_\zeta J^{-1}\hat{M}^n J - D_i|_\zeta] \\ & \times [I + h\delta_\xi^f(\hat{A}^-)^n + h\delta_\eta \hat{B}^n - D_i|_\eta] \Delta \hat{Q}^n = \\ & - \Delta t \{ \delta_\xi^b [(\hat{F}^+)^n - \hat{F}_\infty^+] + \delta_\xi^f [(\hat{F}^-)^n - \hat{F}_\infty^-] \\ & + \delta_\eta (\hat{G}^n - \hat{G}_\infty) + \delta_\zeta (\hat{H}^n - \hat{H}_\infty) - Re^{-1} \delta_\zeta (\hat{S}^n - \hat{S}_\infty) \} \\ & - D_e(\hat{Q}^n - \hat{Q}_\infty) \end{aligned} \quad (4)$$

where $h = \Delta t$ or $\Delta t/2$ for first or second order time accuracy, and the free stream base solution is used. Here δ is typically a three-point, second-order-accurate, central difference operator, $\bar{\delta}$ is a midpoint operator used with the viscous terms, and the operators δ_ξ^b and δ_ξ^f are backward and forward three-point difference operators. The flux \hat{F} has been split into \hat{F}^+ and \hat{F}^- , according to its eigenvalues (Ref. 5), and the matrices \hat{A}^\pm , \hat{B} , \hat{C} , and \hat{M} result from local linearization of the fluxes about the previous time level. In Eq. (4), J denotes the Jacobian of the coordinate transformation. Dissipation operators, D_e and D_i , are used in the central space differencing directions (Ref. 1).

The factored left-hand-side operators can be readily solved by sweeping in the ξ direction and inverting tridiagonal matrices with 5×5 blocks. This two-factor implicit scheme is readily vectorized in planes of $\xi = \text{constant}$.

The grid was generated by solving a system of hyperbolic differential equations (Steger and Chaussee, Ref. 6). First, a two-dimensional grid was generated in the symmetry plane. Then the three-dimensional grid was obtained by rotating it about the major axis of the ellipse. The grid consists of 121 points along the direction of the main axis of the body, 100 around its circular section (no plane of symmetry) and 65 radially from the surface. For the various graphics, the output file was reduced. The reduced grid is shown in figure 1. Each grid point (J, K, L) is defined by the Cartesian coordinates x, y, z . The axial coordinate, x , is measured from the nose of the ellipsoid, the lateral coordinate, y , from the vertical-longitudinal symmetry plane and the normal coordinate, z , from the horizontal-longitudinal symmetry plane.

3. Calculated quantities

For the calculation of the skin friction the physical contravariant velocity components U^*, V^*, W^* , were used. The physical contravariant velocity components are related to the cartesian velocity components through the following equations:

$$\begin{aligned} U^* &= (u\xi_x + v\xi_y + w\xi_z) \sqrt{x_\xi^2 + y_\xi^2 + z_\xi^2} \\ V^* &= (u\eta_x + v\eta_y + w\eta_z) \sqrt{x_\eta^2 + y_\eta^2 + z_\eta^2} \\ W^* &= (u\zeta_x + v\zeta_y + w\zeta_z) \sqrt{x_\zeta^2 + y_\zeta^2 + z_\zeta^2} \end{aligned} \quad (5)$$

The vectors (ξ_x, ξ_y, ξ_z) etc., are the components of the contravariant base vectors, while the vectors (x_ξ, y_ξ, z_ξ) etc., are the components of the covariant metrics. Equations (5) are valid for a curvilinear non-orthogonal system.

The components of the local skin-friction coefficient, along the streamwise and along the crosswise directions, were estimated by the equations:

$$\begin{aligned} c_{f\xi} &= \frac{1}{q_\infty} \left(\mu \frac{\partial U^*}{\partial \xi} \right)_w \\ c_{f\eta} &= \frac{1}{q_\infty} \left(\mu \frac{\partial V^*}{\partial \eta} \right)_w \end{aligned}$$

As the skin friction is estimated near the wall, only the dynamic viscosity μ was considered. Its value was estimated by Sutherland's formula. The velocity differences and the associated normal distance were estimated between the wall ($L = 1$) and the first layer of grid points ($L = 2$).

4. Results

Morphology of the flow surrounding inclined bodies

It is known that the flow field surrounding bodies at incidence is characterized by the appearance of a leeward-side vortex structure. The morphology of the vortical structure is similar for a variety of shapes of bodies. This topic has been covered in detail by Tobak and Peake (Ref. 7) and by Perry, Chong and Hornung (Ref. 8). In a cross-section of such a flow, under the action of circumferential pressure gradient, the outer flow approaching the windward plane of symmetry turns and flows outwards along the body, from the windward toward the leeward side. The boundary layer which is formed in this way, separates from the body at a point on the leeward side that depends on the streamwise position of the cross-section and on the flow conditions. Then the fluid leaves the body along a feeding sheet and rolls up to form a primary vortex system on the leeward side of the body. The pair of the primary vortices induces a flow toward the body surface, which at the point of attachment turns outwards toward the windward side. For primary vortices of sufficient

strength, a secondary separation is induced to the boundary layer below them. Thus the secondary vortex structure may appear, that rotates in an opposite direction than the primary one. Both the systems are carried downstream by the axial component of the flow.

Experimentally, the vortex structures may be detected by particle trace techniques (e.g. smoke), reconstruction of velocity measurements, or more simply, by using surface oil-flow techniques. The lines that are formed on a surface by the oil correspond to the surface skin-friction lines. These lines converge toward the primary and the secondary separation lines and diverge from the attachment line, that lies between them. Computationally, the equivalent of the surface shear-stress lines visualized in oil-flow experiments is simulated by releasing particles at selected grid points on the first layer of points above the body. The particles move with the local fluid velocity, but are constrained to the plane just above the body, i.e., the normal velocity component is set to zero in the time integration.

Comparison of the results with experiments, $\alpha = 30^\circ$

The measurements at ONERA included surface-pressure and skin friction distribution, together with oil-flow visualization. The more detailed tests performed at Göttingen at a Reynolds number equal to 8.52×10^6 also include measurements of the velocity components in the flow field (Ref. 9). The experimental results indicated that in both cases the flow developed similarly to the typical case described in the previous section. At this time the ONERA experimental data have not been published. However, Meier (private communication) has provided the distribution of the pressure coefficient and some other information.

Flow-field results of the calculations are shown in figures 2, 3. The existence of the vortex structure and its outer extent at midlength of the body is indicated by the velocity-vectors plot (figure 2). The primary and secondary vortex structures are detected in figure 3, where surface particle traces are used to simulate the surface shear-stress lines visualized in oil-flow experiments. In this figure the experimental oil-flow pictures included in Ref. 10 are also shown, in top and side view. It is observed that the computed particle traces show relatively good agreement with the experiments. The extent of the crossflow separation, indicated by the primary separation line, is very similar in both cases, with the exception of a small region near the sting. There the separation is more extensive for the calculated results (inadvertent use of a thinner sting in the computations may account for some of this discrepancy). Also, the coincidence of the secondary crossflow separation lines is remarkable. In both cases they run along the azimuthal line of 30° from the leeward symmetry plane.

Computed surface-pressure coefficients at windward ($\phi = 0^\circ$) and leeward ($\phi = 180^\circ$) planes of symmetry are compared with the experimental data in figure 4. The agreement with the experimental results on the windward side, is good. This was expected, because the windward boundary layer remains attached almost over the entire length (near the sting there are again some differences). The computed and experimental pressure distributions are also in good agreement on the leeward plane of symmetry. A small difference is observed between $x/L = 0.2 - 0.4$. It is noted that while in the experiments the flow was transitional at part of the nose, in the calculations it has been assumed that the flow starts as a turbulent one.

In order to verify the quality of the numerical solution away from the symmetry planes, the computed and the experimental pressure coefficients are compared along the circumferential direction, ϕ , in figure 5, at three axial locations. The agreement is good, not only on the windward but also on the leeward side. The suction observed at $\phi = 160^\circ$, on the two upper curves, is due to the secondary vortex.

The computed shear stress angle, γ , along the wall, is shown in figure 6, at the same axial locations that were used in the case of the pressure coefficient. The experimental data have not been released as yet, so a comparison is not possible. However the good agreement of the oil-flow simulation with the experiments indicates that the predicted γ angles may be not very different from the experimentally found values.

Effect of turbulence model and of grid refinement

Both the turbulence modeling and grid resolution can affect the output of the calculations and must be assessed. In the present paper, the calculations were started with a grid consisting of $93 \times 72 \times 47$ points and then they continued with a grid of $121 \times 100 \times 65$ points.

In the case of the turbulent modeling, the turbulent viscosity coefficient μ_t was computed using the two-layer, Cebeci-type, algebraic eddy-viscosity model reported by Baldwin and Lomax (Ref. 3). In both layers, μ_t depends on the absolute value of the local vorticity vector, ω , and on the distance from the wall, y . More specifically, in the outer layer the turbulent viscosity coefficient is proportional to the maximum value of the function:

$$F(y) = |\omega|y[1 - e^{-(\frac{y}{\delta^+})^4}] \quad (7)$$

and to the value of y at which this maximum occurs, y_{max} .

Degani and Schiff (Ref. 11) observed that the evaluation of y_{max} is not straightforward in cases of bodies with crossflow separation. Indeed, while in the windward side the attached boundary layer gives rise to a profile of $F(y)$ which has a single maximum, in the leeward side a second maximum, of greater value, appears. This second maximum is due to the overlying vortical structure. Thus, if in the code, the computer searches outward along each ray to determine the peak of $F(y)$, it will select the second maximum. The resulting value of μ will be much higher than the one of the boundary layer. This will cause an underestimation of the extent of the crossflow separation and, consequently, of the size of the vortical structures.

For eliminating the forementioned difficulty, Degani and Schiff modified the turbulence subroutine, in their code, so that the first peak of $F(y)$ is selected at each profile. In the present calculations, initially the flow was estimated without the modification suggested by Degani and Schiff. Then after reviewing the profiles of the function $F(y)$ around the prolate spheroid, a cut-off distance was defined, that divides the boundary layer and the vortical structures. This is evident in figure 7, where profiles of $F(y)$ are shown at some typical points of the body. It is observed in this figure that the maxima of the boundary-layer vorticity distributions lie below the value $L = 22$, in all the stations. Thus, if the outward search stops at this cut-off distance only the first peak will be selected and not the one which is due to the vortical structures. After this principle was applied for the evaluation of the turbulent viscosity coefficient, the profiles of $F(y)$ were plotted again, and checked as to whether the value $L = 22$ was still appropriate. No significant change has been noticed.

The above observation helps, also, in defining the edge of the boundary layer. It is evident, in figure 7, that the vorticity function $F(y)$, after it takes its local maximum value at the boundary layer, it falls rapidly towards a minimum value and then it starts again to rise, at the leeward side, where the vortices are present. At the windward side, where the boundary layer is attached, only one maximum appears and then the $F(y)$ falls to zero. So in general the function $F(y)$ indicates rather clearly the position of the edge of the boundary layer.

Although a systematic study of grid-refinement and variation of the turbulence model was not carried out, computed surface streamline patterns are shown in figure 8, for a coarse grid(8a), a fine one with the standard turbulence model(8b), and a fine one with the improved turbulence model(8c). For a better comparison, an unwrapped coordinate system is used. Note that in this kind of graphics the pictures are distorted, because the vertical abscissa takes the same value at the position of the maximum diameter and at the position of the sting or the nose. A comparison shows that as far as the primary separation line is concerned, the three calculations show essentially the same results. However, things are completely different in the case of the secondary separation line. In the coarse-grid calculation, this line does not appear at all. In the fine-grid calculations with the unmodified turbulence model, an attachment region has been formed between the primary separation line and the symmetry plane. In the final calculations, after the improvement of the turbulence model, the secondary separation line appears very clearly.

Finally, the circumferential variation of the pressure coefficient at the location $x/L = 0.81$ is shown in figure 9 for the three calculations. The experimental data are also included. The gradual improvement of the predicted results is evident in this figure, also.

Comparison of the results with experiments, $\alpha = 10^\circ$

The experiments for the $\alpha = 10^\circ$ case were conducted at the DFVLR. The Reynolds number based on the major axis of the ellipsoid was 7.7×10^5 . The tunnel velocity was 55m/s. Transition was imposed at 20% of the major axis from the nose, by a circumferential strip of carborundum powder. The tests indicated a fully turbulent boundary layer next to the transition strip. Meier (ref. 10) has given the experimentally obtained surface shear-stress and flow inclination data. Velocity profiles at various stations are included in Ref. 12.

For the calculation it was assumed that the flow was laminar up to $x/L = 0.20$. At this point an instantaneous transition to turbulent flow was imposed. Surface particle-traces of the computed solution are shown in figure 10. It is observed that the cross-flow separation is limited, compared to the 30° -case. Also no secondary vortex structure appears, evidently because the strength of the primary vortex is not sufficiently strong to induce it. The experimental oil-flow results are not available. However, the crossflow angle, γ , is known. The calculated crossflow angle and the experimentally found values are shown in figure 11, at various cross-sections. Like the pressure distribution, the crossflow angle, γ , is much easier to accurately predict than the skin friction.

The computed skin-friction coefficient distribution, in the circumferential direction at three axial stations, is compared with the experimental data in figure 12a. The range of the y^+ parameter of the flow, on the first layer of points above the surface of the body was $y^+ = 0.5-0.9$. The agreement of the predicted data with the experimental values is quite good. Shown in figure 12b is a general coordinate boundary layer result (Ref. 13), in which edge conditions were taken from the Navier Stokes result at approximately 30mm above the wall. The boundary layer code uses central differencing without added numerical dissipation in the direction away from the wall, and it is used to verify the Navier-Stokes predicted values of skin friction. Previously obtained Navier-Stokes results using more numerical smoothing and a coarser grid produced different level of C_f , while the boundary layer code was not sensitive to those changes, even though it used the different Navier-Stokes inputs.

Velocity profiles, on the symmetry plane at $x/L = 0.65$ and 0.74 , are compared with the experiments in figure 13a. The agreement on the windward side is better than on the leeward side, where the measured profiles are fuller in their lower part than the predicted ones. For comparison, the computed boundary layer profiles of Ref. 13 are shown in figure 13b.

In first-order-of-magnitude boundary-layer methods the assumption is made that the pressure is constant across a boundary layer. To check this assumption for the particular prolate spheroid flows that are reported in the present paper, the wall pressure in the circumferential direction ($x/L = 0.74$) is compared in figure 14 with the pressure at a normal distance from the wall. This distance is of the order of the maximum thickness of the boundary layer (30mm). It is seen, in figure 14, that the pressure is nearly constant within the boundary layer, in both the 10° and 30° case. A small gradient appears only in the 30° case at the region of maximum acceleration of the cross flow.

5. References

1. Ying, S. X., Steger, J. L., Schiff, L. B., Baganoff, D. "Numerical Simulation of Unsteady, Viscous, High-angle-of-attack Flows using a Partially Flux-split Algorithm". AIAA-86-2179, 1986
2. Vatsa, V. N., Thomas, J. L., Wedan, B. W. "Navier-Stokes Computations of Prolate Spheroids at Angle of Attack". AIAA Paper 87-2627-CP, 1987.
3. Baldwin, B. S. and Lomax, H. "Thin-layer Approximation and Algebraic Model for Separated Turbulent Flows". AIAA-78-257, 1978
4. Pulliam, T. H. and Steger, J. L. "Implicit Finite-Difference Simulations of Three-Dimensional Compressible Flow". AIAA J Vol. 18, No. 2, pp. 159-167, 1980.
5. Steger, J. L. and Warming, R. F. "Flux Vector Splitting of the Inviscid Gasdynamic Equations with Application to Finite Difference Methods". Jour. of Comp. Phys. Vol. 40, No. 2, p.263, 1981.
6. Steger, J. L., Chaussee, D. S. "Generation of Body-fitted Coordinates Using Hyperbolic Partial Differential Equations". SIAM J. Stat. Comput. Vol.1, No 4, pp. 431-437, 1980.
7. Tobak, M., Peake D.J., Annual Rev. Fluid Mechanics, Vol. 14, pap.61, 1982.
8. Perry A. E., Chong M. S., Hornung, H. G. "Local Solutions of the Navier-Stokes Equations in Separated Flows". Paper 8-25, 3rd Symposium on Numerical and Physical Aspects of Aerodynamic Flows, California State University, Jan. 1985.
9. Vollmers, H., Kreplin, H. P., Meier, H. U., Kühn A. "Measured Mean Velocity Field Around a 1:6 Prolate Spheroid at Various Cross Sections". DFVLR, IB 221-85 A 08, 1985.
10. Kreplin, H. P., Vollmers, H., Meier, H. U., "Wall Shear-Stress Measurements on an Inclined Prolate Spheroid in the DFVLR 3m x 3m Low Speed Wind Tunnel, Göttingen". DFVLR, IB 222-84 A 33, 1984.
11. Degani, D., Schiff, L. B. "Computation of Turbulent supersonic Flows around Pointed Bodies having Crossflow Separation". J. of Comp. Physics Vol. 66, No 1, pp.173-196, 1986.
12. Meier, H. U., Kreplin, H. P., Landhäuser, A., Baumgarten, D. "Mean Velocity Distributions in Three-Dimensional Boundary Layers, Developing on a 1:6 Prolate Spheroid with Artificial Transition". DFVLR, IB 222-84 A 11, 1984.
13. Steger, J. L., Van Dalsem, W. R., Panaras, A. G., and Rao, K. V. A Formulation for the Boundary Layer Equations in General Coordinates. NASA TM 100079, June 1988

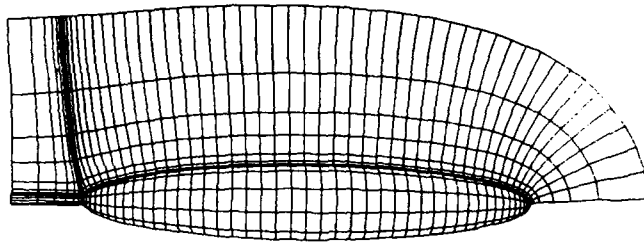


Fig. 1. Schematic view of the grid. Only a few lines are shown.

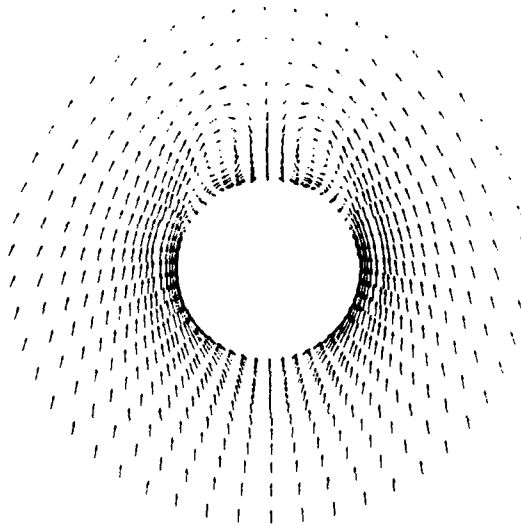


Fig. 2. The calculated flow field. Crossflow velocity vectors at $x/L = 0.50$.
 $Re_l = 43 \times 10^6$, $\alpha = 30^\circ$.

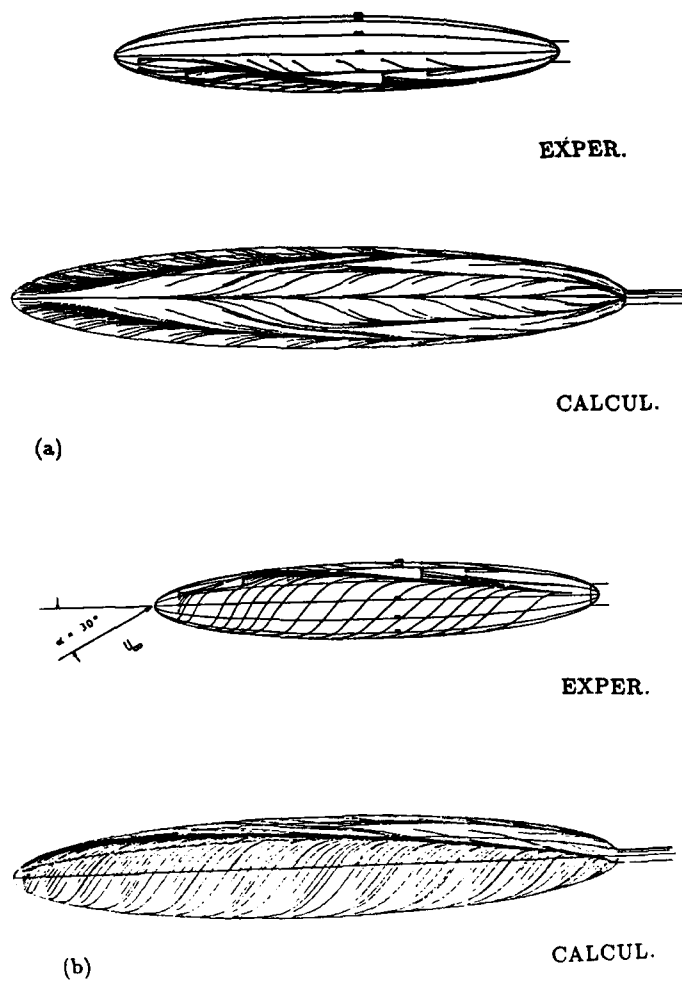


Fig. 3. Comparison of surface particle-traces. (a) top view. (b) side view.

$$Re_l = 43 \times 10^6, \alpha = 30^\circ.$$

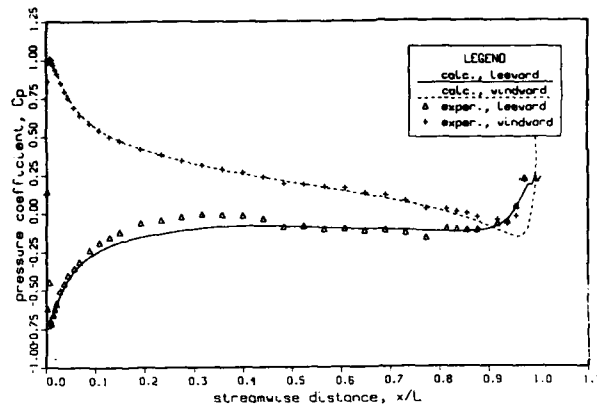


Fig. 4. Comparison of surface pressure at the symmetry planes.
 $Re_1 = 43 \times 10^6$, $\alpha = 30^\circ$.

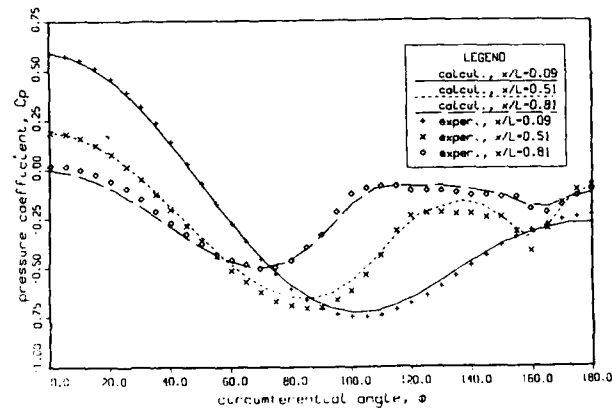


Fig. 5. Comparison of surface pressure at various cross-flow sections.
 $Re_1 = 43 \times 10^6$, $\alpha = 30^\circ$.

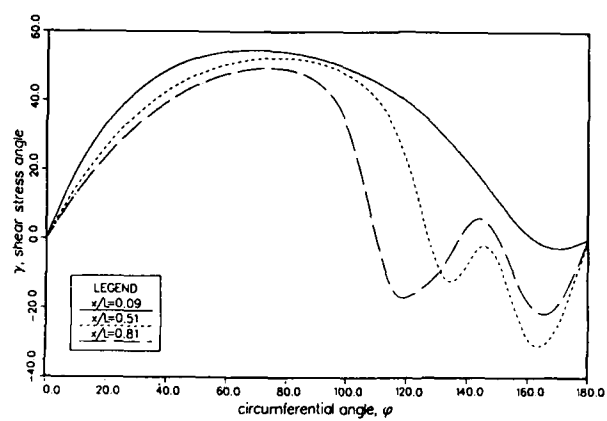
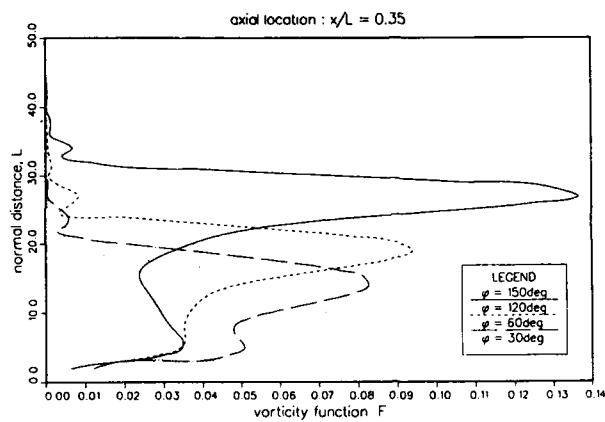
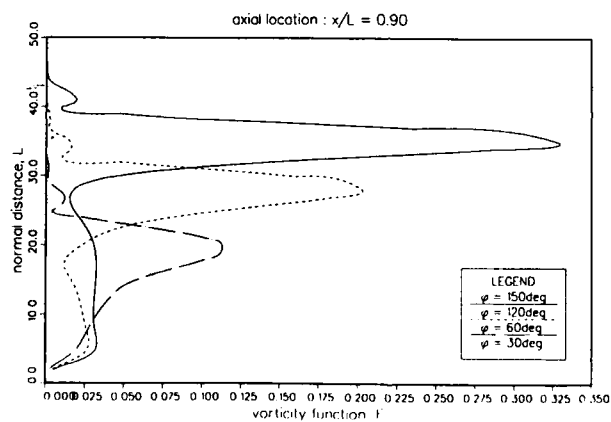


Fig. 6. Variation of shear-stress angle, at various cross-flow sections.
 $Re_l = 43 \times 10^4$, $\alpha = 30^\circ$.



(a)



(b)

Fig. 7. Profiles of the vorticity function, $F(y)$. (a) axial location $x/L = 0.35$. (b) axial location $x/L = 0.90$.
 $Re_l = 43 \times 10^6$, $\alpha = 30^\circ$.

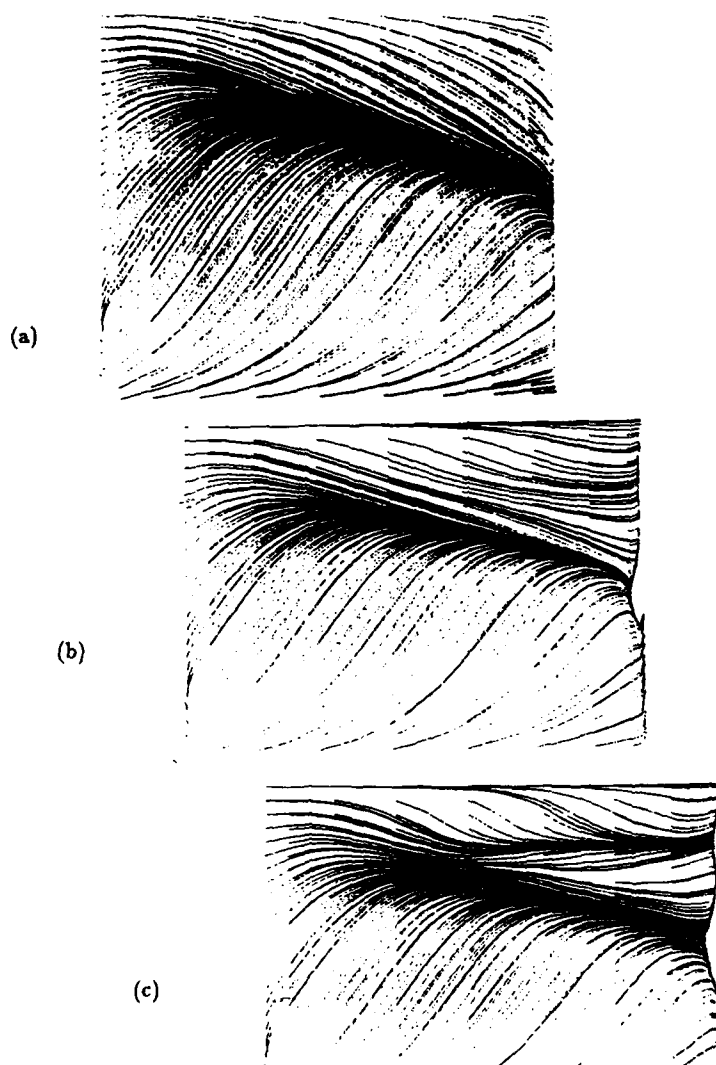


Fig. 8. Surface particle-traces, in an unwrapped coordinate system. (a) coarse grid. (b) fine grid, initial calculations. (c) fine grid, turbulence-model improvement.
 $Re_l = 43 \times 10^6$, $\alpha = 30^\circ$.

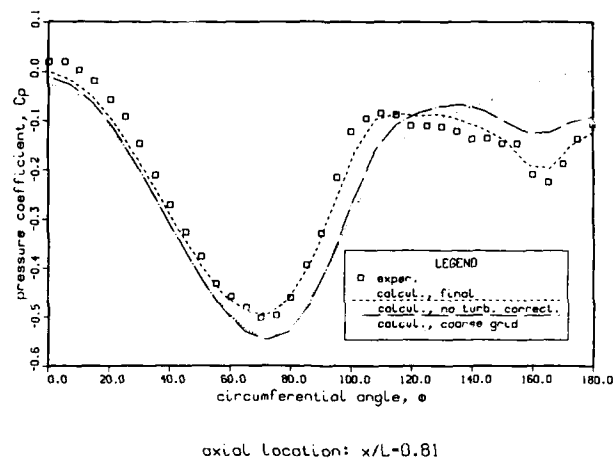


Fig. 9. Comparison of the calculated surface pressure in the circumferential direction at $x/L = 0.81$.
 $Re_1 = 43 \times 10^6$, $\alpha = 30^\circ$.

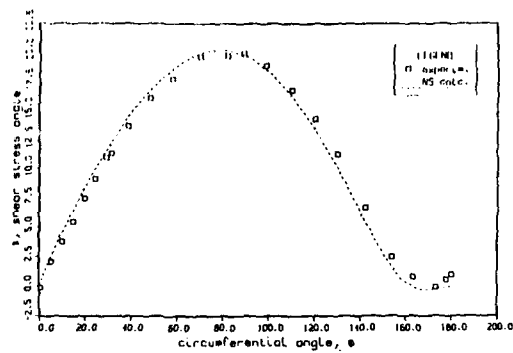


TOP VIEW

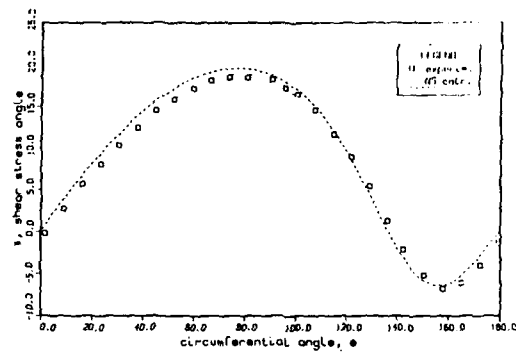


SIDE VIEW

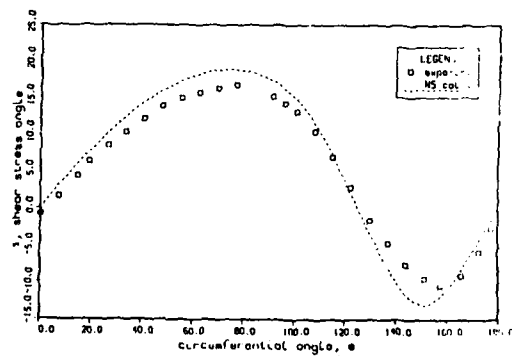
Fig. 10. Surface particle-traces. $Re_l \approx 7.7 \times 10^6$, $\alpha = 10^\circ$.



(a) axial distance, $x/L=0.48$

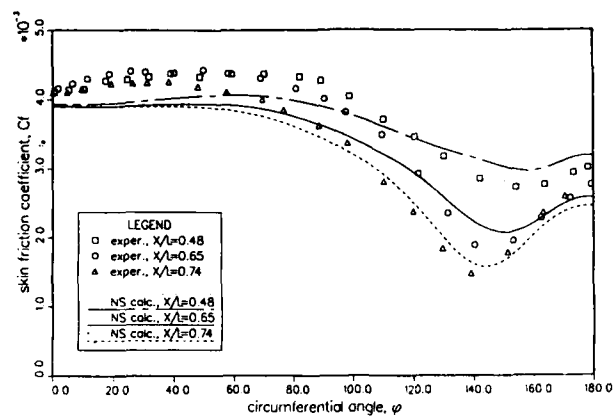


(b) axial distance, $x/L=0.65$

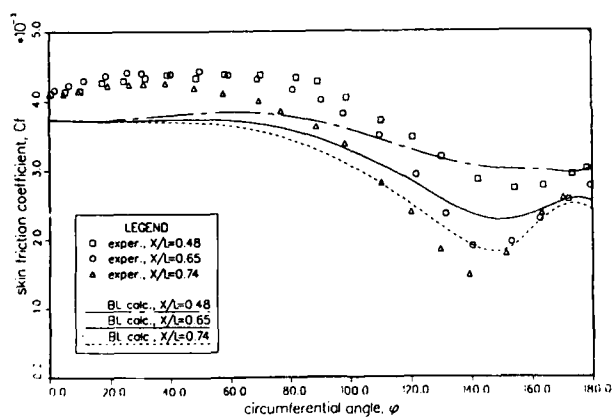


(c) axial distance, $x/L=0.74$

Fig. 11. Shear-stress angle comparison at various cross-sections.
 $Re_1 \approx 7.7 \times 10^6$, $\alpha \approx 10^\circ$.



(a)



(b)

Fig. 12. Skin friction comparison at various cross-sections.
 (a) Navier-Stokes solution. (b) boundary-layer solution.
 $Re_l = 7.7 \times 10^6$, $\alpha = 10^\circ$.

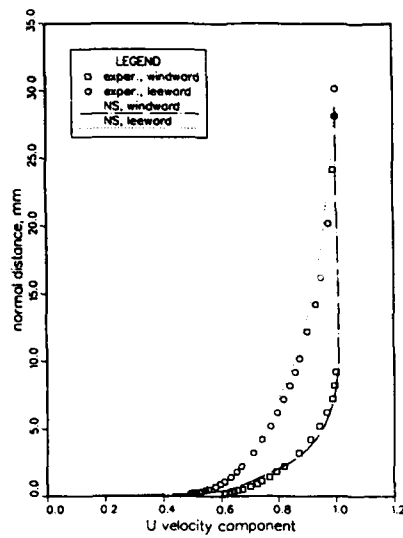
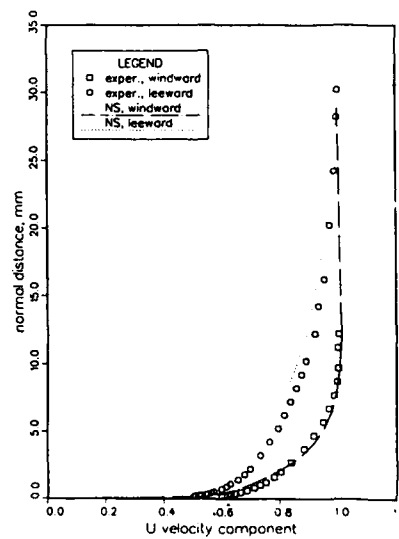
(a) $x/L = 0.65$ (b) $x/L = 0.74$

Fig. 13. Velocity profiles comparison at the symmetry planes. (a) $x/L = 0.65$. (b) $x/L = 0.74$.
 $Re_l = 7.7 \times 10^6$, $\alpha = 10^\circ$.

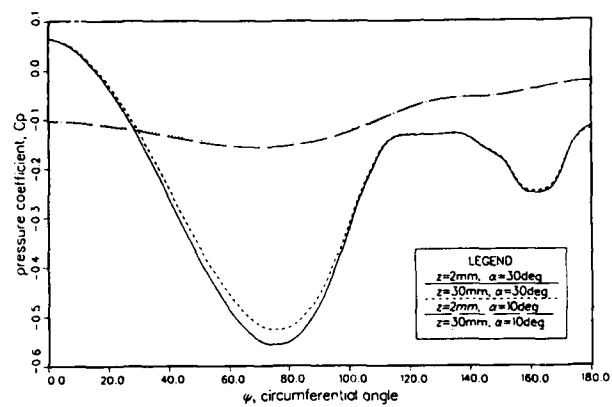


Fig. 14. Variation of the pressure across the boundary layer.

CHAPTER 6. RESULTS

To investigate the accuracy of predicting three-dimensional flows by solving the boundary-layer equations with field and integral methods, two test cases have been considered as a result of the discussions of Chapter 5. The first corresponds to the prolate spheroid discussed in Chapter 5 and examined experimentally in the 3 m x 3 m wind tunnel of the DFVLR in Göttingen. Measurements of wall shear and velocity profiles were obtained at four streamwise stations, $x/2a = 0.48, 0.56, 0.64$ and 0.73 for an angle of attack of $\alpha = 10^\circ$. The measured distributions of the wall pressure coefficient provide a basis for determining the external velocity boundary condition required in the solution of the boundary-layer equations. An alternative approach to this boundary condition is to make use of the measured external velocity values but these are not provided in sufficient detail so that other means require investigation.

The uncertainties associated with the specification of the external velocity distribution have been investigated with results shown in Fig. 1. These results correspond to the velocity components u_e/u_∞ and w_e/u_∞ at $x/2a$ -stations of 0.48 and 0.73 obtained by the solution of the inviscid flow equations with the surface pressure measurements computed by Stock, and from the measurements of Meier and Kreplin. It is clear that the results of the inviscid flow theory are usually higher than those computed from the wall pressure distribution and considerably higher than those measured at the edge of the boundary layer. One possibility for these discrepancies may be the pressure variation across the boundary layer, but this cannot be entirely true since the difference in velocities also appears in areas where the boundary layer is thin and laminar, for example, near the nose. Another possibility may be that the flowfield in the open test section is deflected by the presence of the body because it imposes lift and consequently distorts the pressure distribution. In the light of these uncertainties, the Working Group defined a standard test case, at 10° incidence, which used the external flow data as derived from the wall pressure distribution by Stock.

In general the velocities calculated from the wall pressure distribution by Stock are lower than those calculated from the potential flow but the difference is only a few percent for $\phi < 120^\circ$. For $\phi > 120^\circ$, however, the picture changes; the circumferential velocity component w_e/u_∞ calculated from the surface pressures is higher than that given by inviscid-flow theory and the shape of the resulting distribution is considerably different from that given either by inviscid flow or that obtained by measurements at the boundary-layer edge. The result of these differences is, as shown in more detail below, that if the boundary-layer calculations are performed for the external velocity components deduced from the surface pressures, they are in good agreement with those computed by the inviscid input data so long as ϕ is less than 120° . For $\phi > 120^\circ$ the results differ and, perhaps fortuitously, the inviscid data give closer agreement with experiment.

The second test case corresponds to the Lockheed/NASA Ames C-wing for which there is experimental data obtained in the NASA Ames 6' x 6' transonic/supersonic wind tunnel with a semi-span model for a Mach number range of $M_\infty = 0.25$ to 0.95 (1,2). There are two series of tests, one for the measurement of surface pressures with transition free and the other for boundary-layer measurements with transition fixed at $x/c = 0.045$ on both upper and lower surfaces. The boundary layers were measured only at two chordwise locations corresponding to $x/c = 0.218$ and 0.421 at the mid-semi-span location.

In contrast to the first test case, which has been examined by all of the boundary-layer calculation procedures of Chapter 4 and by the Navier-Stokes method of Chapter 5, the second test case has been calculated only by the Navier-Stokes method described in Chapter 5 and by the interactive boundary-layer method described later in this chapter. As a consequence, the problem of the specification of the external boundary condition described above in connection with the first test case does not arise.

The next two sections are concerned with integral and field methods. In Section 6.1, the emphasis is on the prolate spheroid at $\alpha = 10^\circ$ with some results for the higher angle $\alpha = 30^\circ$. Section 6.2 presents results for the two test cases referred to above and provides a brief description of the interactive procedure.

6.1 Integral methods

P.D. Smith, RAE, Farnborough, Hants, UK

6.1.1 The ellipsoid at 10° incidence

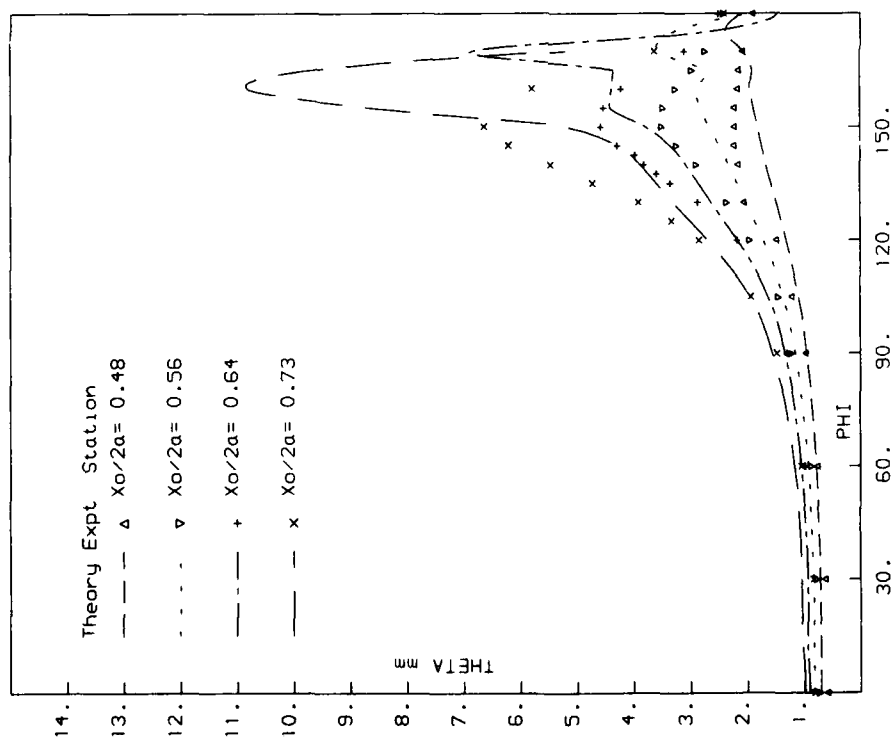
This is the only test case to which the integral methods described in Chapter 4 have been applied. For each method results are shown for the standard test case using the external flow data given by Stock together with some examples of the attempts which have been made to improve the agreement between calculation and experiment.

For the RAE method, Smith has produced results both for the basic method and for the method using Cross's velocity profiles. The use of the more sophisticated velocity profiles produces a small improvement in the results but large differences between calculation and experiment remain on the leeward side ($\phi > 120^\circ$ say) of the body.

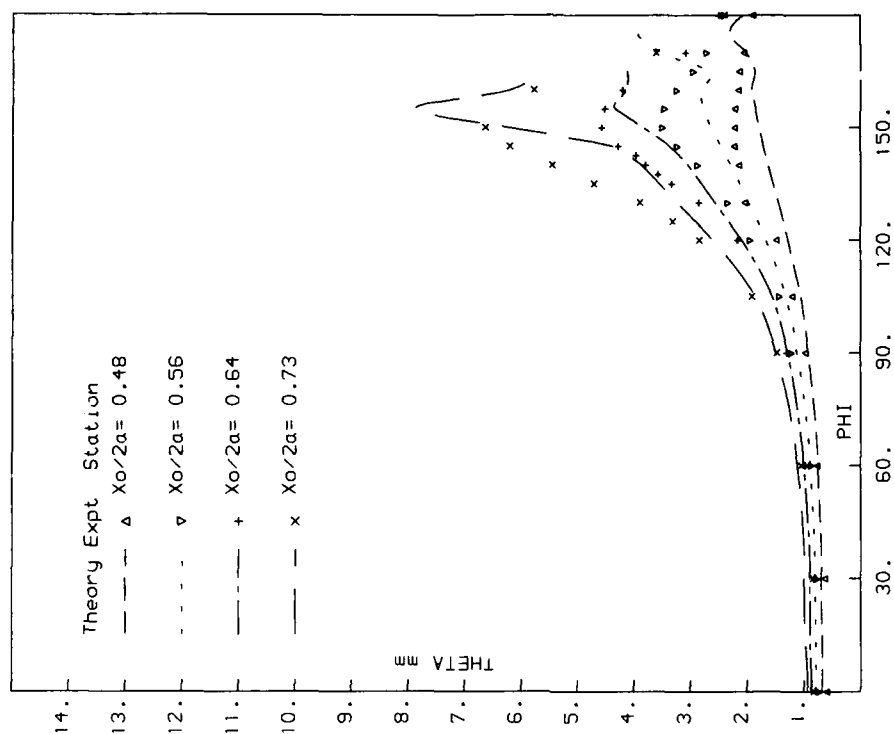
For the ONERA/CERT method, Gleyzes notes that the external flow directions are given by Stock do not agree with the measurements particularly over the rear leeward side of the body. Gleyzes has, therefore, recalculated the external flow by matching it to the experimental data at $x_0/2a = 0.48$. As will be seen from the figures this improves the agreement between experiment and calculation but significant differences remain.

For the ONERA method, Le Balleur and Lazareff have calculated both the standard test case and one in which the external flow is assumed to be the inviscid potential flow which would be present in the absence of all viscous effects. This second calculation improves the agreement with experiment and underlines the unexpected sensitivity of the predictions to the distribution of the external flow angle. This type of calculation has also been made by both Smith and Gleyzes.

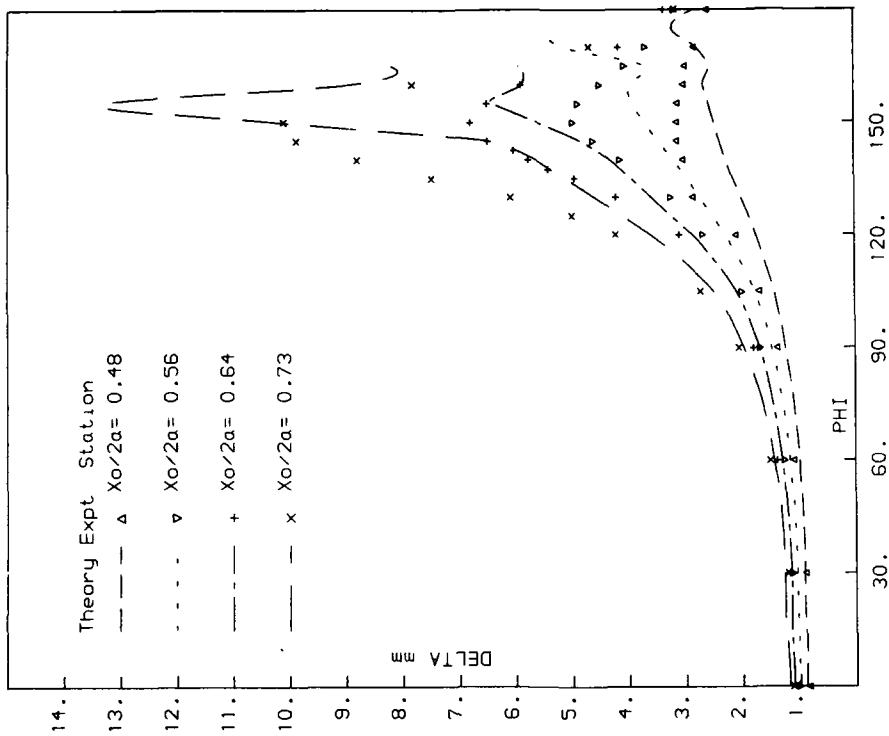
As will be seen from the figures all of the methods produce results of a similar quality and for the standard test case they agree well with experiment over the windward side of the body but on the leeward side they agree more closely with each other than they do with experiment.



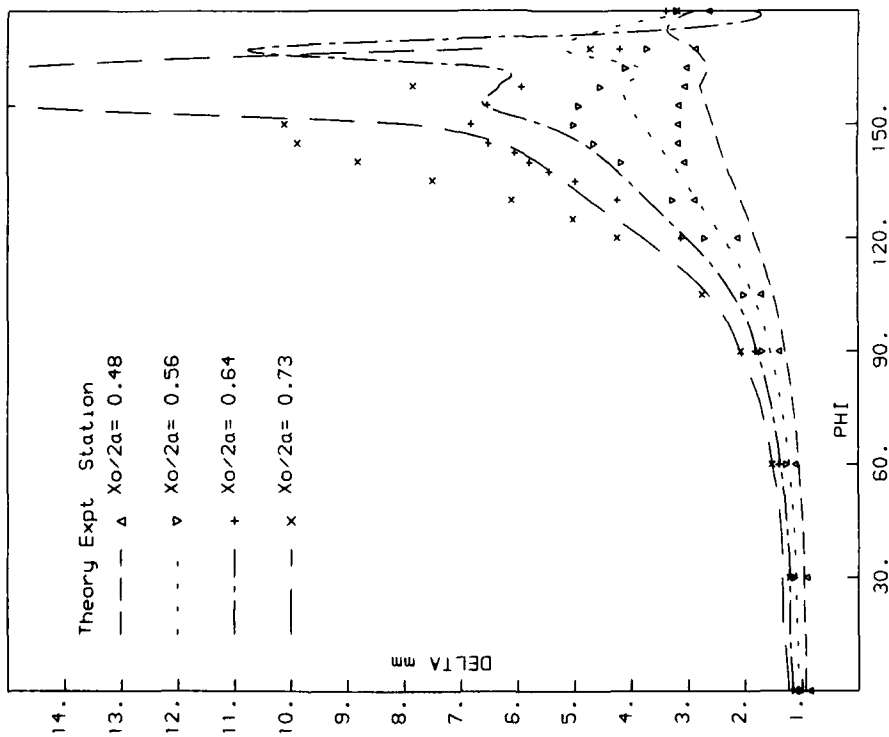
RAE Method



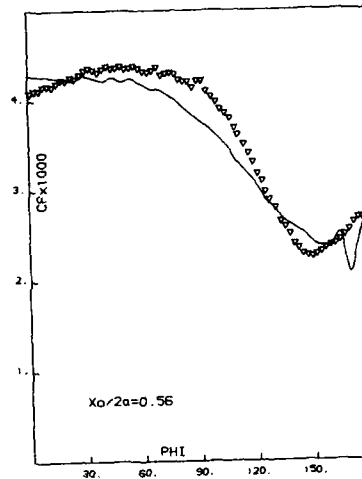
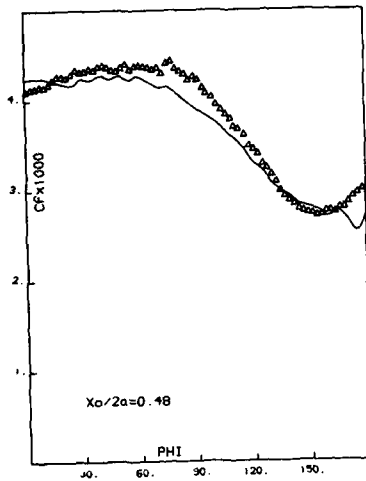
RAE Method Cross's Profiles



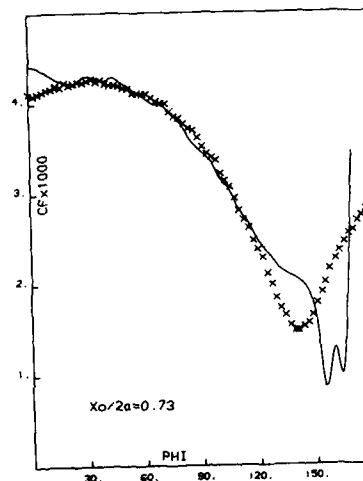
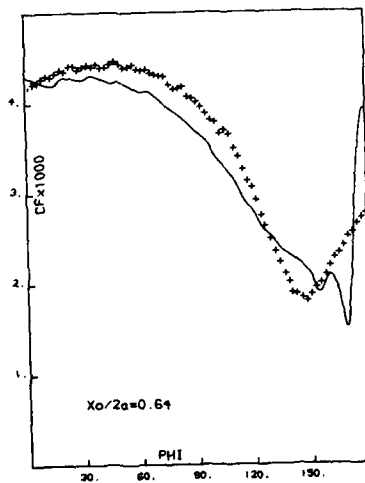
RAE Method Cross's Profiles



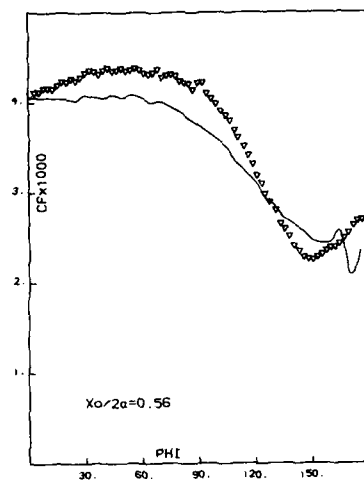
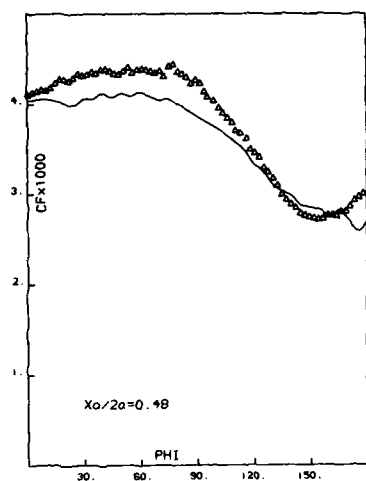
RAE Method



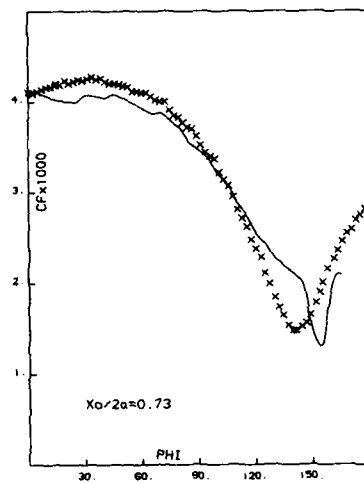
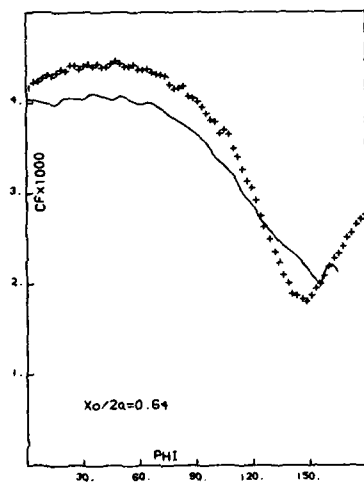
— THEORY
 $\Delta \nabla + \times$ EXPERIMENT



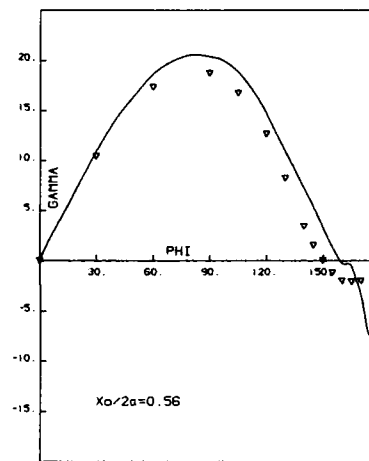
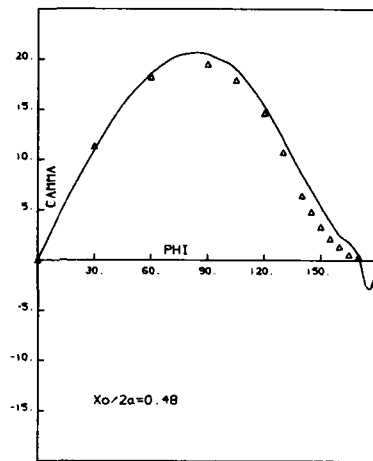
RAE Method



— THEORY
 $\Delta \nabla + \times$ EXPERIMENT

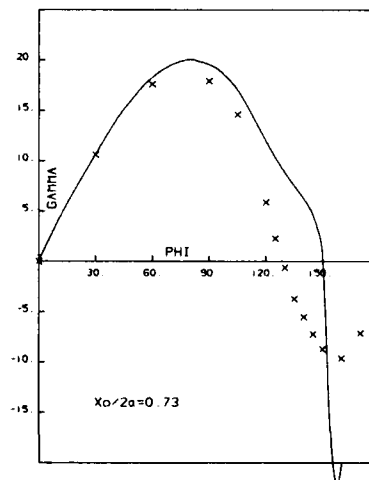
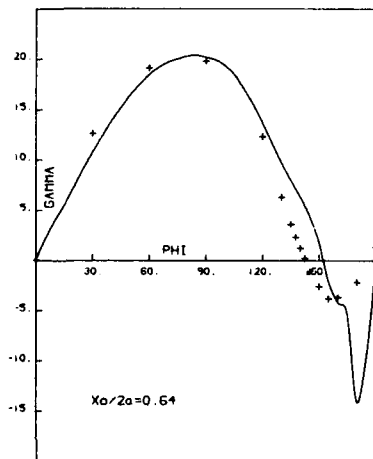


RAE Method Cross's Profiles

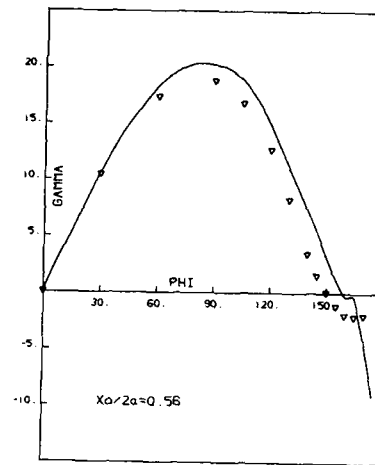
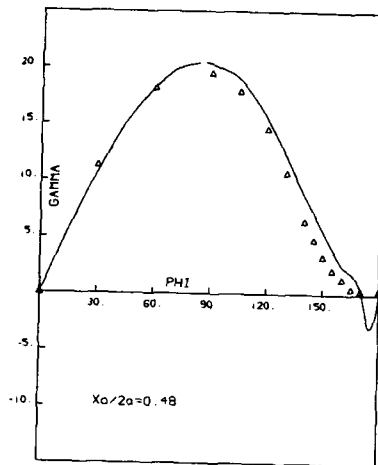


— THEORY

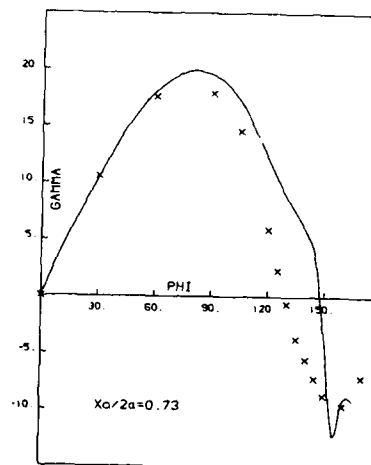
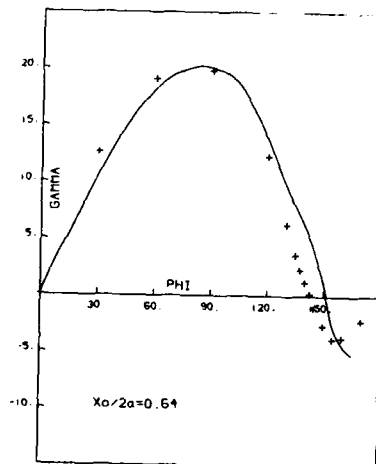
Δ ▽ + × EXPERIMENT



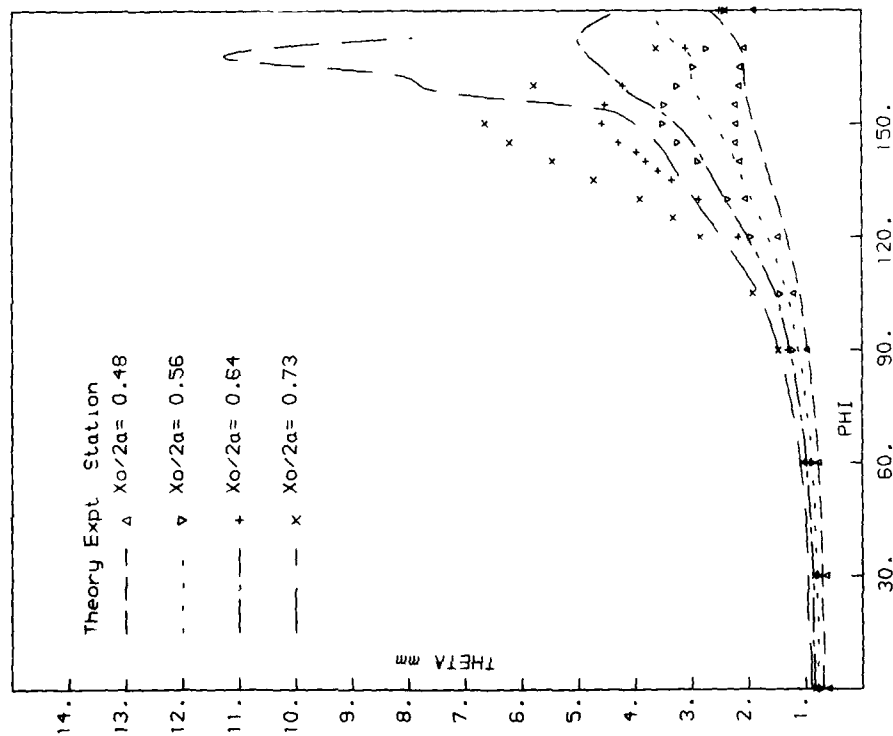
RAE Method



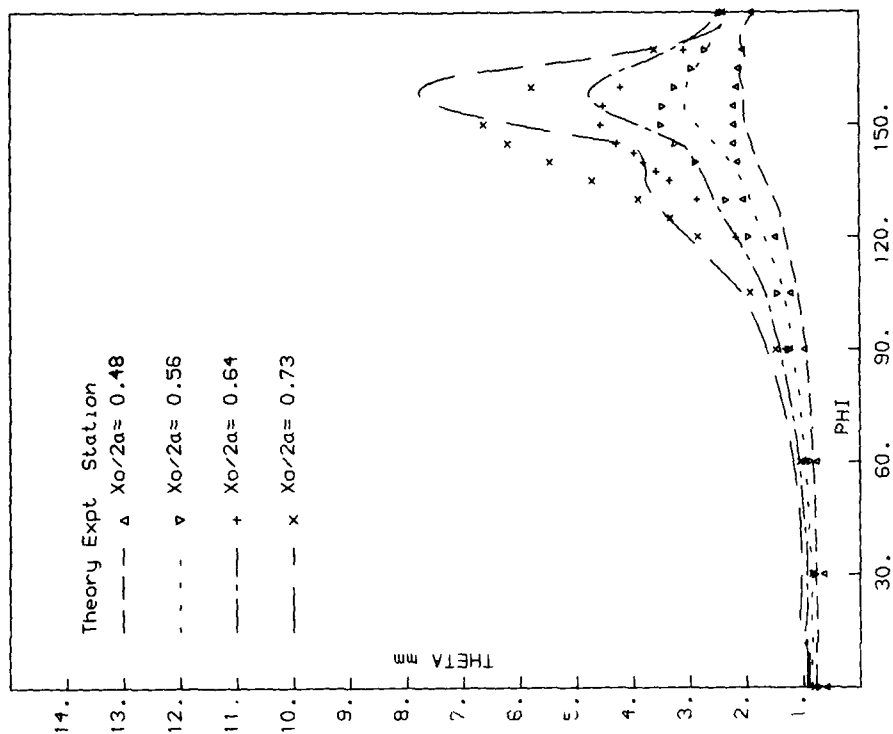
— THEORY
 $\Delta \nabla + \times$ EXPERIMENT



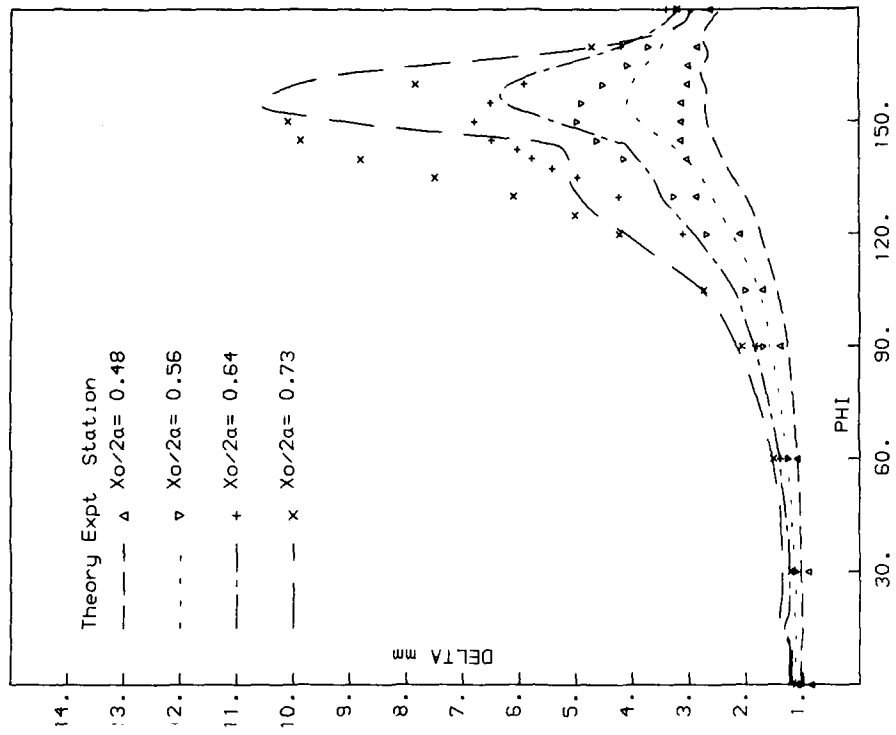
RAE Method Cross's Profiles



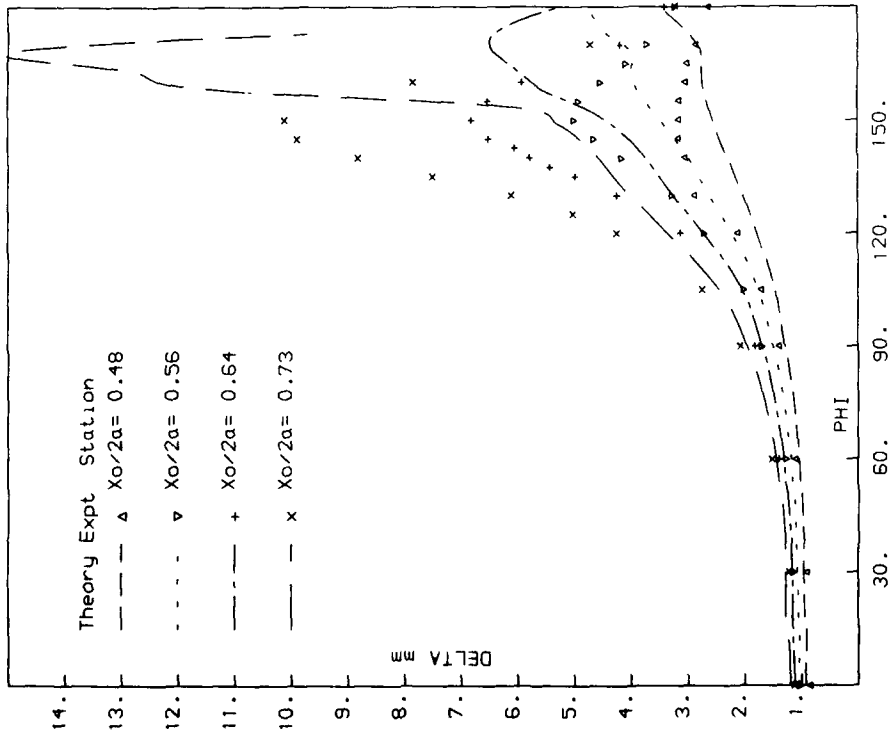
ONERA/CERT Method



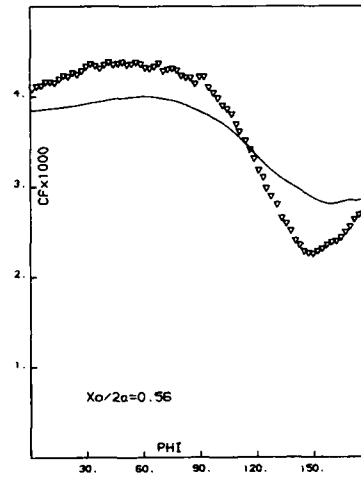
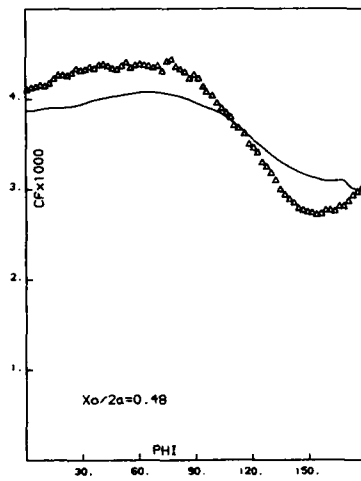
ONERA/CERT Method Recalculated External Flow



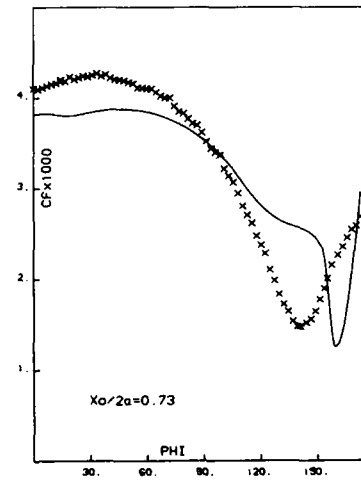
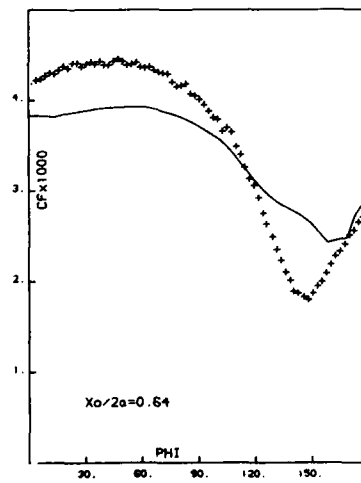
ONERA/CERT Method Recalculated External Flow



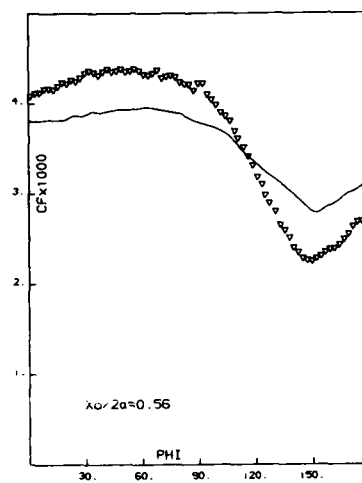
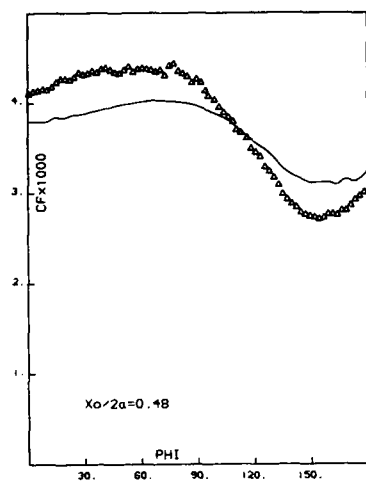
ONERA/CERT Method



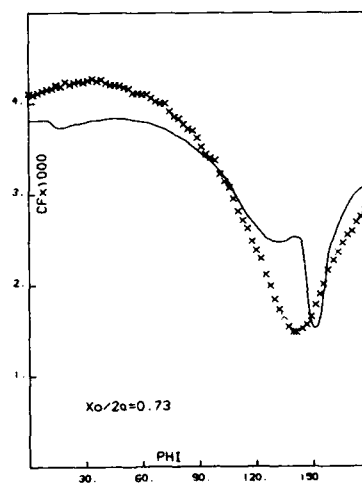
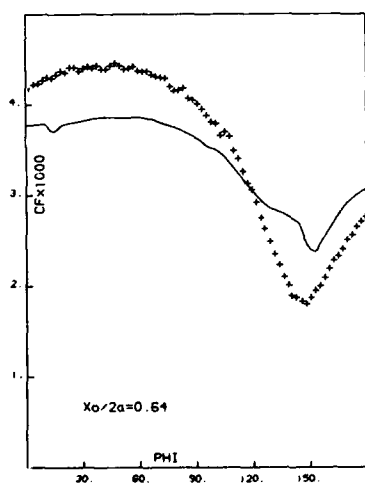
— THEORY
 $\Delta \nabla \times$ EXPERIMENT



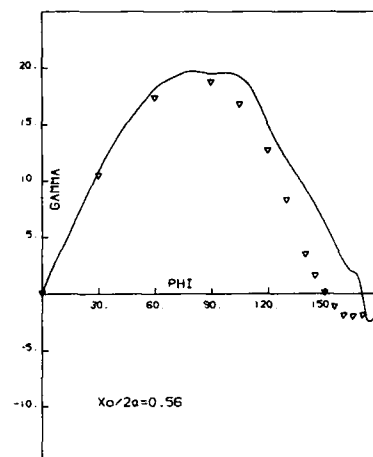
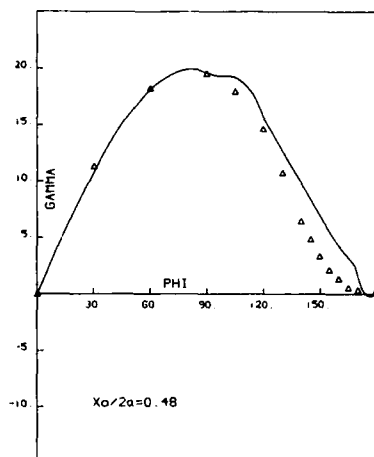
ONERA/CERT Method



— THEORY
 $\Delta \nabla + \times$ EXPERIMENT

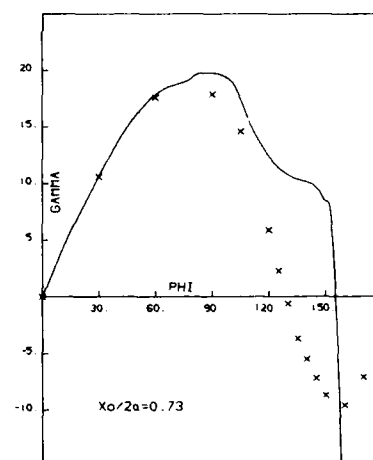
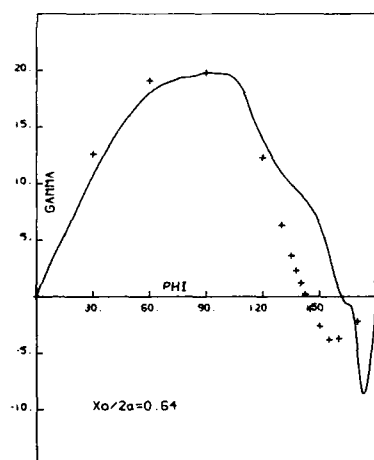


ONERA/CERT Method Recalculated External Flow

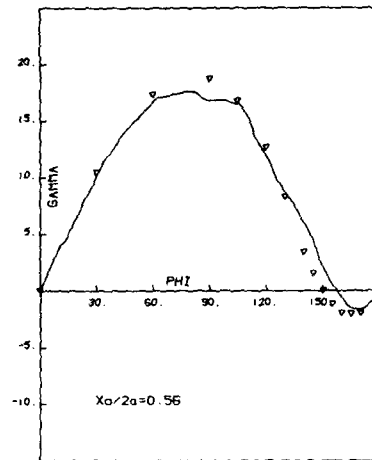
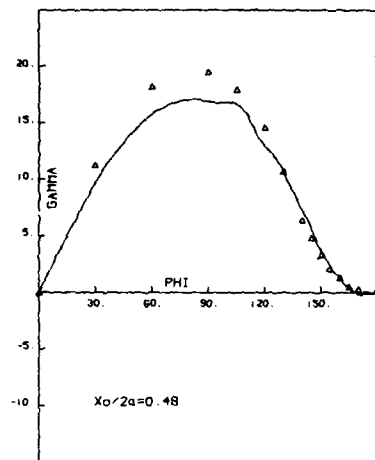


— THEORY

$\Delta \nabla + \times$ EXPERIMENT

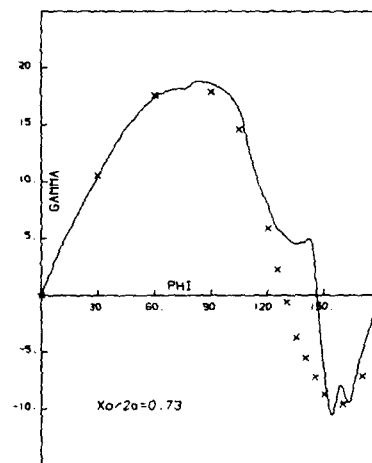
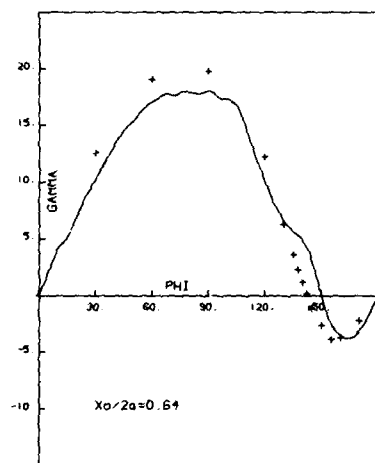


ONERA/CERT Method

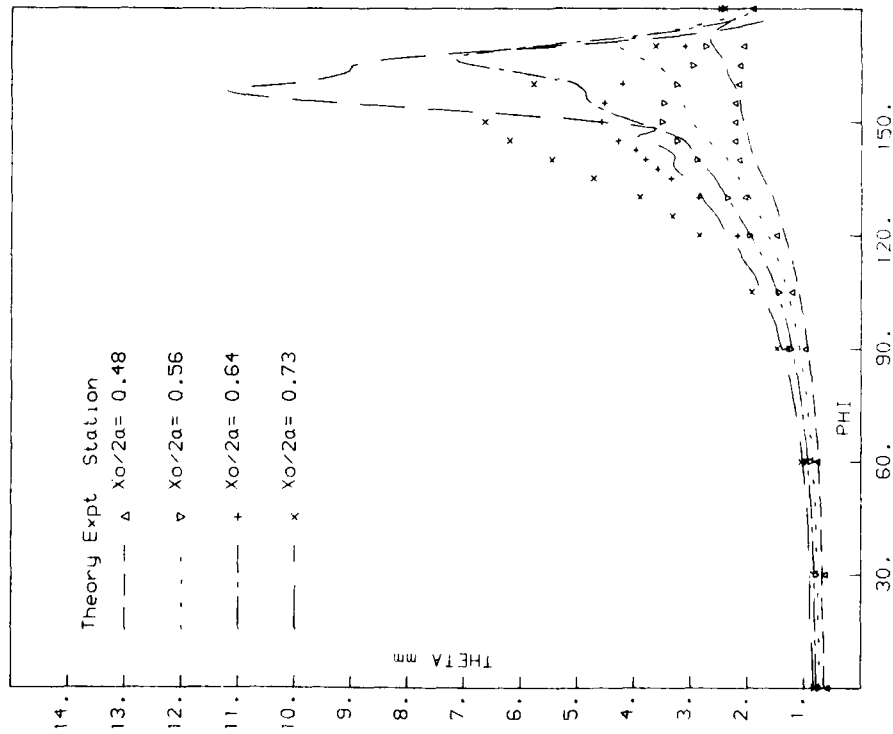


— THEORY

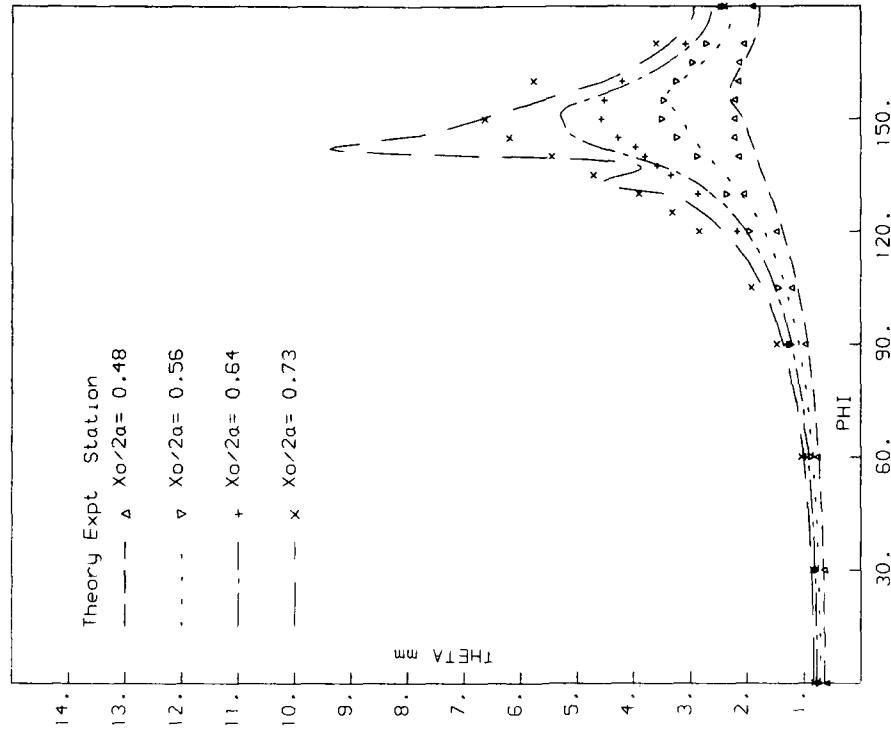
Δ ▽ + × EXPERIMENT



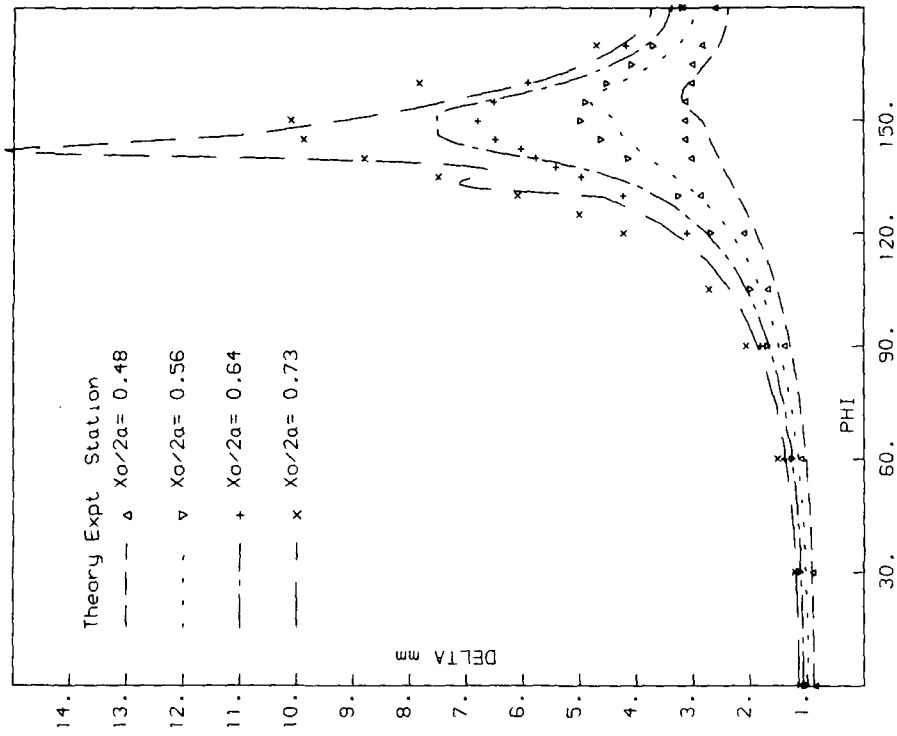
ONERA/CERT Method Recalculated External Flow



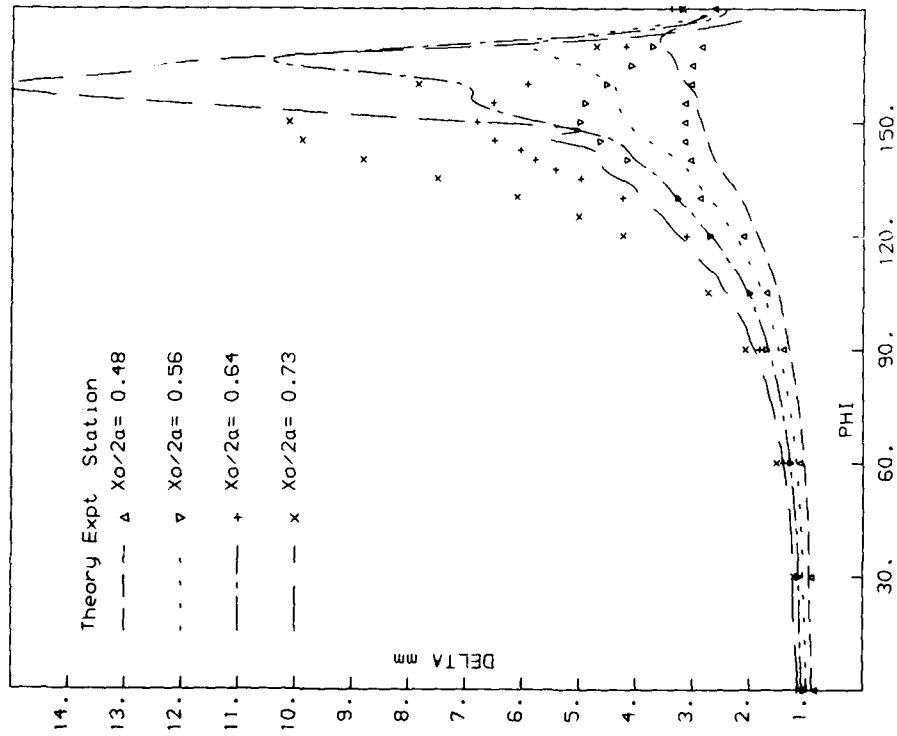
ONERA Method



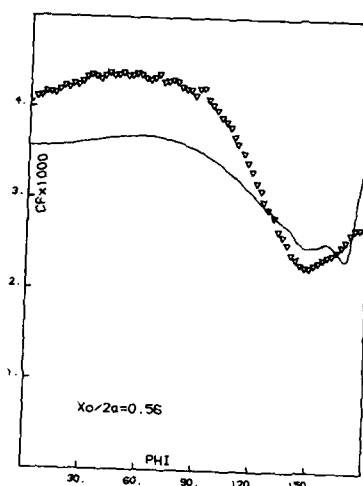
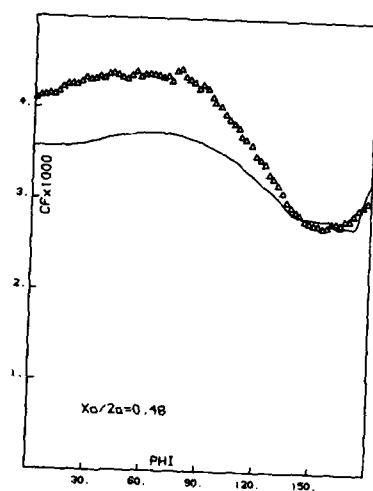
ONERA Method Theoretical External Flow



ONERA Method Theoretical External Flow

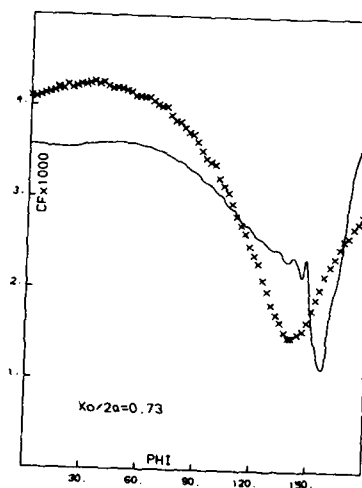
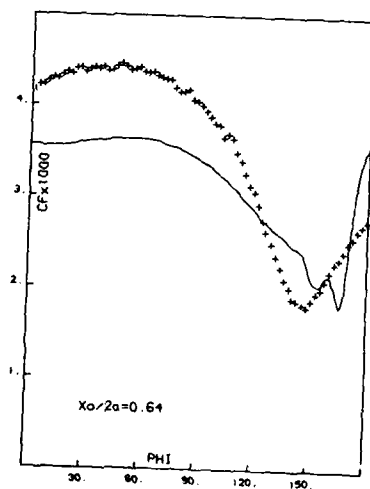


ONERA Method

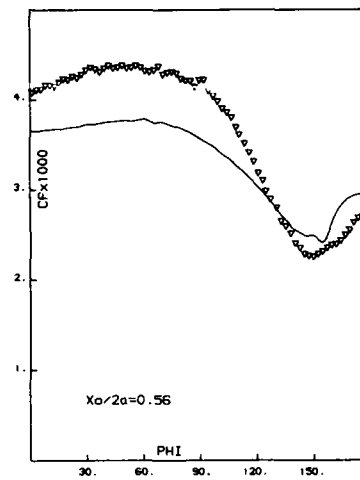
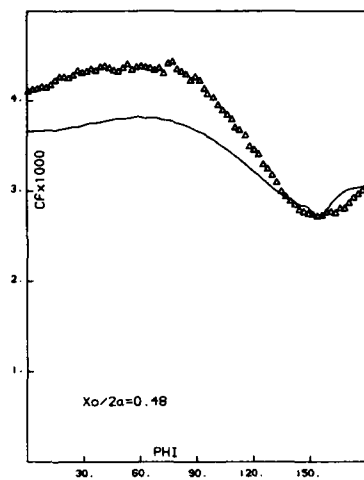


— THEORY

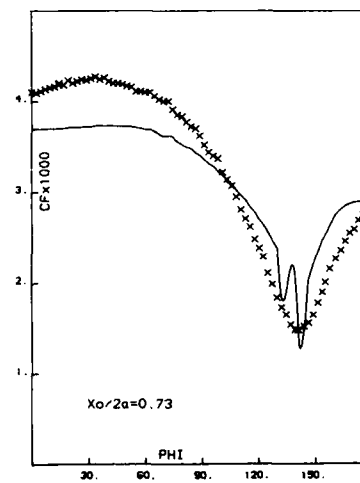
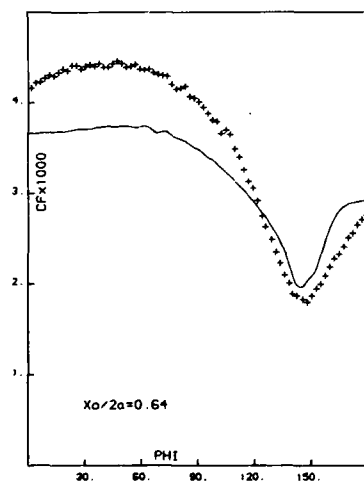
$\Delta \nabla + \times$ EXPERIMENT



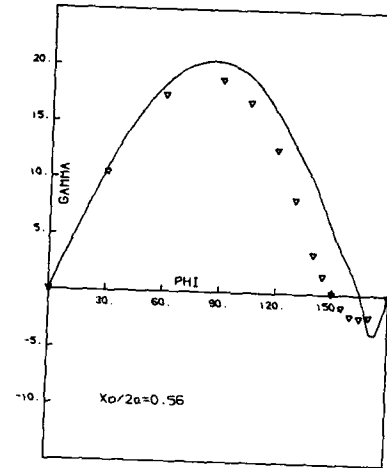
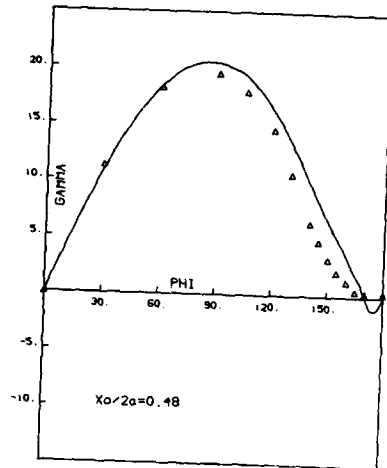
ONERA Method



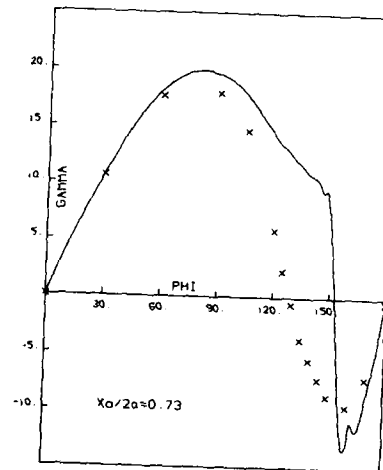
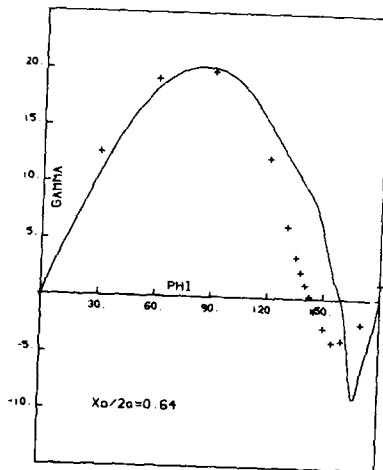
— THEORY
 $\Delta \nabla + \times$ EXPERIMENT



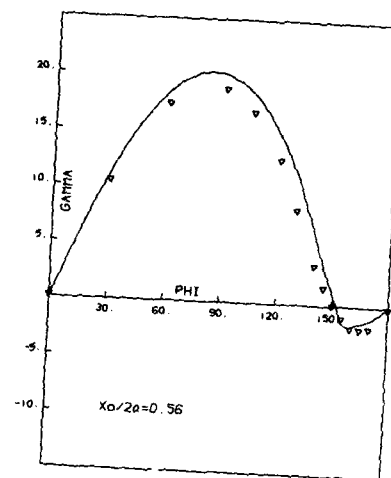
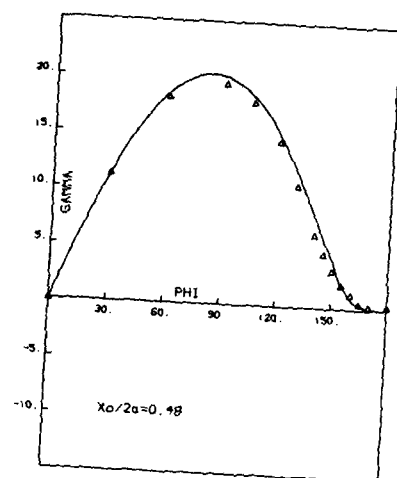
ONERA Method Theoretical External Flow



— THEORY
 $\Delta \nabla + \times$ EXPERIMENT

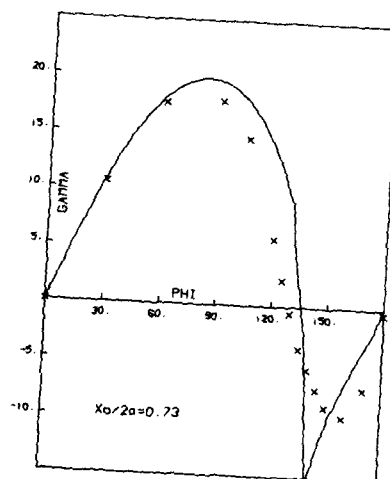
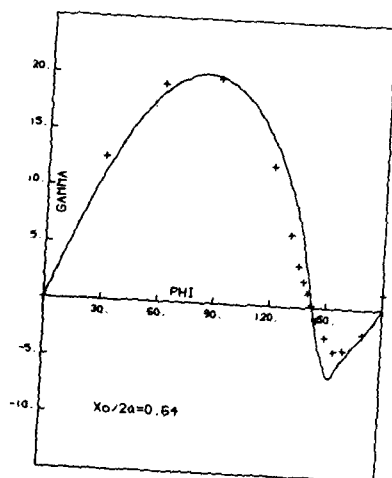


ONERA Method

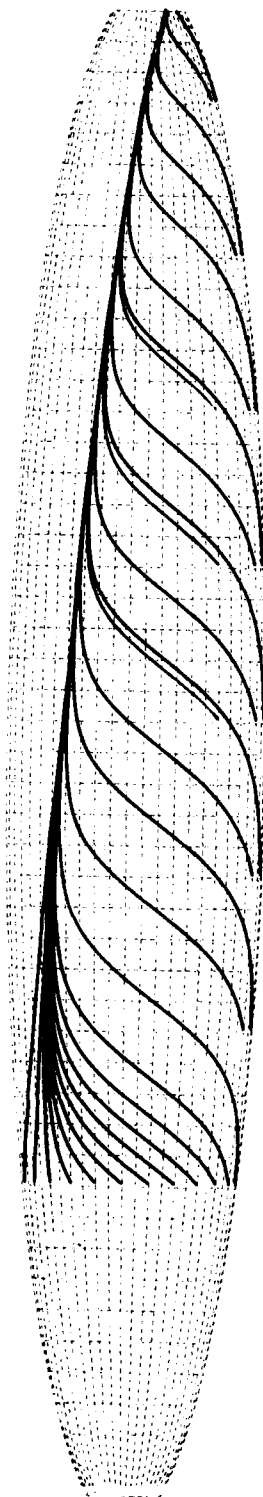


— THEORY

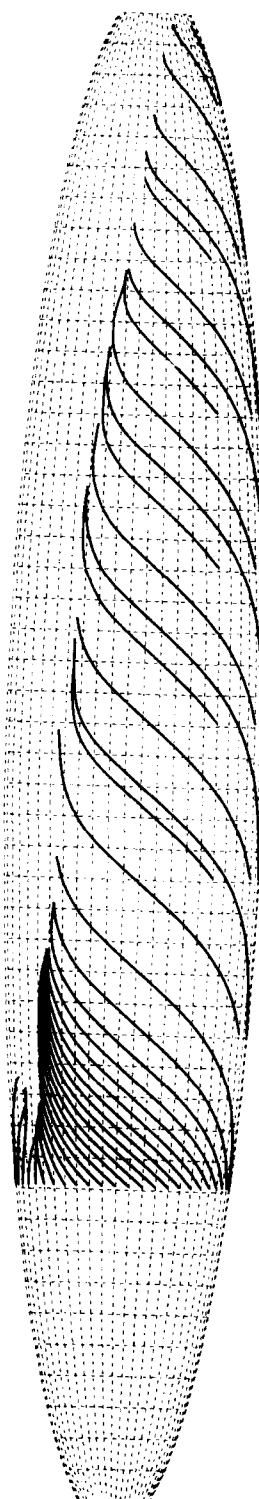
$\Delta \nabla + \times$ EXPERIMENT



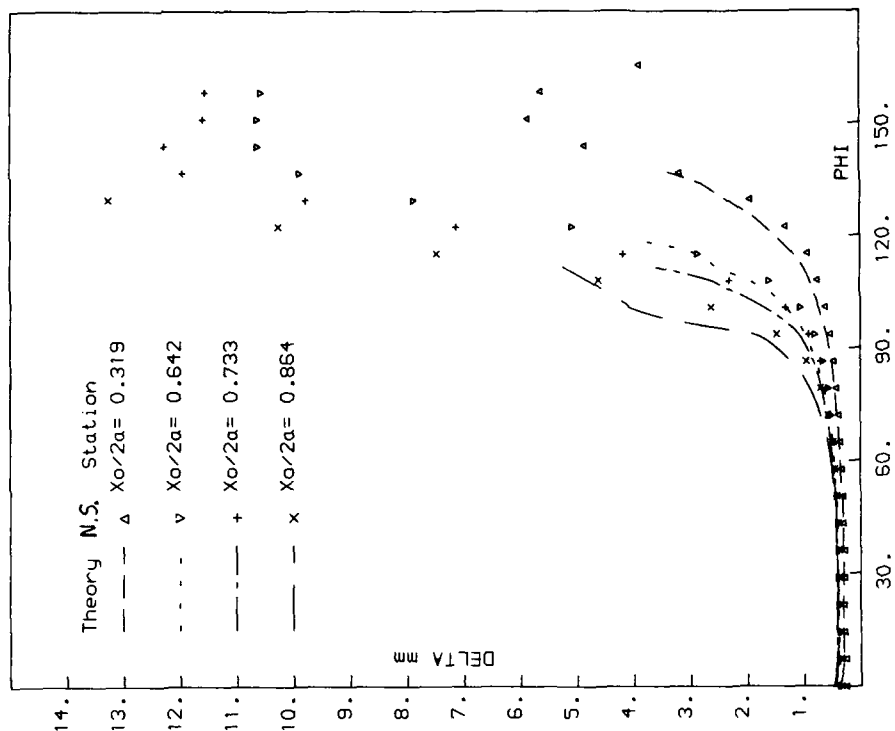
ONERA Method Theoretical External Flow



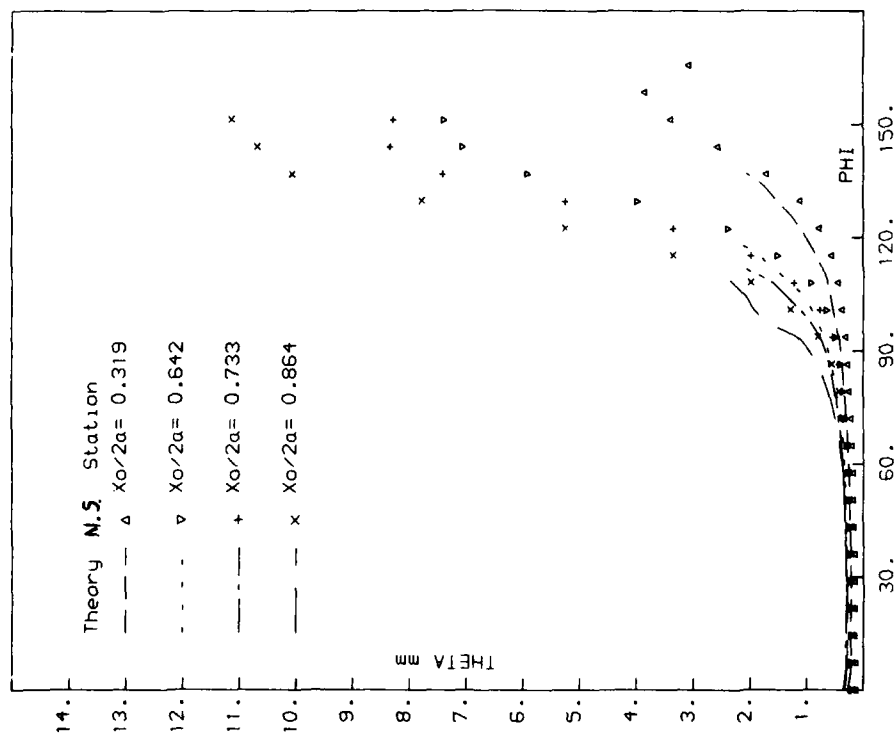
30 Deg Case wall streamlines computed from wall angle given by Navier-Stokes results



ONERA/CERT Method wall streamlines obtained with edge defined by $P_i/P_{i0} = .99$



30 Deg Case ONERA/CERT Method



30 Deg Case ONERA/CERT Method

6.2 Field methods

T. Cebeci, Douglas Aircraft, CA, USA

6.2.1 The ellipsoid at 10° incidence

The calculations for this test case were performed by Cebeci [DAC], Hirschel and Monnoyer [MBB], Humphreys [FAA], Menter [DFVLR], and van den Berg et al. [NLR] using the boundary-layer procedures of Chapter 4b with external velocity distributions which will be indicated.

The results obtained by Cebeci are described in detail in [3] and made use of the external boundary condition determined from the solution of inviscid flow equations. The distributions of momentum and displacement thickness show similar trends to those of Section 6.1 where, in general, the external boundary conditions determined by Stock were used, but here particularly for ϕ greater than 120° the calculations are in much better agreement with measurements. There is a tendency, for angles of 120° , for the calculations to underpredict at low values of $x/2a$ and to overpredict at the furthest downstream station. This is probably due to the external velocity boundary condition, as described in [3] and discussed above in relation to Fig. 1. The skin-friction results display the experimental trends and are within 15% of the measured values with some underprediction in regions which are consistent with the experimental pressure distribution as argued in [3]. The flow angles show even better agreement except, again, in the downstream region where the boundary conditions are subject to uncertainty.

The results obtained by Hirschel and Monnoyer [MBB] made use of the inviscid external velocity distribution and a brief description of the method and the results provided by Monnoyer are given below.

The calculations were performed on the 1:6 ellipsoid at 10° incidence. The Reynolds number based on the ellipsoid major axis was 7,700,000 and the freestream Mach number 0.17. Transition was tripped at $x/2a = 0.2$.

The mesh had 89 nodes in the axis direction, 61 points equally spaced in the cross-flow direction (half body), and 51 across the boundary layer. The initial profiles were computed at $x/2a = 0.0013$, and the calculation was laminar until $x/2a = 0.2$; intermittency was applied until $x/2a = 0.225$, where the flow became fully turbulent. The outer flowfield was obtained from the potential flow solution, and no displacement effect was applied to the inviscid part of the flow.

Results of the calculation neglecting (MBB-1) and including (MBB-2) the effect of surface curvature are compared with experiment. The circumferential distributions of the pseudo two-dimensional displacement thicknesses, the flow angles at the wall and the skin-friction coefficients are plotted at four stations. In addition, the wall pressure distribution is provided. The comparison of both calculations shows that curvature plays a role on the boundary-layer flow as the boundary-layer thickness increases, namely on the leeside region. Since the velocity profiles at the vicinity of the wall are only marginally modified, no significant changes are to be seen on the skin friction and the wall flow direction, although there is a trend towards the measured values. On the other hand, the effect of curvature on the metric coefficients away from the wall largely affects the solution at the outer part of the boundary layer as illustrated by the displacement thicknesses.

Concerning the comparison with experiment, only wall flow angles γ_w agree satisfactorily, except on the leeside at the last station where it is clear that the analytical potential flow solution does not hold anymore. It is interesting to note that much better agreement between the calculated and measured values is obtained if the latter are slightly "translated" as follows: the flow angles at each station are shifted so that the symmetry condition ($\gamma_w = 0$) at the leeside is satisfied leading to shiftings not larger than 0.7° ; the skin-friction coefficients are translated downwards by a constant value of $\Delta c_f = 0.00025$, in order to fit them with the computed ones; a shift $\Delta c_p = 0.025$ is applied to the measured pressure so that better agreement with the potential flow solution is obtained, especially on the windward side. It is indeed surprising that discrepancies are smaller at the leeside where it is expected that the deviation of the actual pressure distribution from the theoretical inviscid pressure should be larger than at the windward side.

The results obtained by Humphreys made use of the experimental pressure distribution as extracted by Stock. They show increasing deviations from the measurements as the circumferential angle increases beyond 120° with some discontinuities which may stem from the details of the numerical procedure.

Menter [DFVLR] has used a second-order accurate finite-difference method which is based on the standard and the zig-zag box method [4-5]. He has performed four sets of computations by using different boundary conditions at the boundary-layer edge. A description of the results provided by him is given below.

For the first set, the boundary conditions were taken from potential flow theory. Figure a1 shows the wall streamline angles and Fig. a2 the local displacement thickness at four different x-stations. The computations are generally in good agreement with the experiments except in a small region in the rear part of the body at $\phi \approx 140^\circ$. There a discontinuous (weak) solution builds up in the direct mode computations. This discontinuity is certainly a feature of the boundary-layer equations itself [6] when solved in the direct mode and could not be removed by changing the grid resolution.

A second set of calculations has been performed by using the external velocity field computed by Haase and Stock [7] on the basis of the experimental pressure distribution. An improvement of the results could not be achieved, as can be seen in Figs. b1 - b3. The reasons are first that the computations are still performed in the direct mode so that singularities in the solution are not excluded and second the computations of [7] do not automatically fulfill the symmetry condition at the leeward line of symmetry, leading to the unphysical behavior of the boundary-layer method.

The singular behavior can be avoided by using inverse boundary conditions as shown by [8-9]. In the present case half inverse boundary conditions were used by specifying first the length of the velocity vector at the boundary-layer edge from the experimental wall pressure distribution via the Bernoulli equation and second the direction of the wall streamline. This experimental input was used, because it can be measured quite accurately. The direction of the external streamline was computed with a Newton iteration. Figures c1 - c3 show the results (remember that c1 shows the input). One can see that the discontinuity in the solution is avoided and that the results (Fig. a2) are in good agreement with the measurements.

In order to avoid the need of an experimental input, first results were produced by coupling the Euler and the boundary-layer equations. The boundary layer was simulated with the wall transpiration approach [10] in the space-marching parabolized Euler solver. The correction for the wall pressure was computed at the boundary-layer edge, defined as follows:

$$\left(\frac{u}{u_e} + \frac{w}{w_e} \right) \cdot \frac{1}{2} = 0.9 \quad \text{at } y = \delta$$

Figures d1 - d3 show the results of this viscous-inviscid interaction method. The singularity in the solution is completely avoided, as was expected and the computations are in much better agreement with the measurements than those of Figs. a1 - a3. It should be noted that the major shortcoming of the viscous-inviscid interaction approach is the arbitrariness in the definition of the boundary-layer edge (coupling location). This problem can only be avoided by using parabolized or full Navier-Stokes methods [11,12].

Calculations performed by J. I. van den Berg, Lindhout and B. van den Berg of NLR, for the prolate spheroid at 10° angle of attack were carried out with BOLA, the NLR calculation system for three-dimensional boundary layers. The calculations were started at $x_0/2a = 0.30$ with given initial viscous flow conditions. As a boundary condition the surface pressure distribution was employed, the flow angle at the boundary-layer edge being obtained from an integration of the Euler equations. A description of their results provided by them is given below.

In a first report [13] grid dependence and the effect of changing the empirical constants in the turbulence model were investigated. Refinement of the grid was found to have little influence and the choice of slightly different constants in the turbulence model did not lead to essentially different results. In a second report [14], the influence of initial data and boundary conditions on the calculation results was investigated. Three calculations were performed subject to the following initial and boundary conditions:

1. Measured pressure distribution; initial flow conditions at $x_0/2a = 0.30$ from Cebeci (based on boundary-layer calculations from the nose using the potential flow boundary condition).
2. Potential flow pressure distribution; initial flow conditions at $x_0/2a = 0.30$ from Cebeci.
3. Measured pressure distributions; initial flow conditions at $x_0/2a = 0.30$ from Gleyzes (different edge stream angles, obtained by fitting calculations to available measurement data at $x_0/2a = 0.48$).

The first case represents the initial and boundary conditions as defined for this test case by the Working Group.

The calculation results for the three cases and the experimental data at the sections $x_0/2a = 0.48, 0.56, 0.64$ and 0.73 are plotted in a series of graphs appended. For the test case conditions defined by the Working Group (case 1), the calculation results are seen to compare not well with experiment at the leeward side of the prolate spheroid. The region of flow convergence is predicted essentially too close to the symmetry line. The calculations with the same initial conditions and the potential flow pressure distribution (case 2) produce results in much better agreement with experiment, though the displacement thickness peak is substantially overestimated. Comparatively

smooth results are obtained, probably because the initial and boundary conditions used are smooth and compatible. Best overall agreement is obtained when the measured pressure distribution is used together with initial edge flow angles derived indirectly from the measurements (case 3).

It is concluded that the test case is dominated to a great extent by the boundary and initial conditions. More specifically boundary and initial conditions can probably not be prescribed independently. The poor results for case 1 seem to be due to prescribing the measured pressure distribution together with initial edge stream angles from potential flow. The solution of the Euler equations downstream of the initial line will lead then to an essentially wrong edge stream angle distribution.

The objective of the Working Group is to determine the limits of boundary-layer calculation procedures in 3-D separation regions. The last figure shows the computed boundary-layer thickness distribution at two sections in the rear part of the prolate spheroid. No problems were encountered in performing the boundary-layer calculations, but the large circumferential thickness variations indicate that the boundary-layer approximation (comparatively large derivatives normal to the surface) does not hold anymore and determines the limit here.

6.2.2 The C-wing

The calculations were performed at DAC by Kaups, Mehta and Cebeci [15] at the design angle of attack of 5 degrees, at Mach numbers of 0.70, 0.82, 0.85 and 0.90 for a Reynolds number of 6.8×10^6 . The interactive boundary-layer approach, based on the strip-theory approach to three-dimensional flow, has been described in [16] and incorporates viscous effects into the inviscid flow through a surface-blowing boundary condition. Two inviscid-flow procedures corresponding to a full-potential code [17] and an Euler code were used in the calculations. The transonic potential code was used in nonconservative form with a numerical grid of $161 \times 25 \times 33$ mesh points and the Euler code $145 \times 25 \times 31$ mesh points arranged in a C-grid in the streamwise and spanwise directions, in some cases with an H-grid in the spanwise direction.

Figure 2 allows comparison of the measured and calculated results at $M_\infty = 0.70$. The interactive calculations with the Euler code and H-grid spanwise, and with full potential code agree well with experimental data except near the leading edge where the flow is supercritical. As expected, the calculated lift coefficients also agree well with the normal force coefficient $C_N = 0.483$ calculated from the measured pressure distributions. It is evident that calculations with the Euler code and C-grid in both directions reproduce the velocity peaks more accurately except near the wing tip where the local lift is overpredicted over the whole chord. The results of Figure 3 correspond to $M_\infty = 0.82$ and show attached flow with shocks. The interactive calculations with the Euler code are closer to the measurements than those with the full-potential flow solutions. The C-grid was used in both directions mainly to improve results near the wing tip but it is clear that better agreement with experiments has resulted near the shock location and over the whole wing apart from the wing tip where the lift tends to be overpredicted, and caused the wing lift coefficient to exceed the measured normal force coefficient $C_N = 0.53$. It should be noted that the predicted pressure recovery near the trailing edge at the wing tip differs in all cases from the measured values indicating a strong decambering effect in the experiment.

Figure 4 shows results at the design condition at which flow visualization has shown the flow in the outer 30 percent of the span to be separated due to strong shock-boundary-layer interaction. The calculations are in good agreement with experiment except in the region of the separation bubble, and the corresponding lift coefficient is only slightly lower than the measured value of C_N of 0.54. It is surprising that the results obtained by interaction with the full potential flow method are in better agreement with those with the Euler method than the results of Figure 3. The pressure distributions obtained at $M_\infty = 0.9$ and the full-potential code are again in reasonable agreement with experiments on the inboard and middle portions of the wing, as shown in Figure 5; the predictions on the outboard portion of the wing show attached flow whereas the experiments suggest separation because the predicted shock pressure rise is spread out over a considerable distance. Despite this discrepancy, the predicted lift coefficient is close to the measured normal force coefficient C_N of 0.56.

REFERENCES

1. Keener, E.R., Computational-Experimental Pressure Distributions on a Transonic, Low-Aspect Ratio Wing, AIAA paper 84-2092, Aug. 1984, Seattle, Wash.
2. Keener, E.R., Pressure-Distribution Measurements on a Transonic Low-Aspect Ratio Wing, NASA TM 86683, Sept. 1985.
3. Cebeci, T. and Meier, H.U., Turbulent Boundary Layers on a Prolate Spheroid, AIAA Paper.
4. Cebeci, T., Khattab, A.A. and Stewartson, K.: Three-Dimensional Laminar Boundary Layers and the Role of Accessibility, J. Fluid Mech. 107, 1981.
5. Krause, E., Hirschel, E.H., Bothmann, Th.: Die numerische Integration der Bewegungsgleichungen dreidimensionaler laminarer Grenzschichten, Fachtagung "Aerodynamik," Berlin 1968, DGLR Fachbuchreihe, Bd. 3, 1969.

6. Cousteix, J. and Houdeville, R.: Singularities in Three-Dimensional Turbulent Boundary-Layer Calculations and Separation Phenomena, AIAA J. Vol. 19, No. 8, pp. 976-985, 1981.
7. Haase, W. and Stock, H.W.: Ein Verfahren zur Ermittlung des äquivalenten reibungsfreien Geschwindigkeitsfeldes an dreidimensionalen Konfigurationen aus gemessenen Wanddrücken bei inkompressibler Strömung, ZFW, Vol. 10, pp. 97-106, 1986.
8. Radwan, S.F. and Lekoudis, S.G.: Inverse Mode Calculations of the Incompressible Turbulent Boundary Layer on an Ellipsoid, AIAA J., Vol. 24, No. 10, pp. 1628-1635, 1986.
9. Barberis, D.: Calcul de la couche limite tridimensionnelle en mode direct ou inverse sur des obstacles quelconques, Le Recherche Aerospatiale, No. 3, pp. 169-195, 1986.
10. Lighthill, M.J.: On Displacement Thickness, J. Fluid Mech., Vol. 4, 1958.
11. Rosenfeld, M., Israeli, M. and Wolfstein, M.: Numerical Study of the Skin Friction on a Spheroid at Incidence, AIAA J., Vol. 26, No. 2, pp. 129-136, 1988.
12. Panaras, A.G. and Steger, J.L.: A Thin Layer Solution of the Flow About a Prolate Spheroid, ZFW, Vol. 12, pp. 173-180, 1988.
13. Van den Berg, J.I., Lindhout, J.P.F. and Van den Berg, B.: Calculations of the Boundary Layer Around an Ellipsoid at 10° Angle of Attack. NLR MP 84726 U, 1987.
14. Van den Berg, J.I., Lindhout, J.P.F. and Van den Berg, B.: Comparison of Calculations of the Boundary Layer Along a 1:6 Ellipsoid at 10° Angle of Attack. NLR Memo. IN-88-005 U, 1988.
15. Kaups, K., Mehta, U. and Cebeci, T., Interactive Boundary-Layer Calculations of a Transonic Wing Flow, To be published in J. Aircraft.
16. Chen, L.T., Vassberg, J.C., Chang, K.C. and Cebeci, T., A Transonic Wing/Body Flow-field Computational Method Using a General Grid Generation Scheme and an Inverse Boundary-Layer Method, Vol. I, Theory, Douglas Aircraft Co. Rept. No. MDC J3773-1, Jan. 1986.
17. Chen, L.T., Vassberg, J.C. and Peavey, C.C., A Transonic Wing-Body Flowfield Calculation with Improved Grid Topology and Shock-Point Generators, AIAA J., Vol. 23, Dec. 1985, pp. 1877-1884.

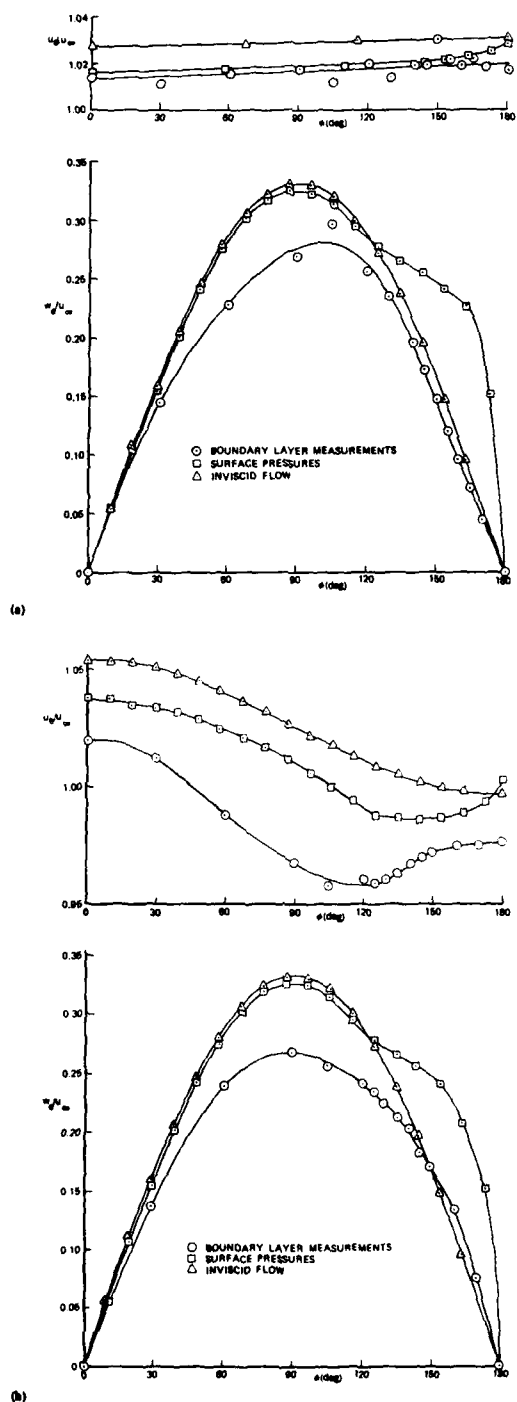
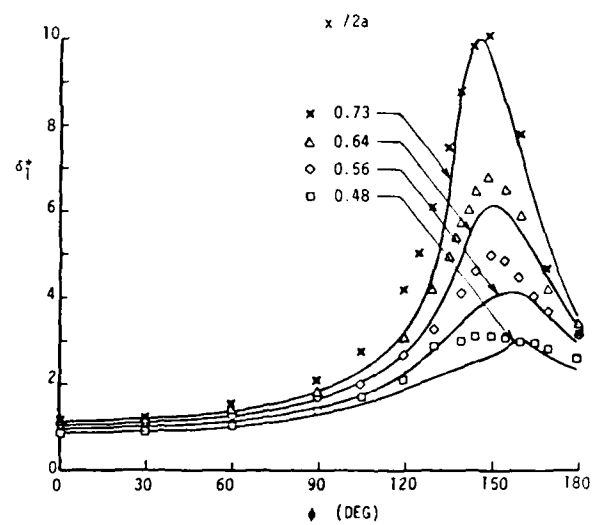
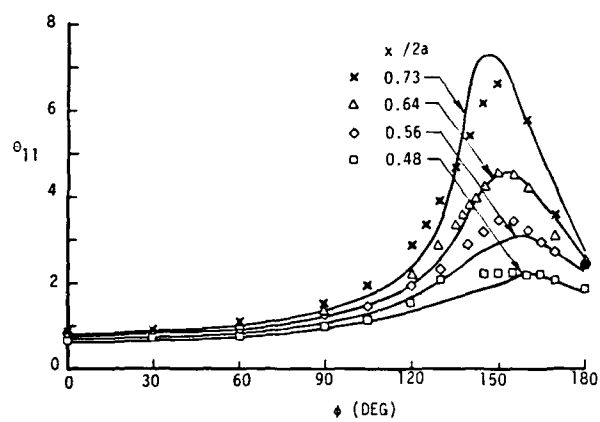
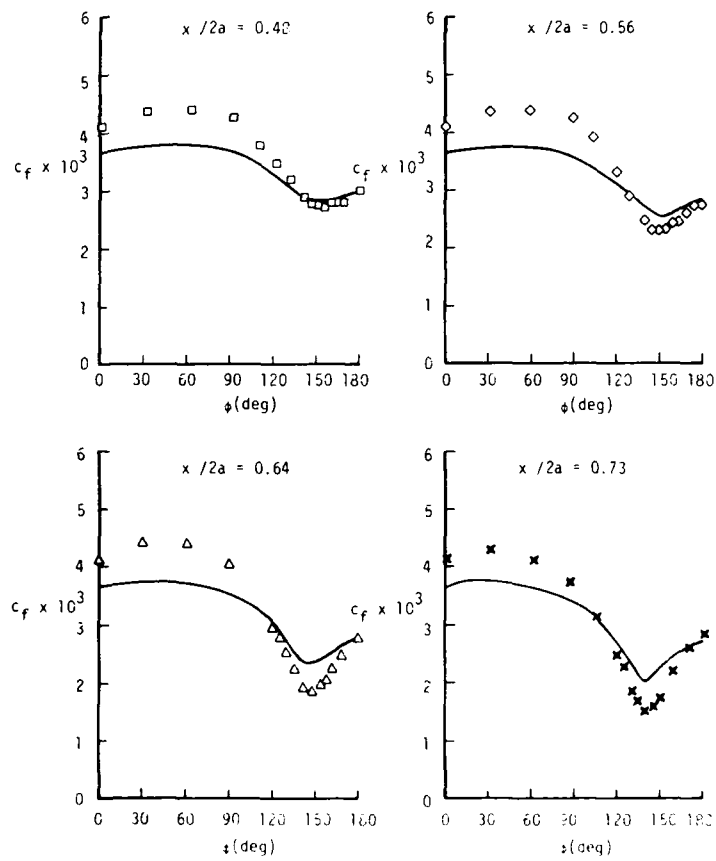


Figure 1. Comparison of calculated, measured, and extracted streamwise and circumferential velocity components for the prolated spheroid at (a) $x/2a = 0.48$, (b) $x/2a = 0.73$.

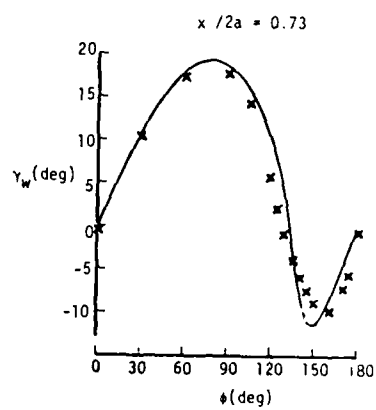
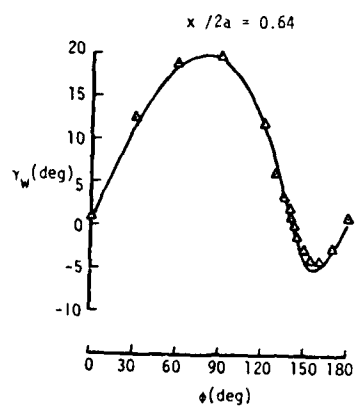
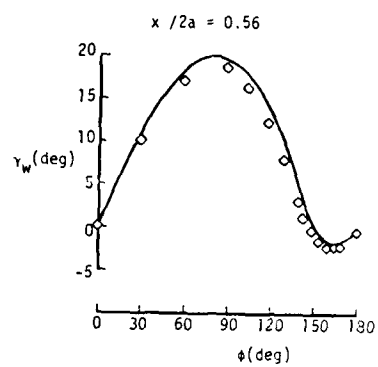
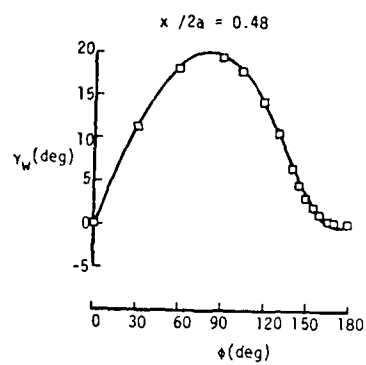
CEBECI RESULTS



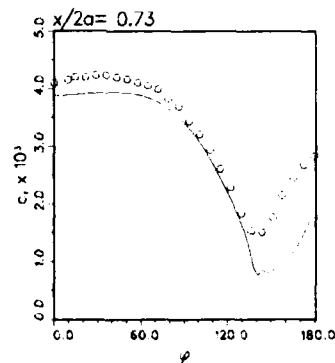
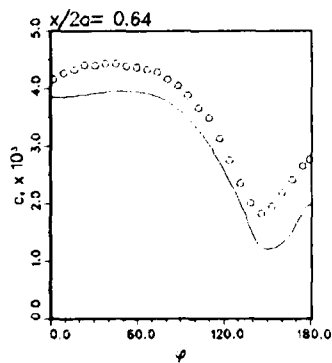
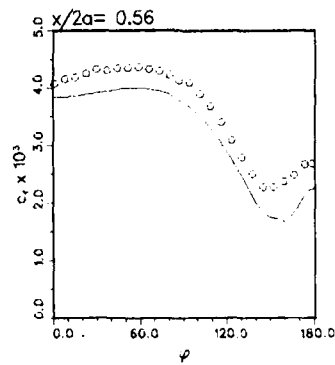
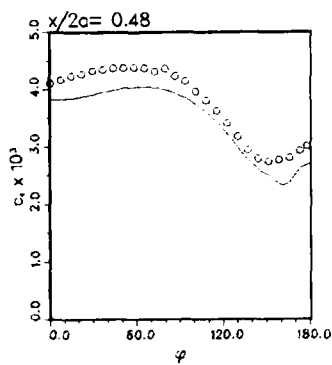
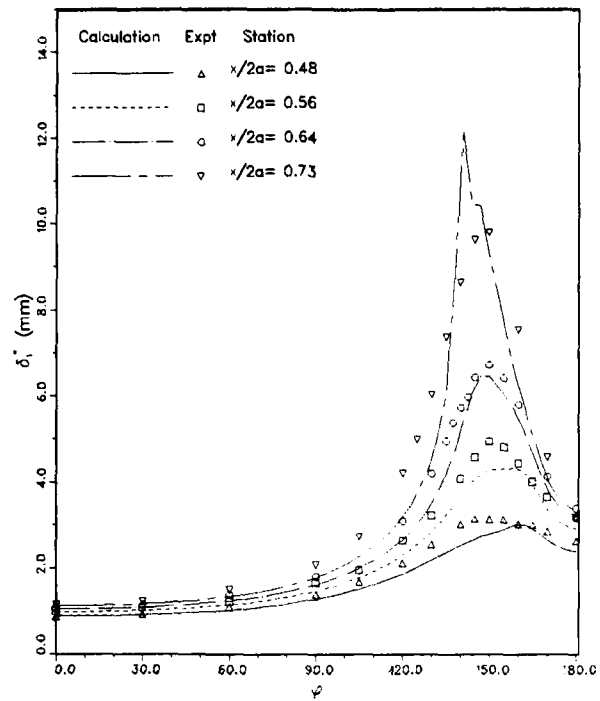
CEBECI RESULTS



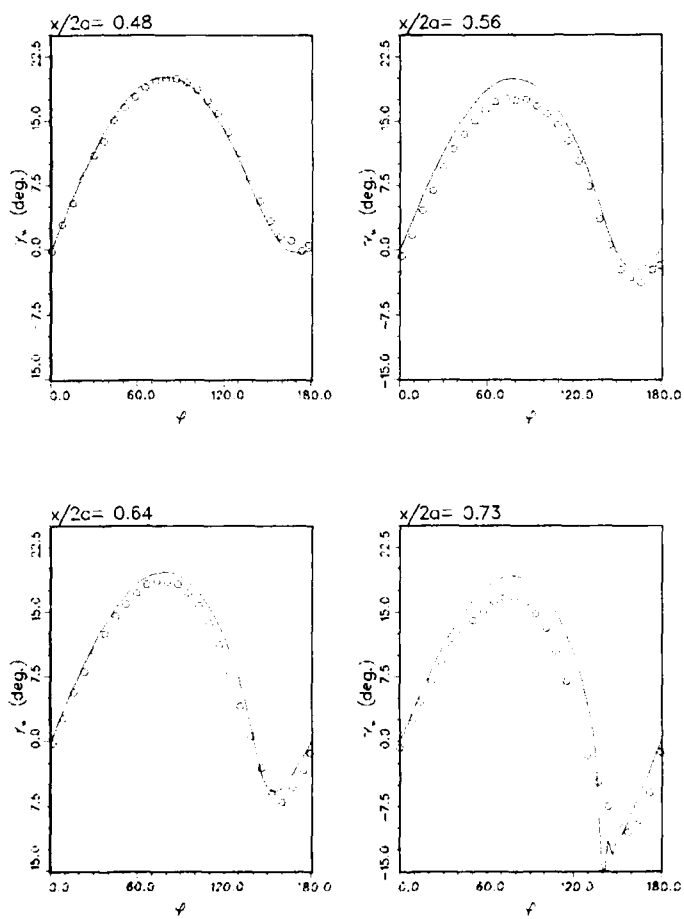
CEBECI RESULTS



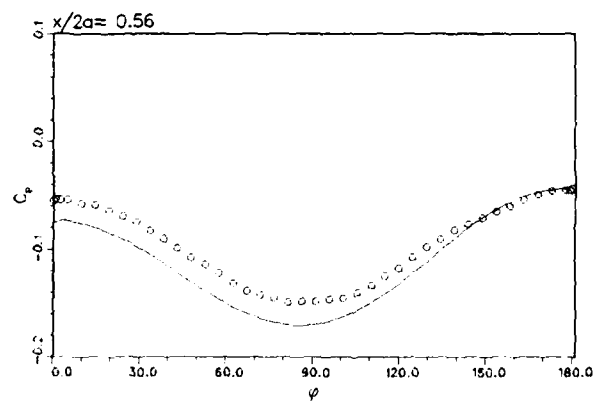
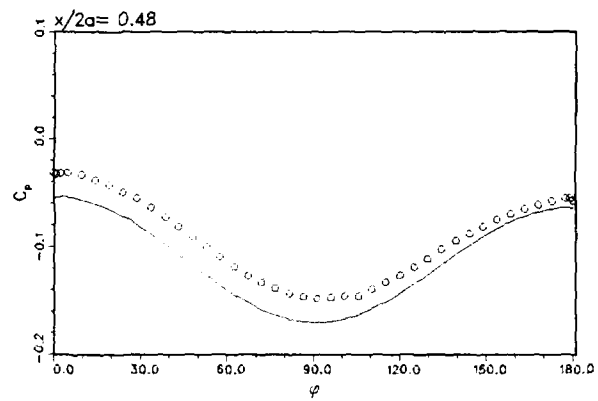
MBB-2 Results



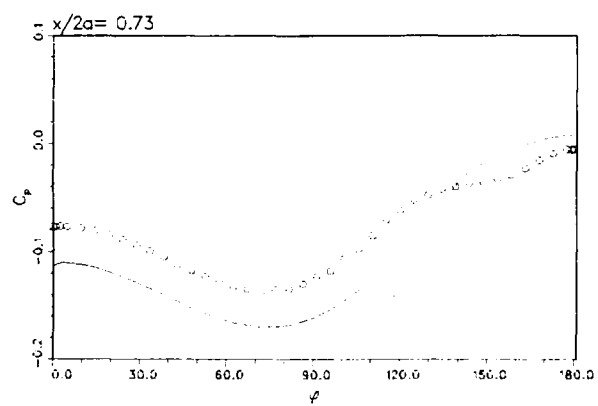
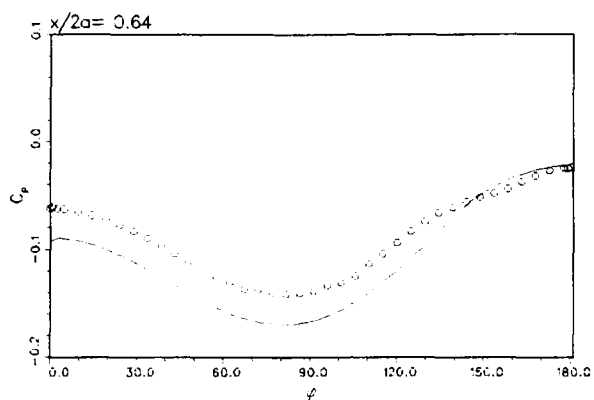
MBB-2 Results



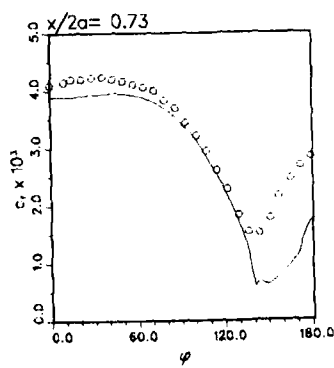
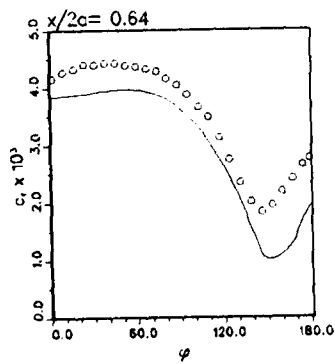
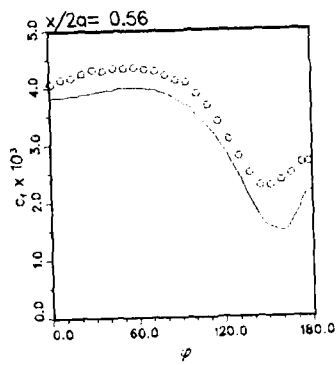
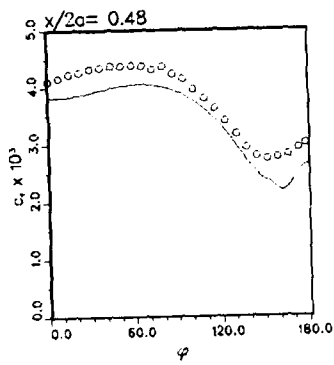
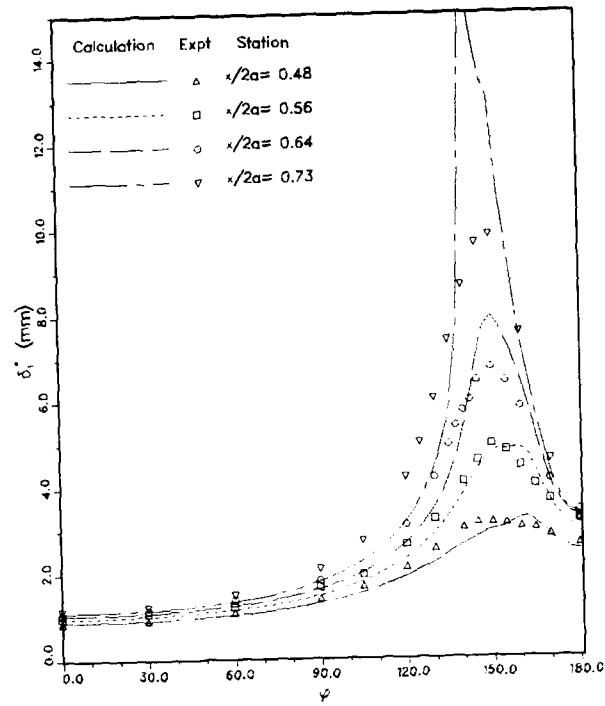
MBB-2 Results



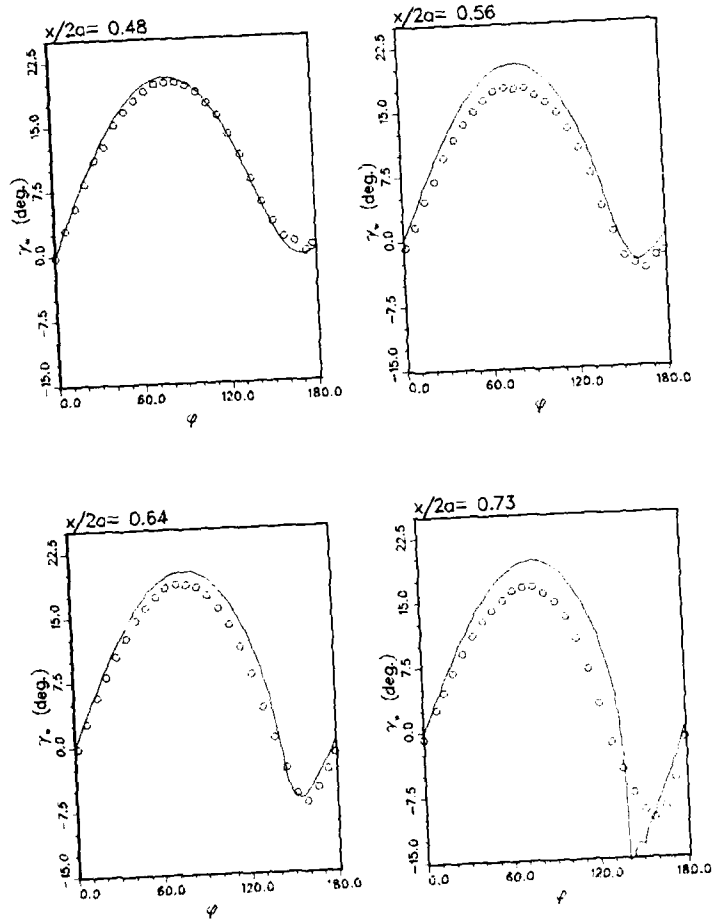
MBB-2 Results



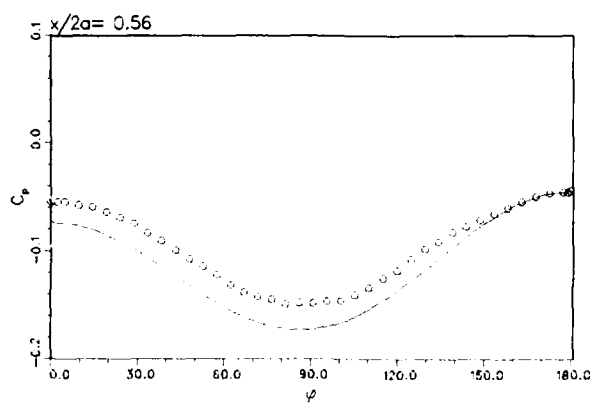
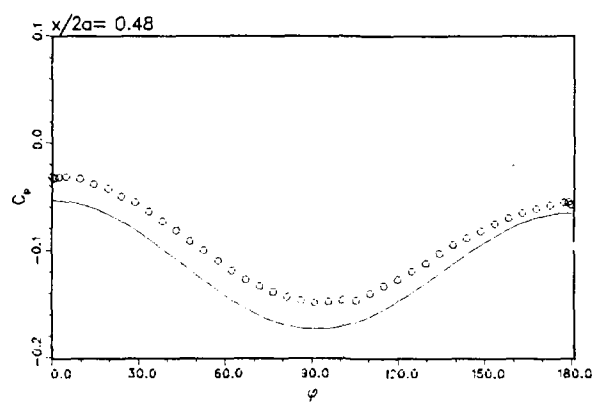
MBB-1 Results



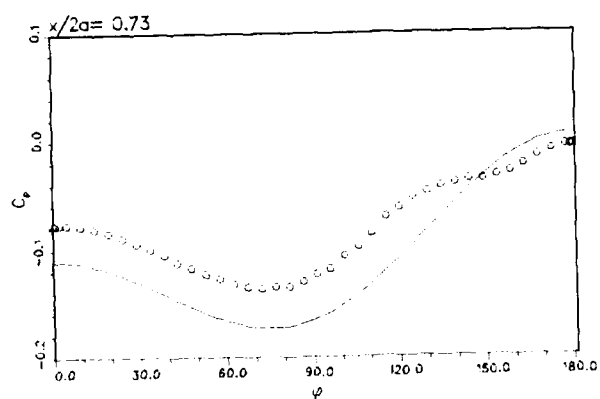
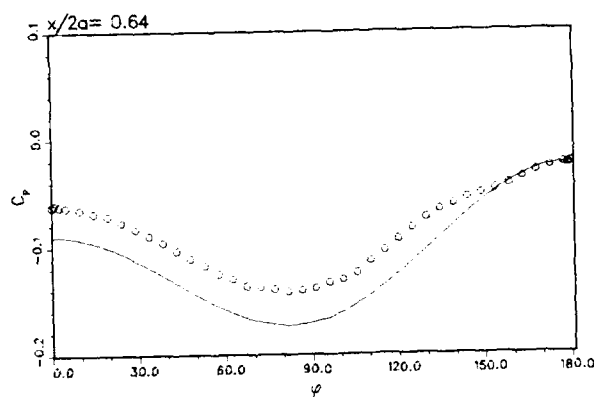
MBB-1 Results



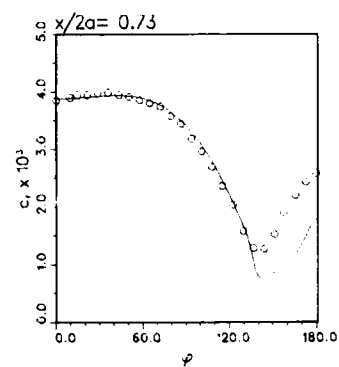
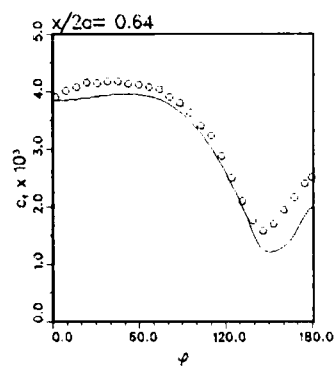
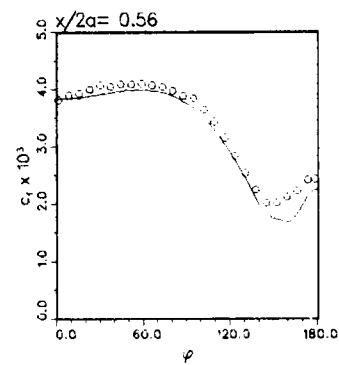
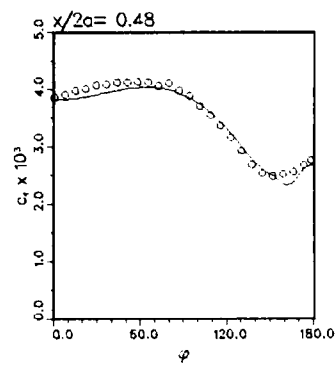
MBB-1 Results



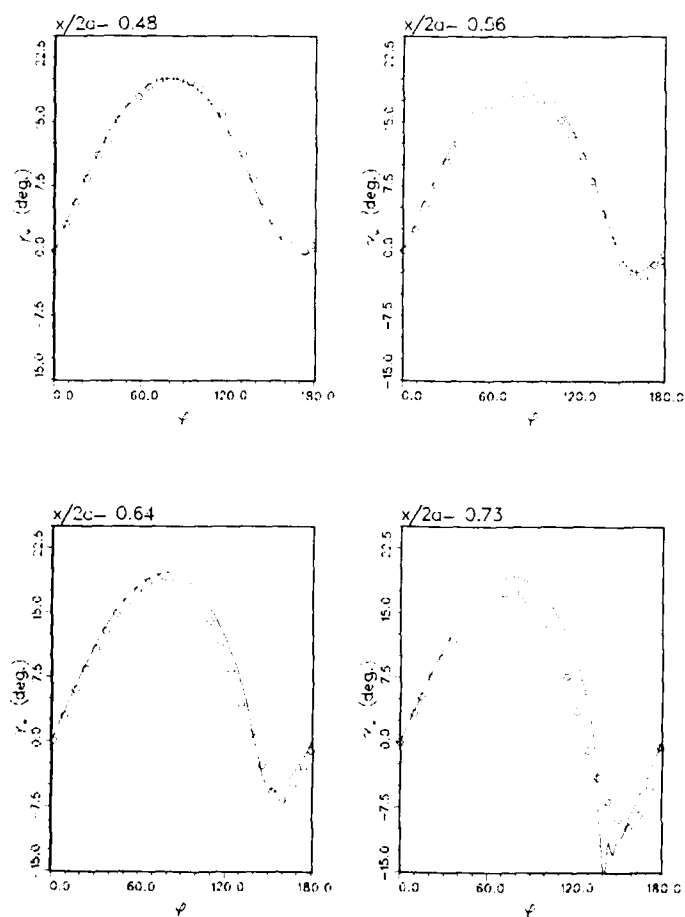
MBB-1 Results



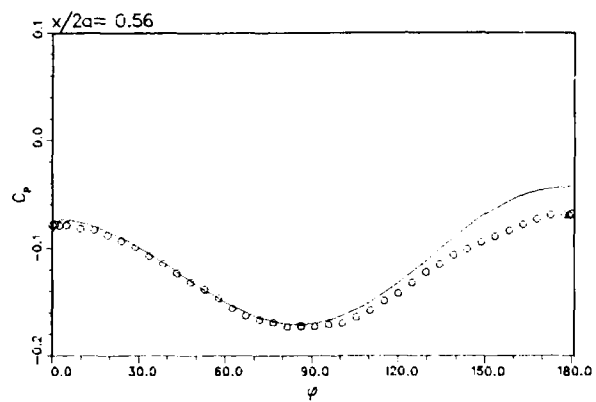
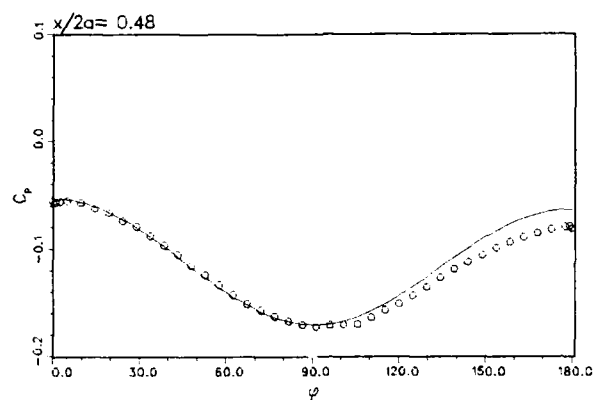
MBB-2 Results ("translated" measurements)



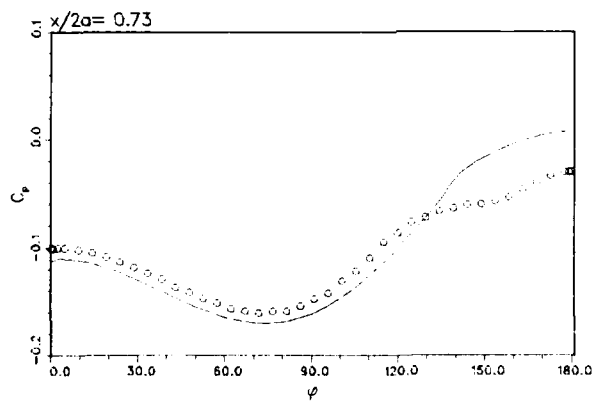
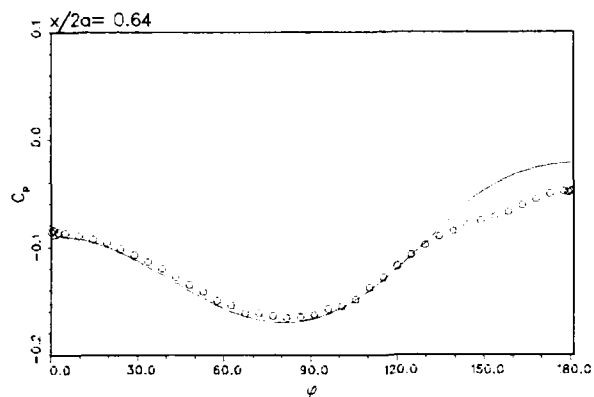
MBB-2 Results ("translated" measurements)



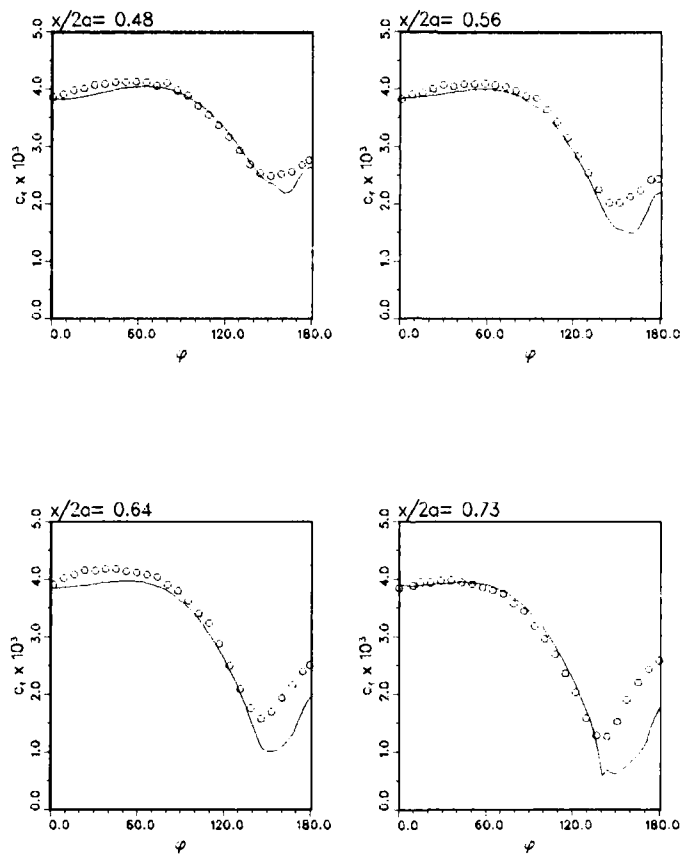
MBB-2 Results ("translated" measurements)



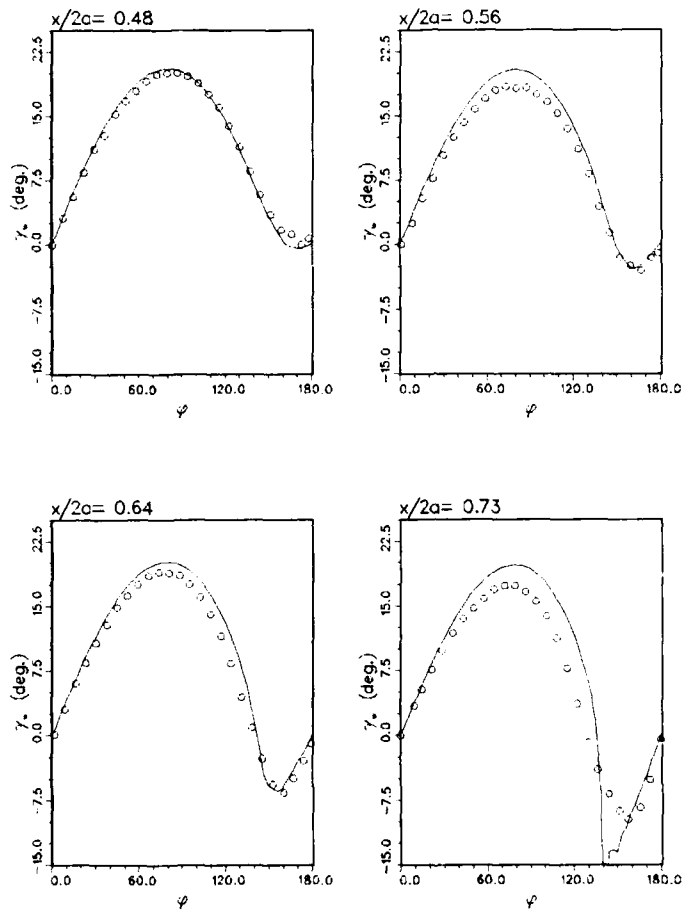
MBB-2 Results ("translated" measurements)



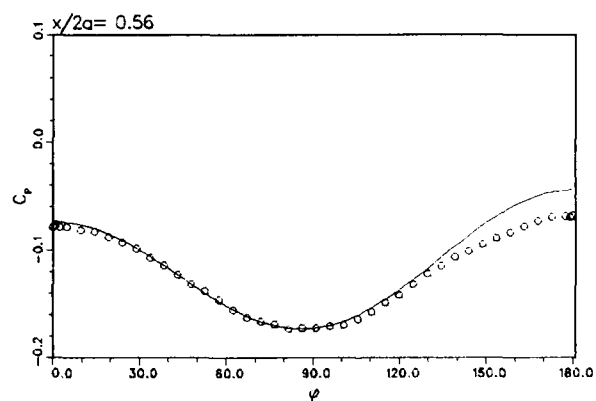
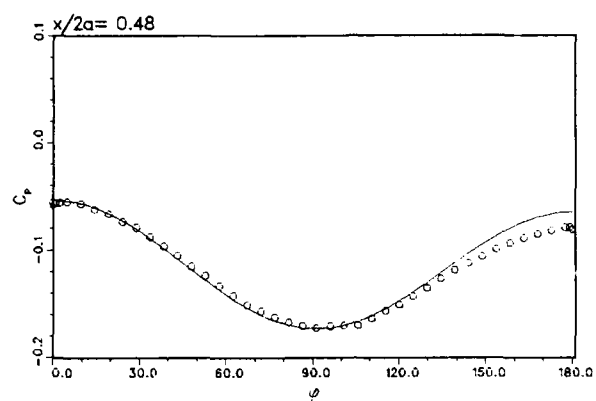
MBB-1 Results ("translated" measurements)



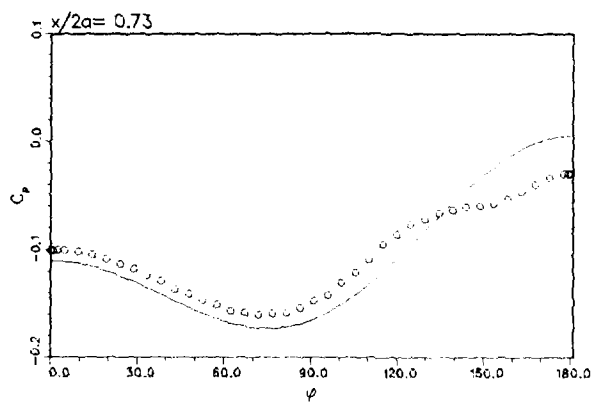
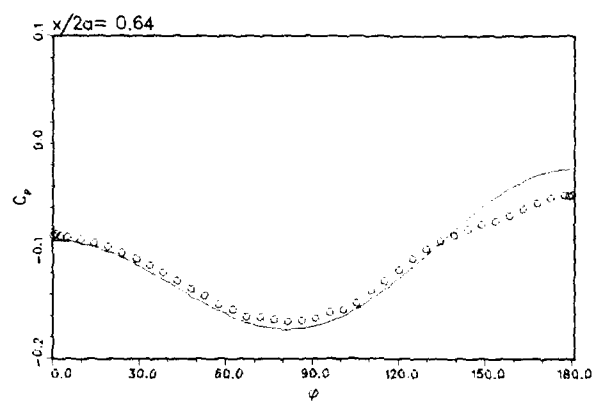
MBB-1 Results ("translated" measurements)



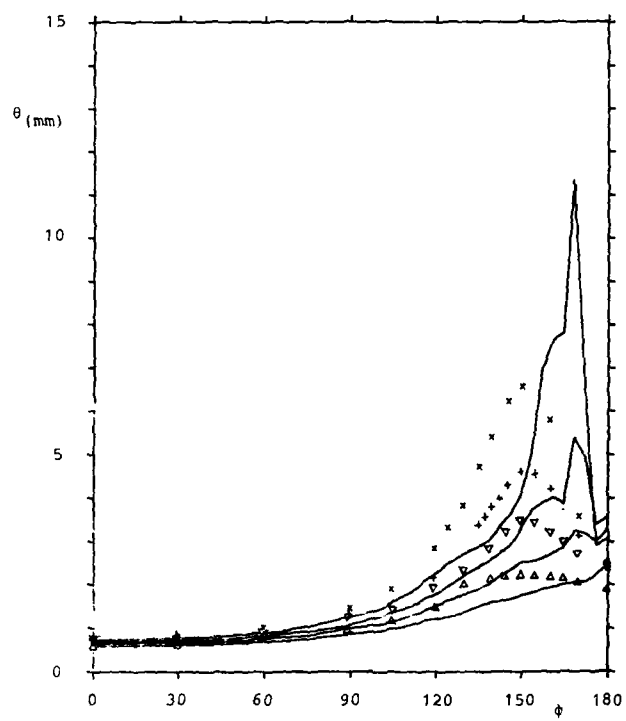
MBB-1 Results ("translated" measurements)



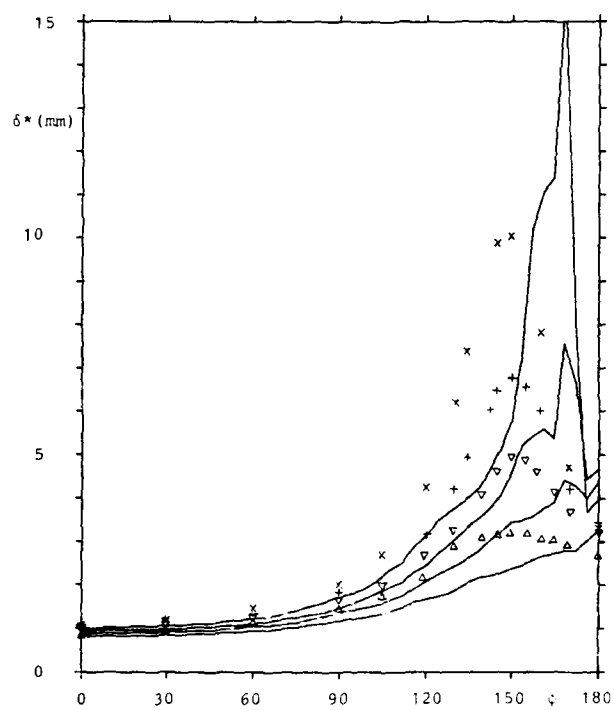
MBB-1 Results ("translated" measurements)



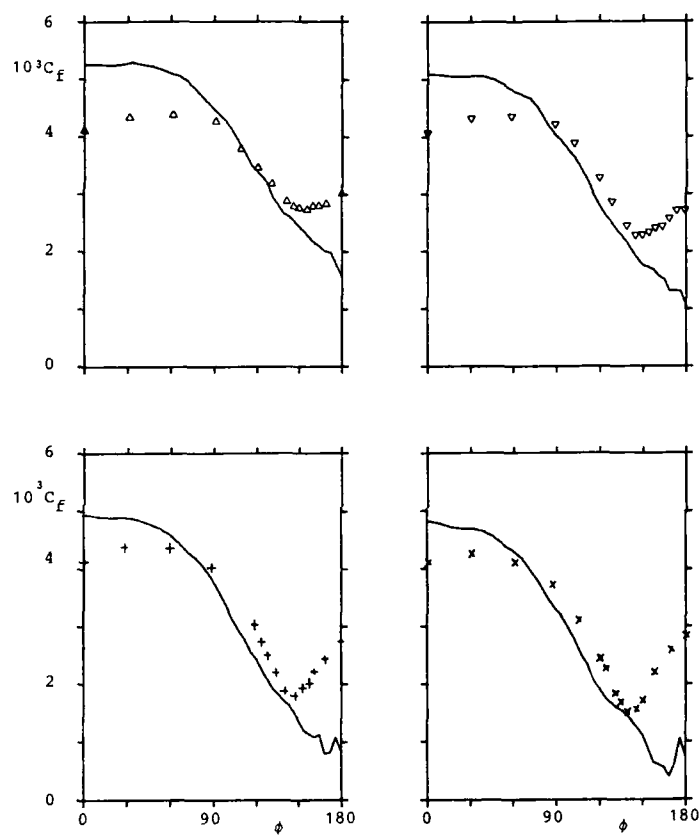
MOM LENGTH (HUMPHREYS, FFA)



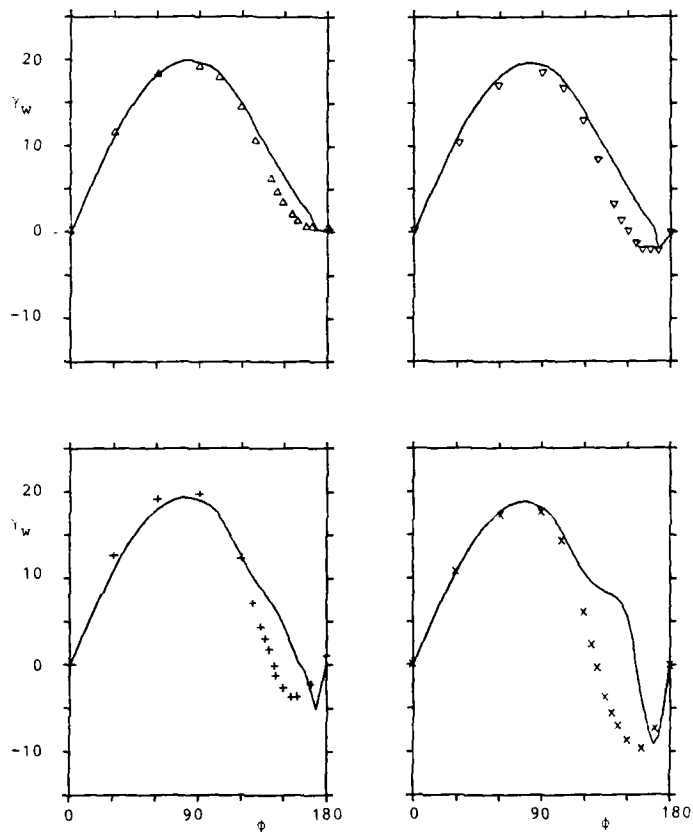
DISP LENGTH (HUMPHREYS, FFA)



FRIC COEF (HUMPHREYS, FFA)



FRIC ANGLE (HUMPHREYS, FFA)



MENTER, DFVLR

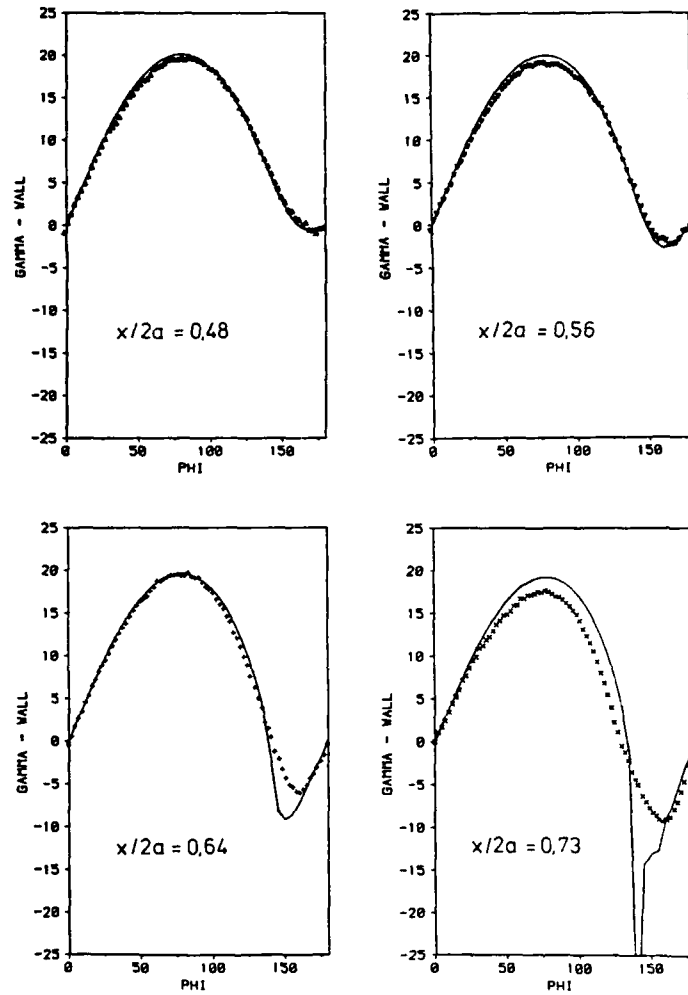


Fig. a1: Wall streamline angles at four different x-stations in comparison with experiments (potential pressure distribution)
 — computations

DFVLR

MEMTER, DFVLR

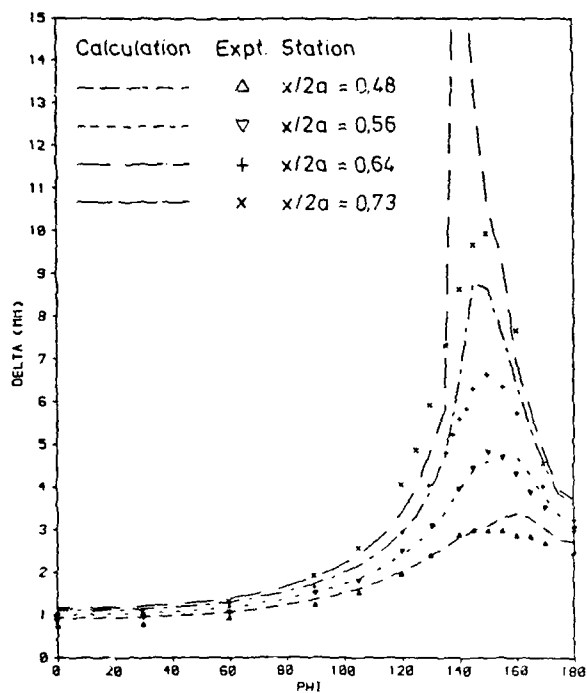


Fig. a2: Local displacement thicknesses at four different x-stations in comparison with experiments (potential pressure distribution)

DFVLR

MENTER, DFVLR

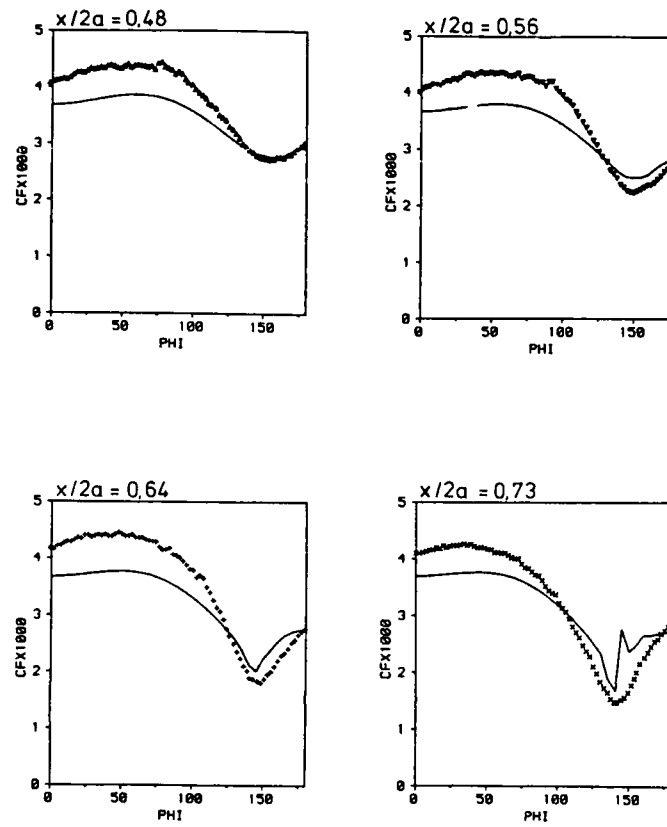


Fig. a3: Skin friction coefficient at four different x-stations in comparison with experiments (potential pressure distribution)

DFVLR

MENTER, DFVLR

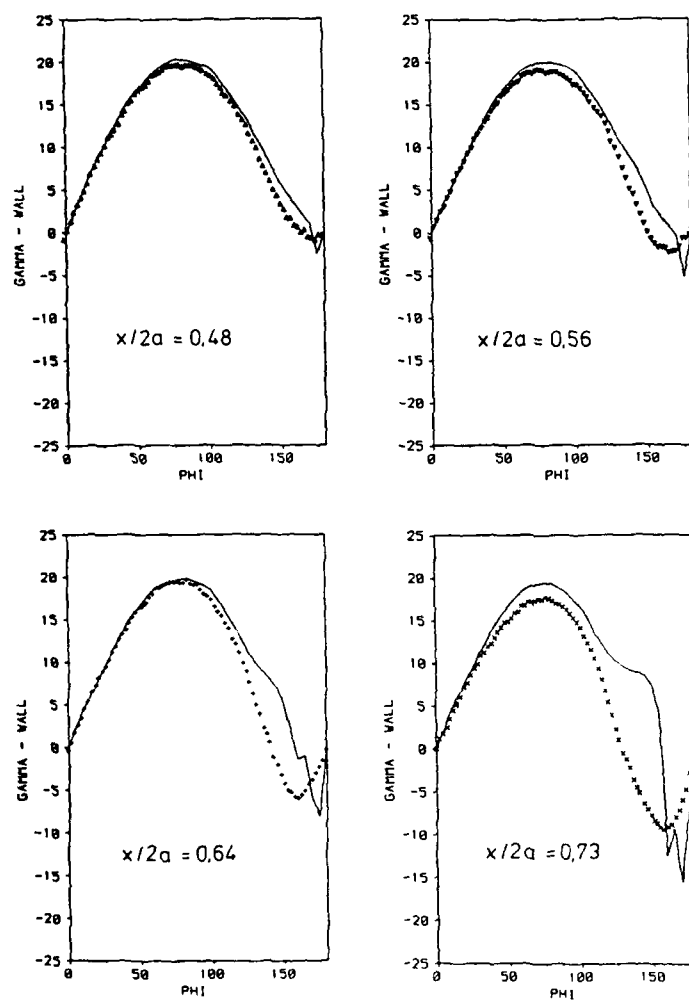


Fig. b1: Wall streamline angles at four different x -stations in comparison with experiments (boundary layer edge velocity computed by Stock)

DFVLR

MENTER, DFVLR

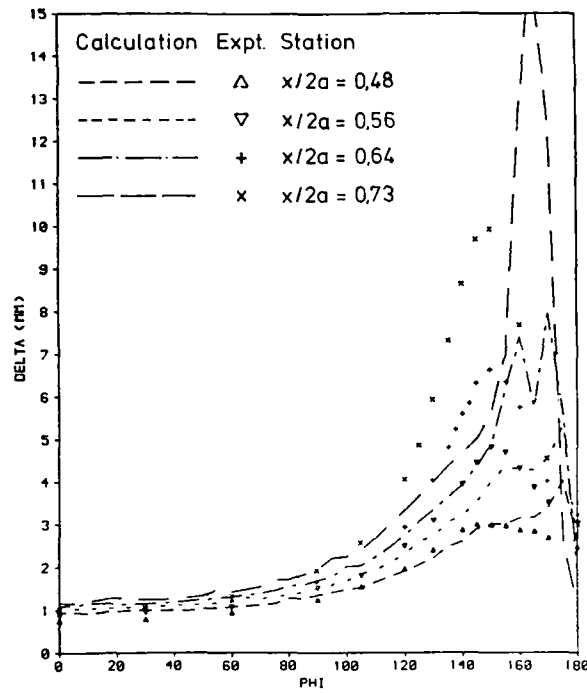


Fig. b2: Local displacement thicknesses at four different x-stations in comparison with experiments (boundary layer edge velocity computed by Stock)

DFVLR

MENTER, DFVLR

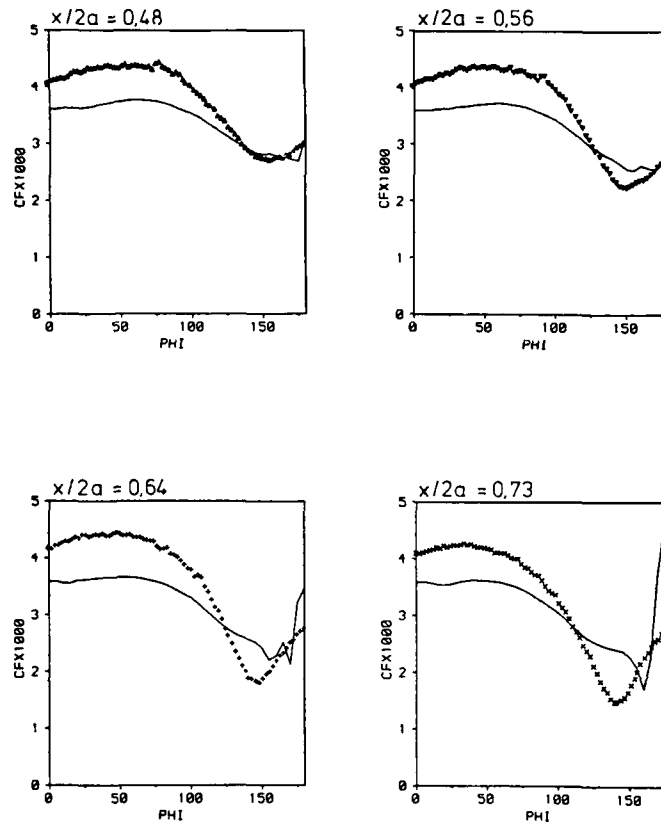


Fig. b3: Skin friction coefficient at four different x-stations in comparison with experiments (boundary layer edge velocity computed by Stock)

DFVLR

MENTER, DFVLR

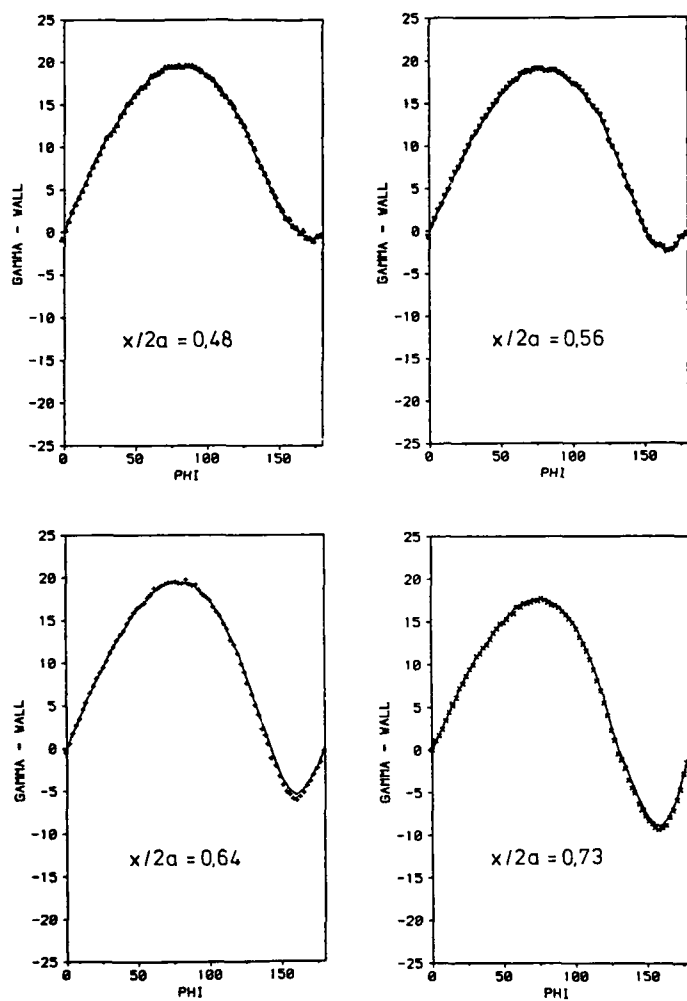


Fig. c1: Wall streamline angles at four different x -stations in comparison with experiments (Inverse boundary conditions)

DFVLR

MENTER, DFVLR

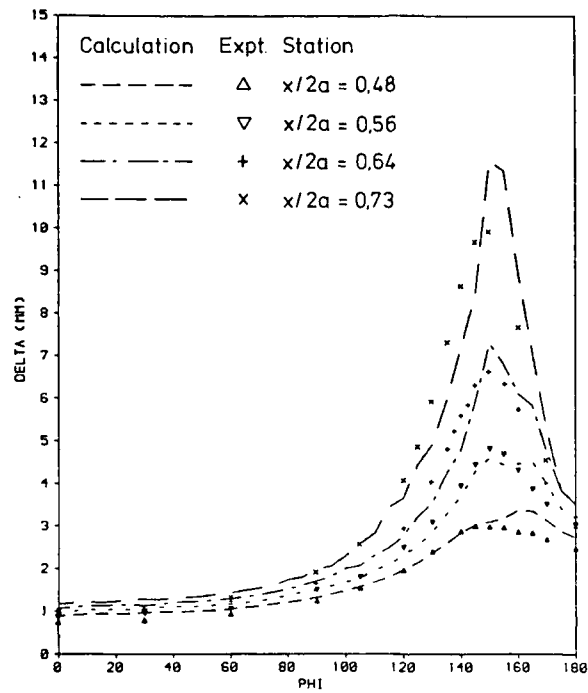


Fig. c2: Local displacement thicknesses at four different x-stations in comparison with experiments (Inverse boundary conditions)

DFVLR

MENTER, DFVLR

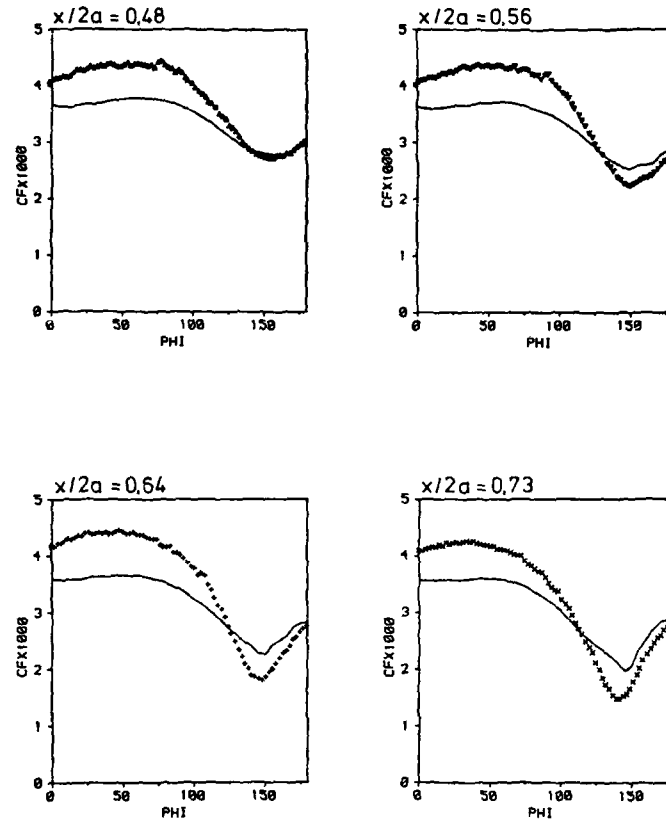


Fig. c3: Skin friction coefficient at four different x-stations in comparison with experiments (Inverse boundary conditions)

DFVLR

MENTER, DFVLR

DISPLACEMENT THICKNESS

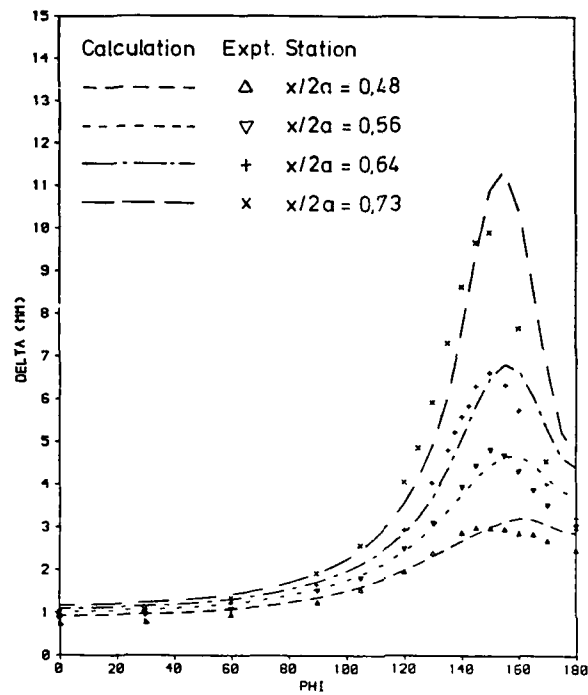


Fig. d2: Local displacement thicknesses at four different x-stations in comparison with experiments (with viscous-inviscid interaction)

DFVLR

MENTER, DFVLR

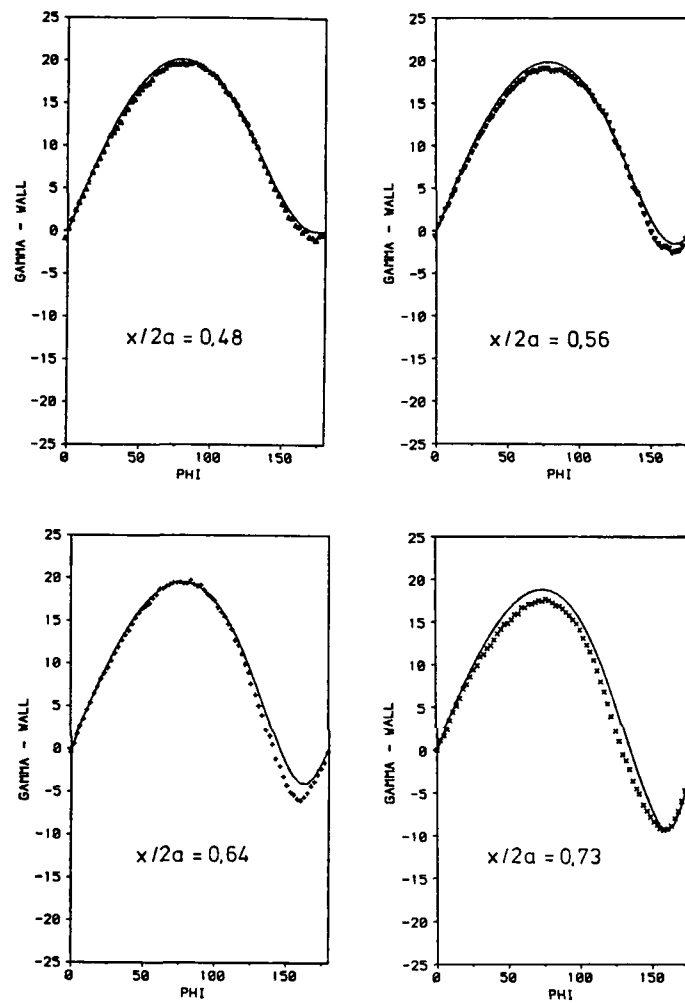


Fig. d1: Wall streamline angles at four different x-stations in comparison with experiments (with viscous-inviscid interaction)

DFVLR

MENTER, DFVLR

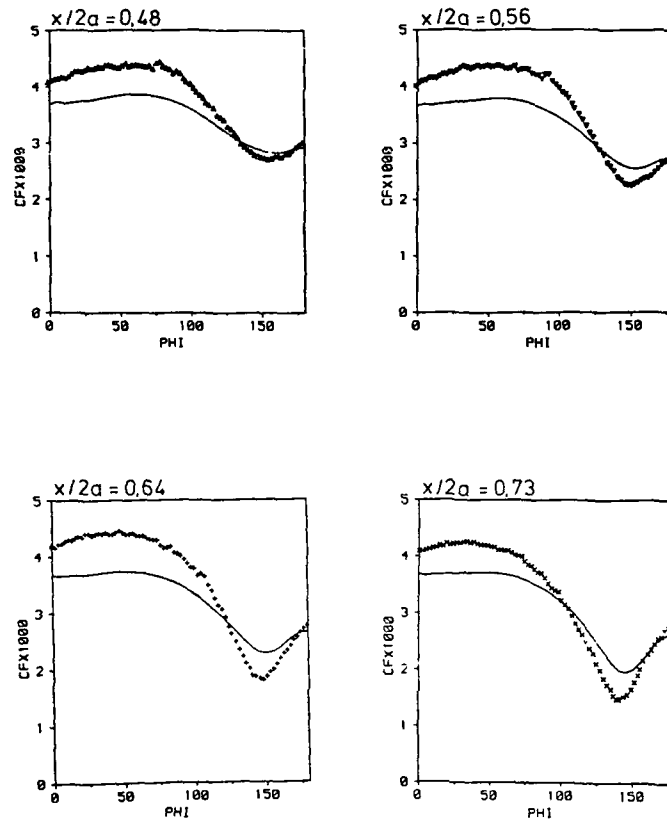
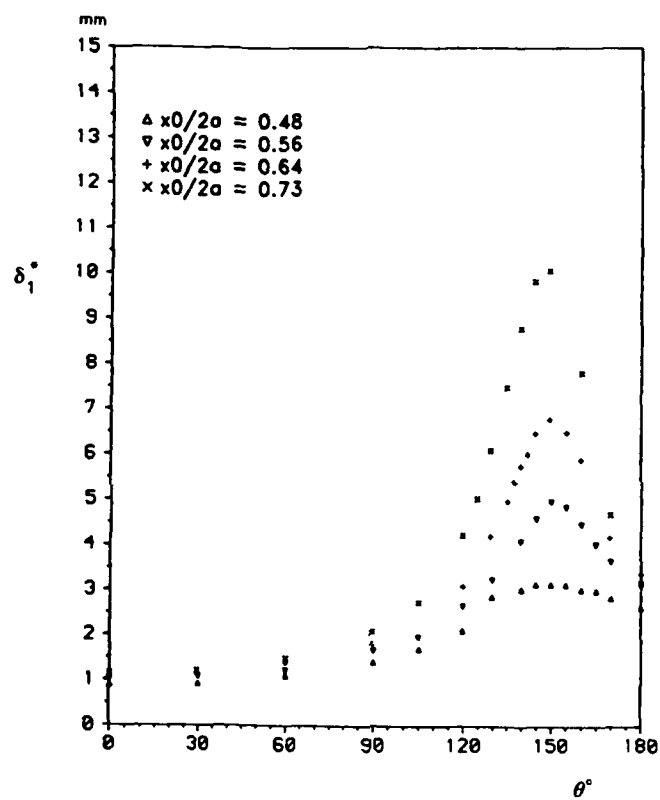


Fig. d3: Skin friction coefficient at four different x -stations in comparison with experiments (with viscous-inviscid interaction)

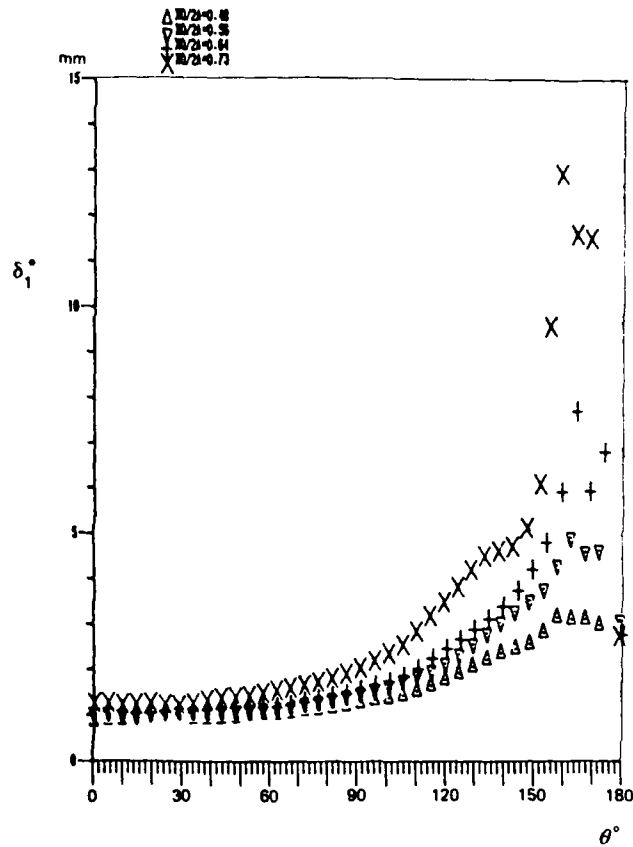
DFVLR

NLR RESULTS



Measured displacement thickness

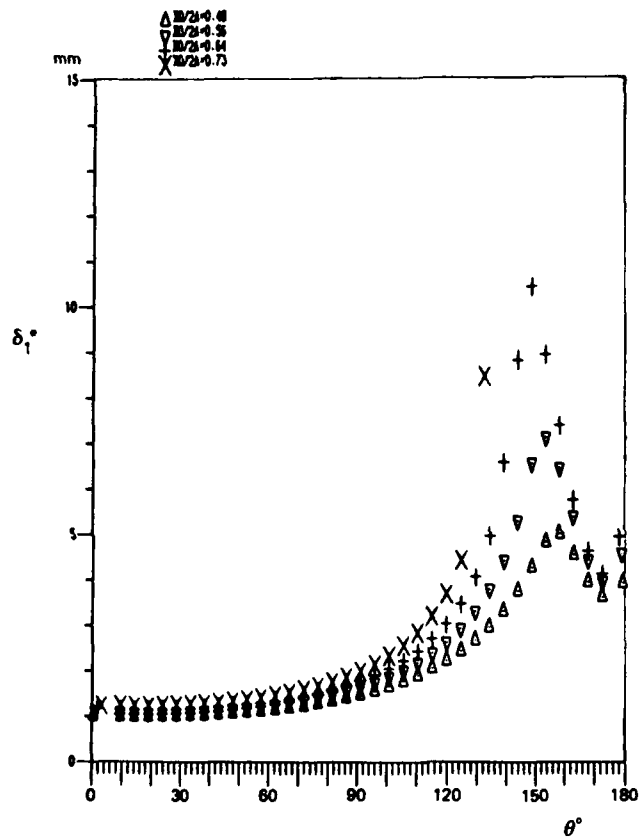
NLR RESULTS



Calculated displacement thickness

Case 1: Measured pressure distribution; initial conditions from Cebeci

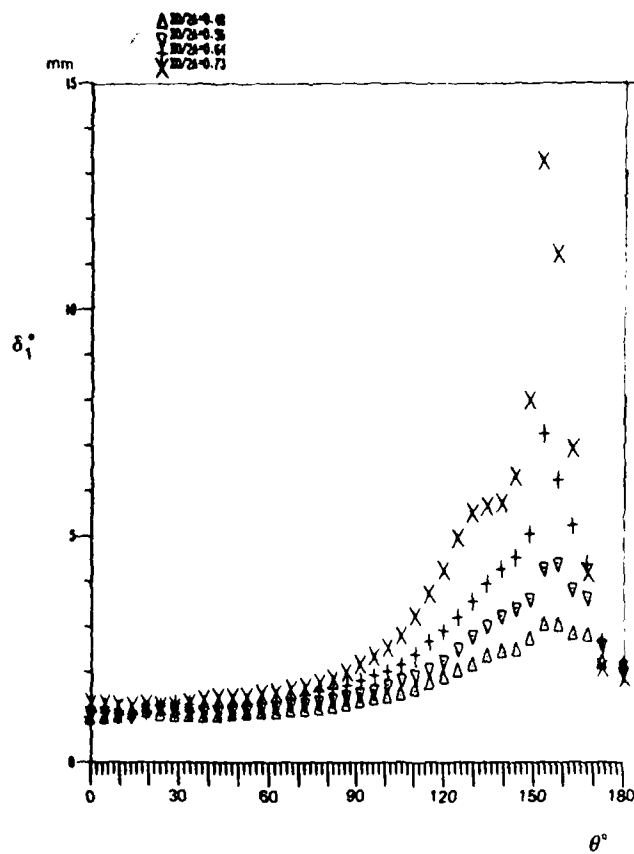
NLR RESULTS



Calculated displacement thickness

Case 2: Potential flow pressure distribution; initial conditions from
Cebeci

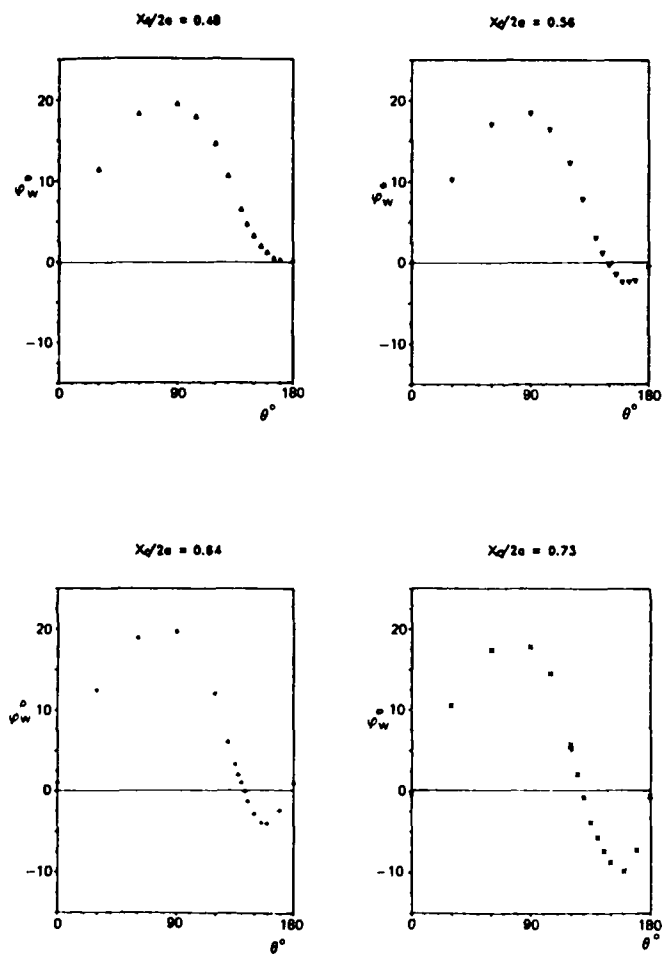
NLR RESULTS



Calculated displacement thickness

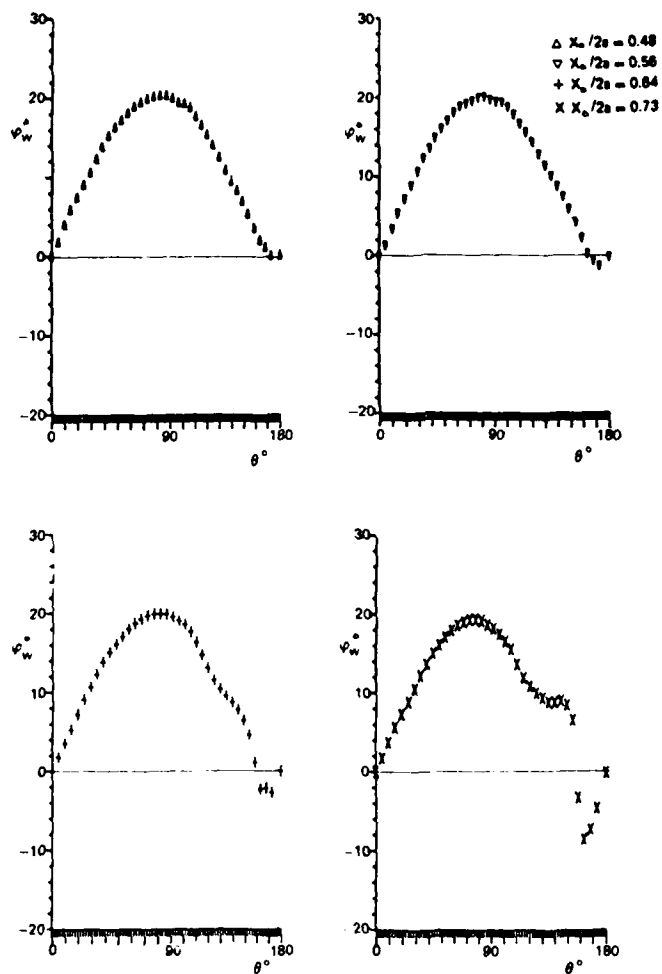
Case 3: Measured pressure distribution; initial conditions from Gleyzes

NLR RESULTS



Measured wall stream angle

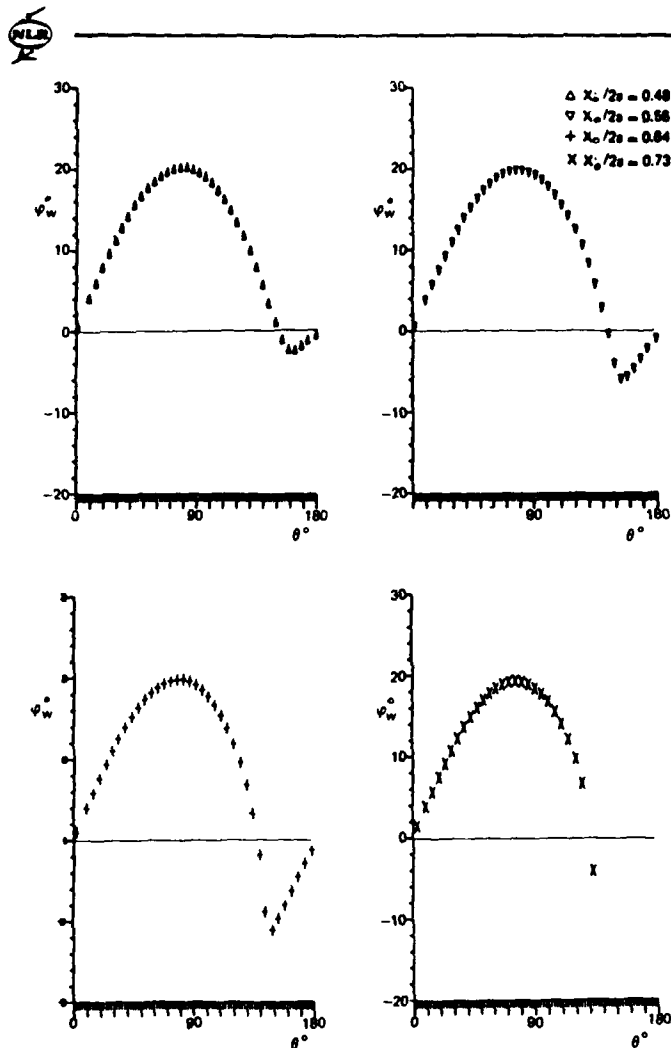
NLR RESULTS



Calculated wall stream angle

Case 1: Measured pressure distribution; initial conditions from Cebeci

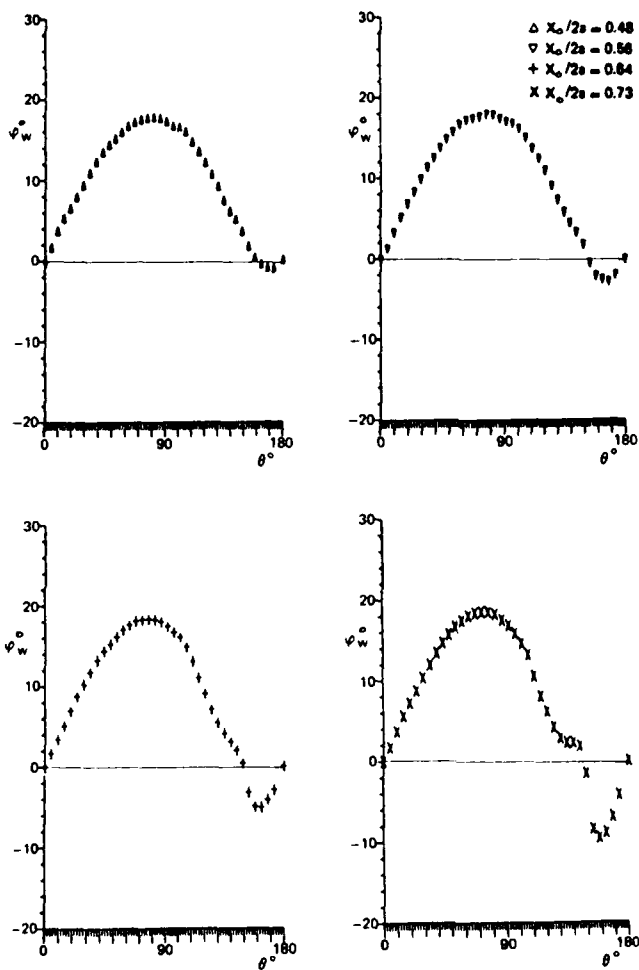
NLR RESULTS



Calculated wall stream angle

Case 2: Potential flow pressure distribution; initial conditions from Cebeci

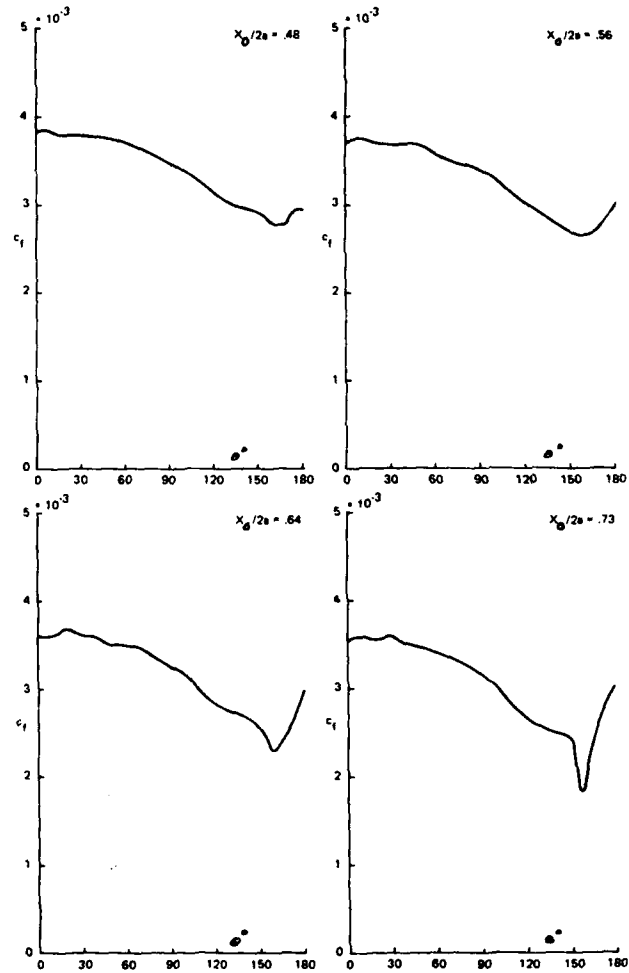
NLR RESULTS



Calculated wall stream angle

Case 3: Measured pressure distribution; initial conditions from Gleyzes

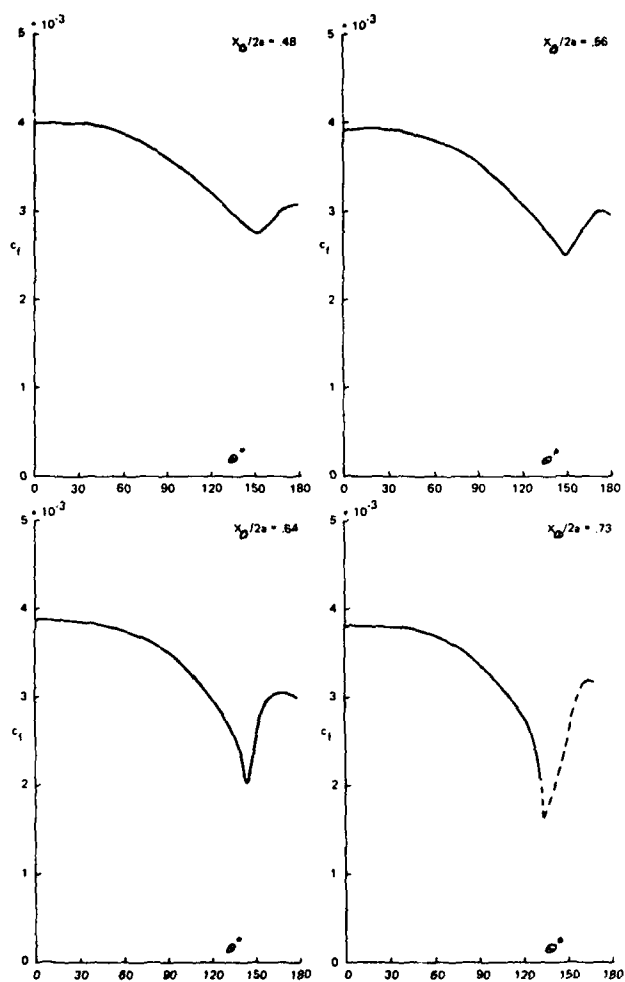
NLR RESULTS



Calculated skin friction coefficient

Case 1: Measured pressure distribution; initial conditions from Cebeci

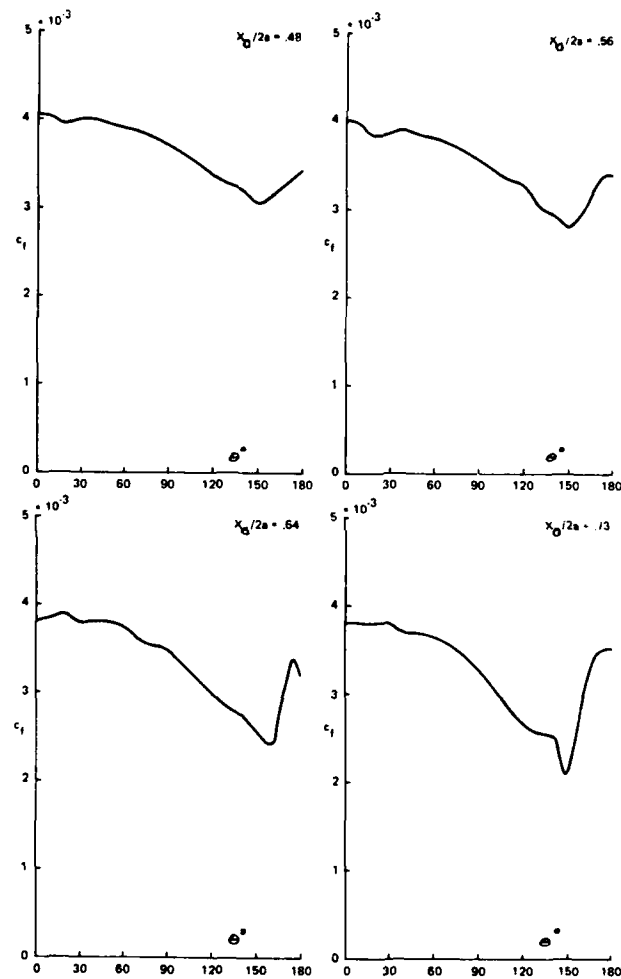
NLR RESULTS



Calculated skin friction coefficient

Case 2: Potential flow pressure distribution; initial conditions from Cebeci

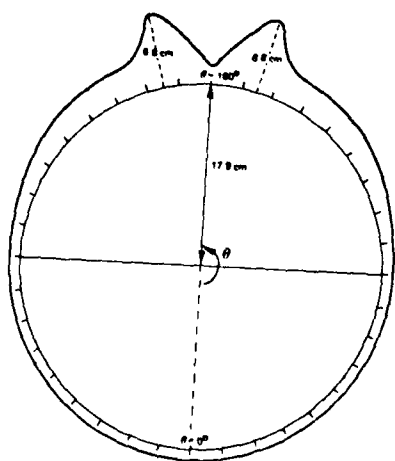
NLR RESULTS



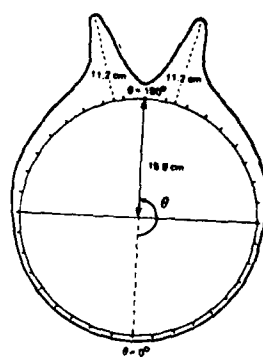
Calculated skin friction coefficient

Case 3: Measured pressure distribution; initial conditions from Gleyzes

NLR RESULTS

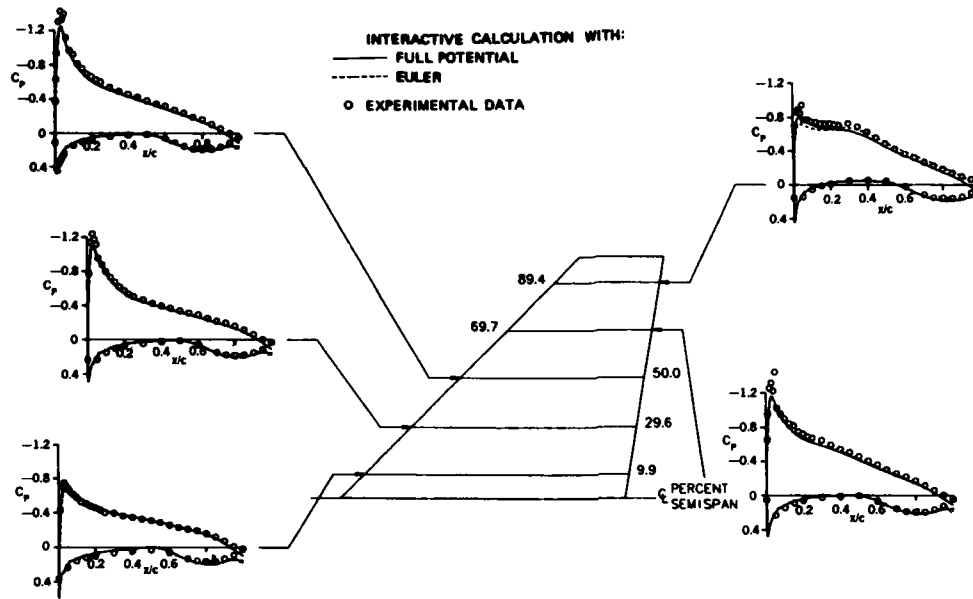


$$x_D/2a = 0.73$$

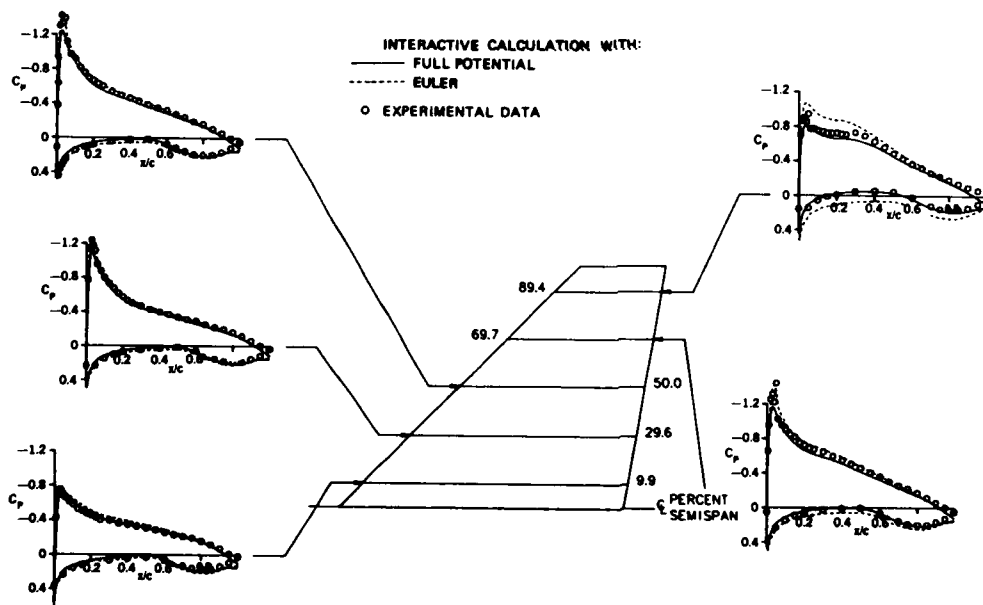


$$x_D/2a = 0.80$$

Calculated boundary layer thickness



(a)



(b)

Figure 2. Comparison of calculated and experimental chordwise pressure distributions for $M_\infty = 0.70$, $Re = 6.8 \times 10^6$. (a) Euler with H-grid. (b) Euler with C-grid.

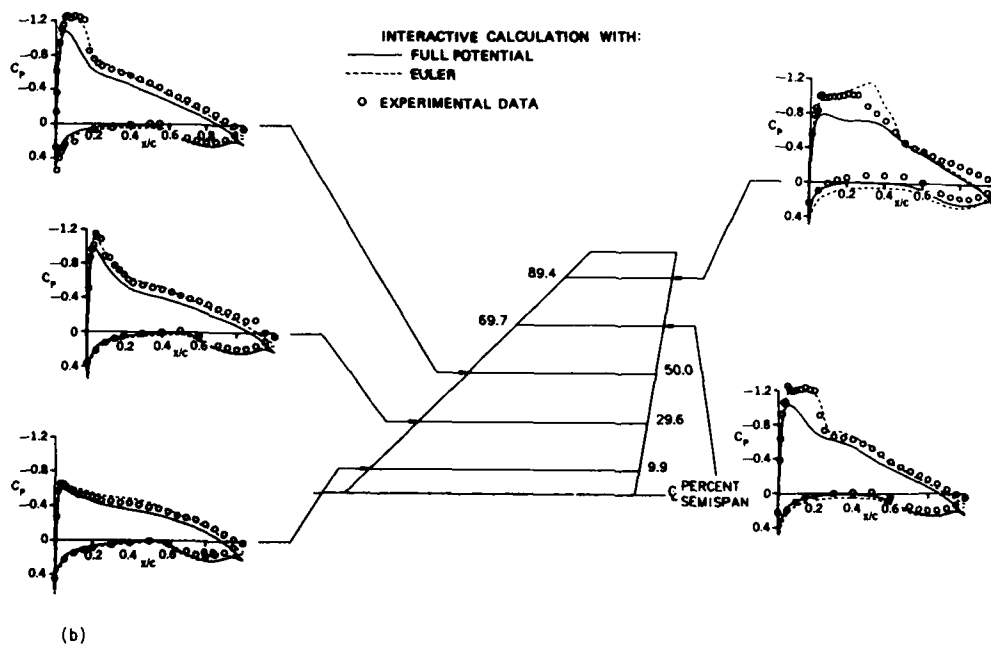
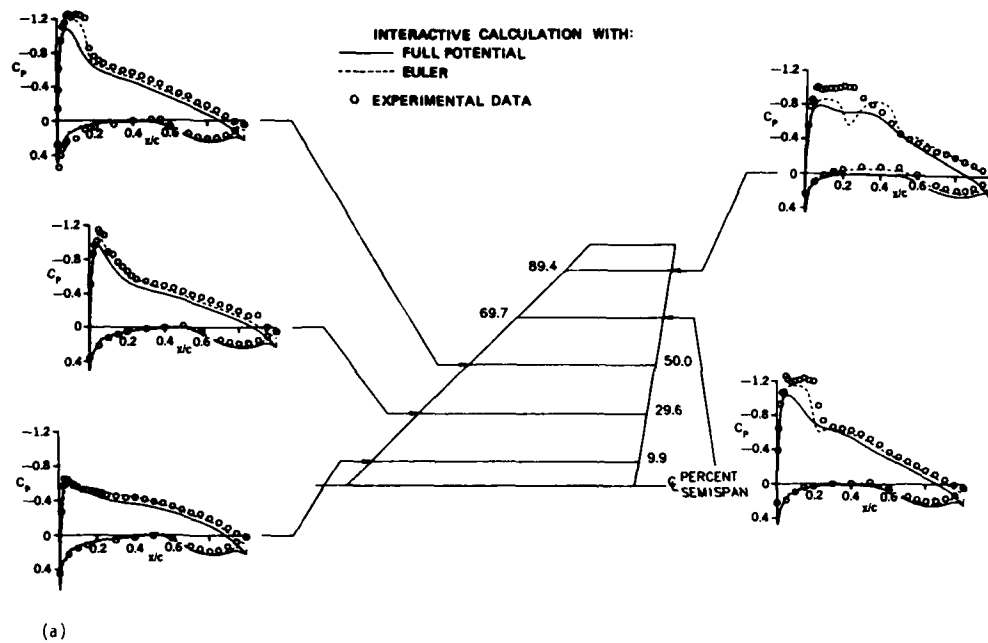


Figure 3. Comparison of calculated and experimental chordwise pressure distributions for $M_\infty = 0.82$, $Re = 6.8 \times 10^6$. (a) Euler with H-grid. (b) Euler with C-grid.

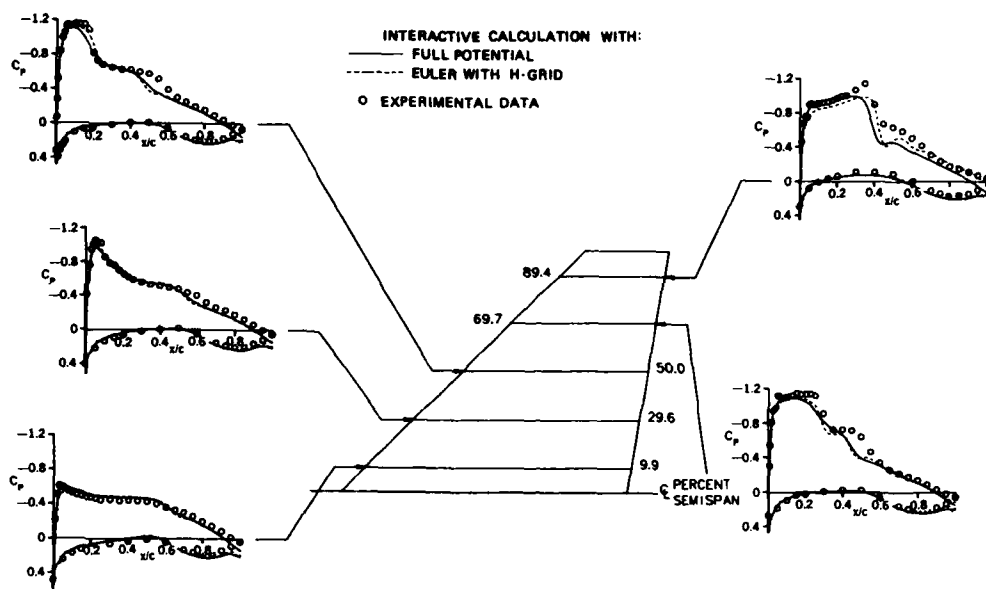


Figure 4. Comparison of calculated and experimental chordwise pressure distributions for $M_\infty = 0.85$, $Re = 6.8 \times 10^6$.

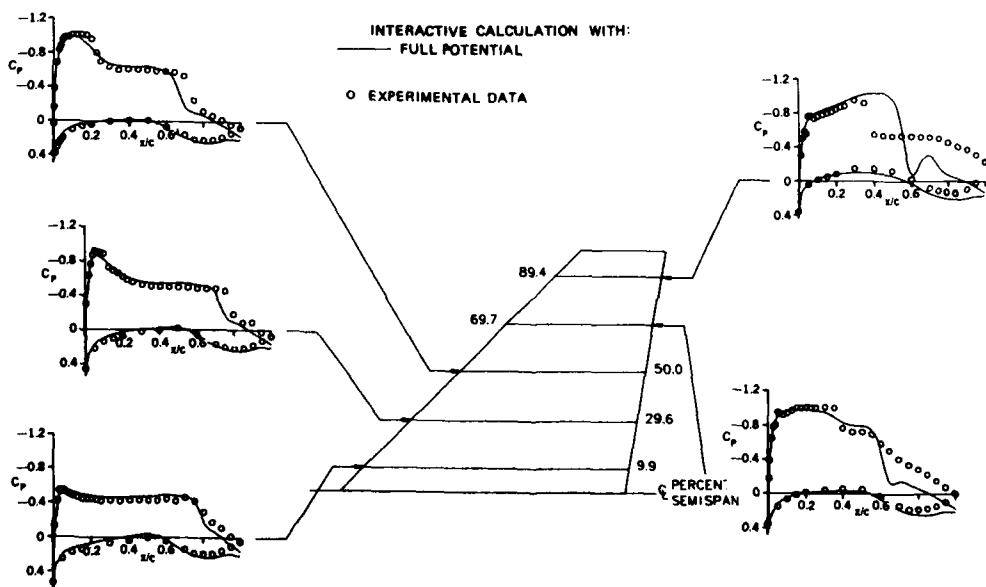


Figure 5. Comparison of calculated and experimental chordwise pressure distributions for $M_\infty = 0.90$, $Re = 6.8 \times 10^6$.

CHAPTER 7. CONCLUSIONS

The present study of the Working Group 10 was confined to turbulent flows using both the field and integral boundary layer equations. Two test cases were selected for numerical simulation, i.e. the DFVLR prolate spheroid and the NASA-Ames Wing C.

In order to give a brief summary of the results achieved some concluding remarks are listed below as stated by the various WG members:

- For the 10° prolate spheroid case, the boundary layer equations are valid, except in the regions of strong convergence of the wall streamlines.
- The 10° case is very sensitive to azimuthal distribution of the given external flow.
- Problems of definition of external flow lead to lack of agreement with experiment at 10° .
- Results very much dependent of edge conditions even at 10° .
- Boundary layer results for 30° agree better with Navier-Stokes results, perhaps because edge conditions and integral quantities are coherent (which is not evident for 10°).
- Wing C complicated by interference from root.
- 3-D boundary layer assumptions are very sensitive to external flow angles.
- Apply boundary layer theory only where it is valid, strong and global interaction should be handled by coupling approaches.
- For attached flow or for flow with mild cross flow separation, the viscous-inviscid interaction method is accurate and efficient and well suited for the design process. This is true for integral as well as for field methods.
- It seems that boundary layer calculations can go fairly far if proper boundary conditions are introduced.
- The initial aim was too ambitious.

From the last remark one can easily recommend a follow-up Working Group which would be useful if viscous/inviscid interaction methods are available. Furthermore, it is recommended to work on basic features of turbulent flow such as transition and turbulence modelling.

Appendix

NLR CALCULATIONS

J.I. van den Berg, J.P.F. Lindhout and B. van den Berg, National Aerospace Laboratory,
NLR, Anthony Fokkerweg 2, 1059 CM Amsterdam, The Netherlands

Calculations have been performed for one test case: The prolate spheroid at 10° angle of attack. The calculations have been carried out with BOLA, the NLR calculation system for three-dimensional boundary layers. The calculations were started at $x_0/2a = 0.30$ with given initial viscous flow conditions. As a boundary condition the surface pressure distribution was employed, the flow angle at the boundary layer edge being obtained from an integration of the Euler equations.

In a first report (J.I. van den Berg et al, 1987) grid dependence and the effect of changing the empirical constants in the turbulence model were investigated. Refinement of the grid was found to have little influence and the choice of slightly different constants in the turbulence model did not lead to essentially different results. In a second report (J.I. van den Berg et al, 1988) the influence of initial data and boundary conditions on the calculation results was investigated. Three calculations were performed and the results of these will be given in this appendix. The initial and boundary conditions for the three cases are:

- 1) Measured pressure distribution; initial flow conditions at $x_0/2a = 0.30$ from Cebeci (based on boundary layer calculations from the nose using the potential flow boundary condition).
- 2) Potential flow pressure distribution; initial flow conditions at $x_0/2a = 0.30$ from Cebeci.
- 3) Measured pressure distribution; initial flow conditions at $x_0/2a = 0.30$ from Gleyzes (different edge stream angles, obtained by fitting calculations to available measurement data at $x_0/2a = 0.48$).

The first case represents the initial and boundary conditions as defined for this test case by the Working Group.

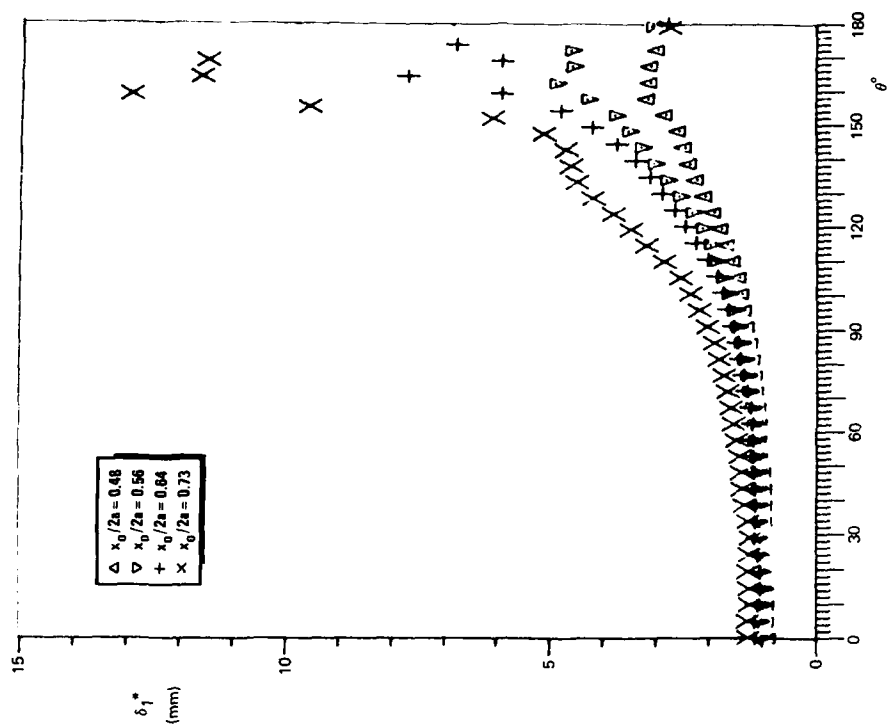
The calculation results for the three cases and the experimental data at the sections $x/2a = 0.48, 0.56, 0.64$ and 0.73 are plotted in a series of graphs appended. For the test case conditions defined by the Working Group (case 1), the calculation results are seen to compare not well with experiment at the leeward side of the prolate spheroid. The region of flow convergence is predicted essentially too close to the symmetry line. The calculations with the same initial conditions and the potential flow pressure distribution (case 2) produce results in much better agreement with experiment, though the displacement thickness peak is substantially overestimated. Comparatively smooth results are obtained, probably because the initial and boundary conditions used are smooth and compatible. Best overall agreement is obtained when the measured pressure distribution is used together with initial edge flow angles derived indirectly from the measurements (case 3).

It is concluded that the test case is dominated to a great extent by the boundary and initial conditions. More specifically boundary and initial conditions can probably not be prescribed independently. The poor results for case 1 seem to be due to prescribing the measured pressure distribution together with initial edge stream angles from potential flow. The solution of the Euler equations downstream of the initial line will lead then to an essentially wrong edge stream angle distribution.

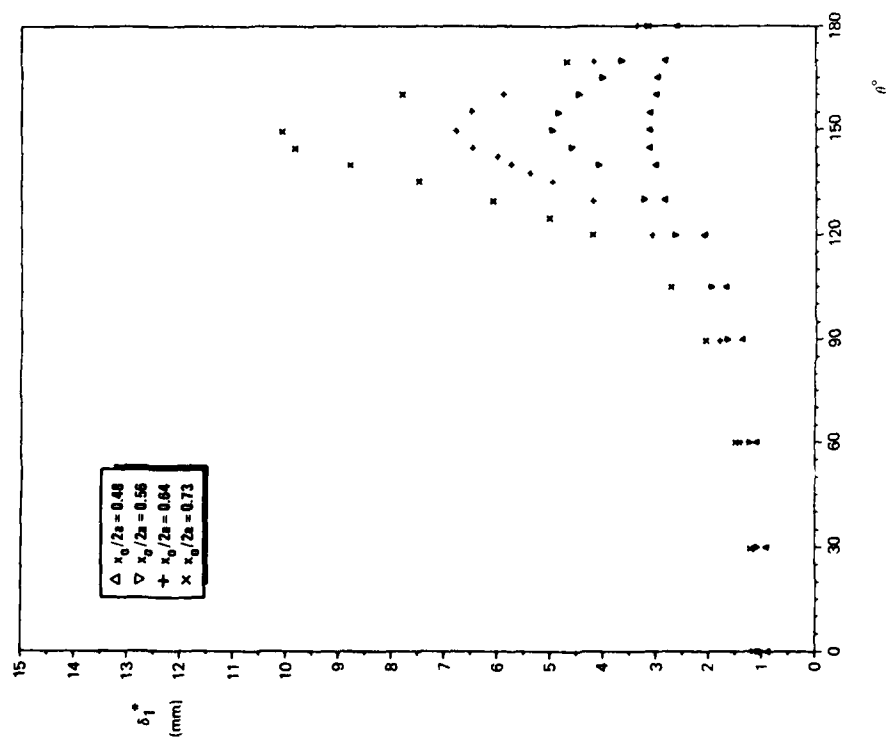
The objective of the Working Group is to determine the limits of boundary layer calculation procedures in 3D separation regions. The last figure shows the computed boundary layer thickness distribution at two sections in the rear part of the prolate spheroid. No problems were encountered in performing the boundary layer calculations, but the large circumferential thickness variations indicate that the boundary layer approximation (comparatively large derivatives normal to the surface) does not hold anymore and determines the limit here.

REFERENCES

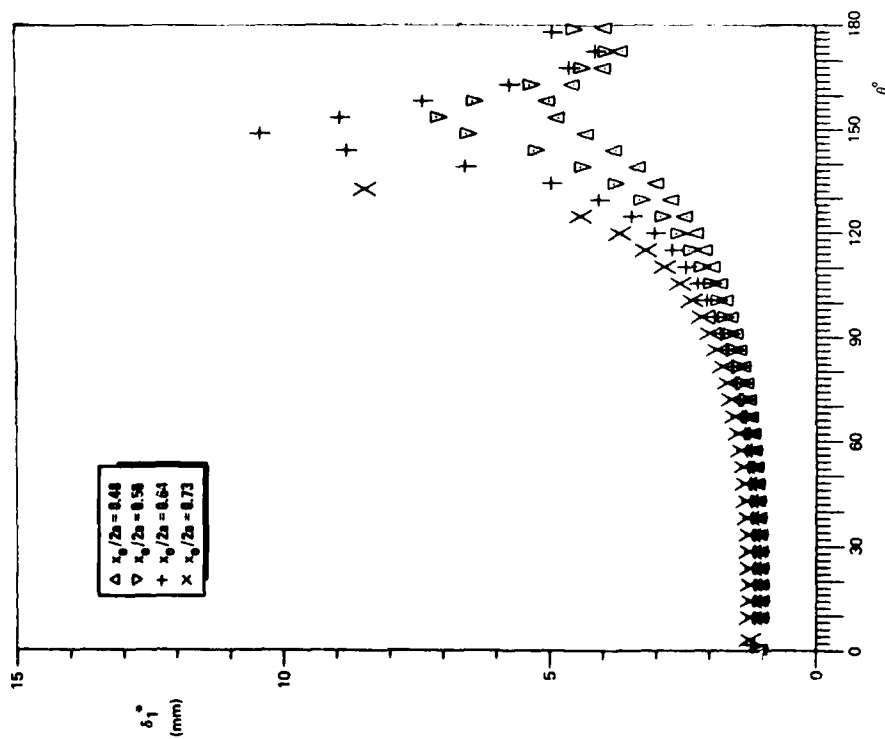
1. Berg, J.I. van den, Lindhout, J.P.F., Berg, B. van den, 1987. "Calculation of the boundary layer around an ellipsoid at 10° angle of attack". NLR MP 87026 U.
2. Berg, J.I. van den, Lindhout, J.P.F., Berg, B. van den, 1988. "Comparison of calculations of the boundary layer along a 1:6 ellipsoid at 10° angle of attack" NLR Memorandum IN-88-005 U.



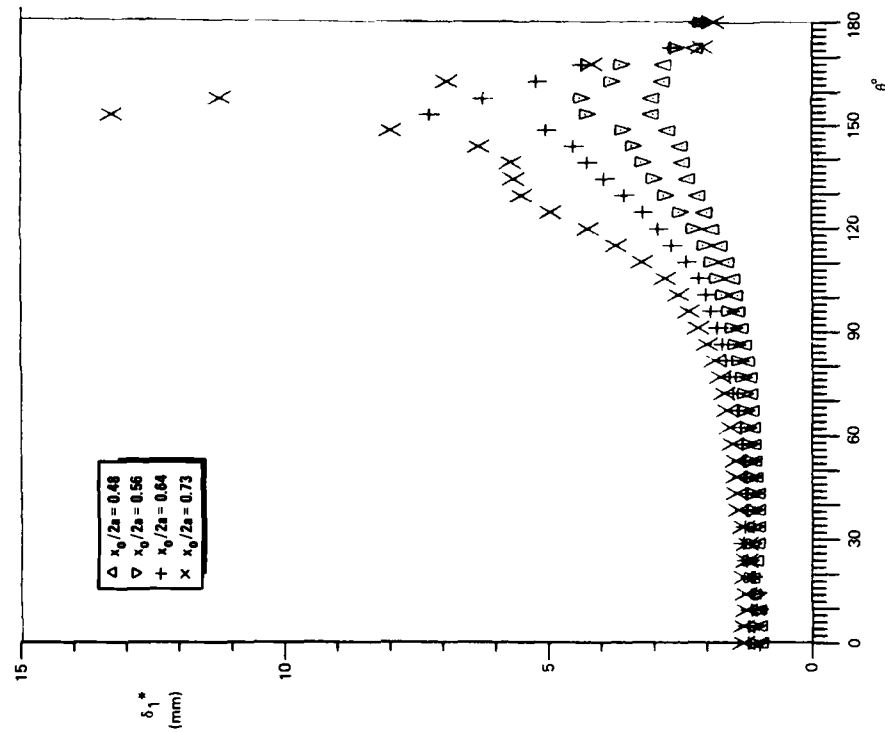
Calculated displacement thickness, NLR BOLA method
 Case 1: Measured pressure distribution; initial conditions from Cebeci



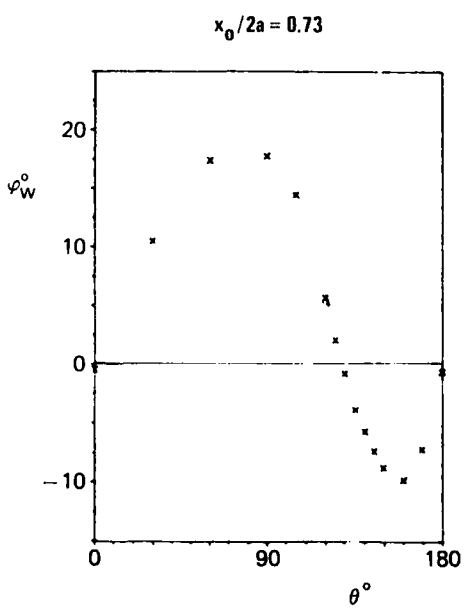
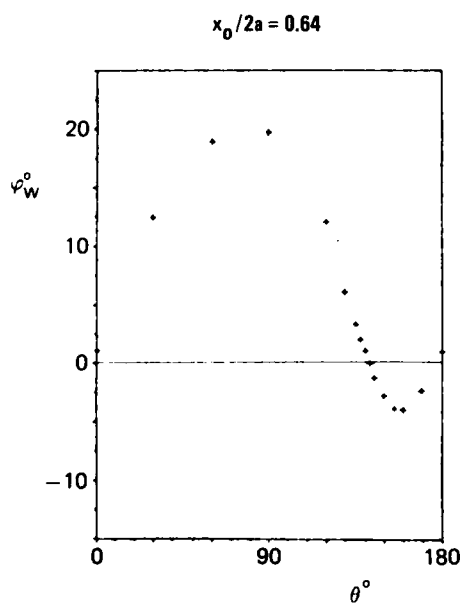
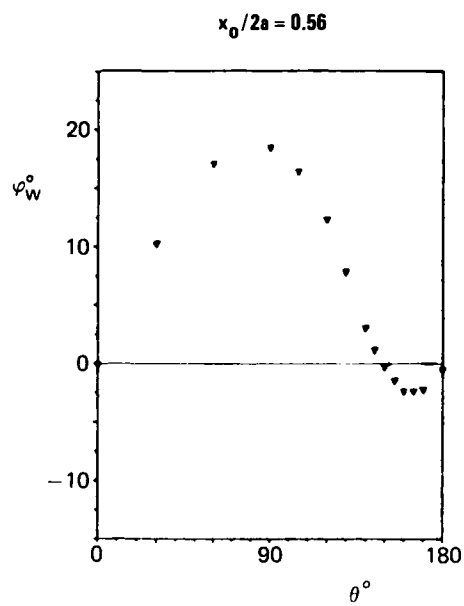
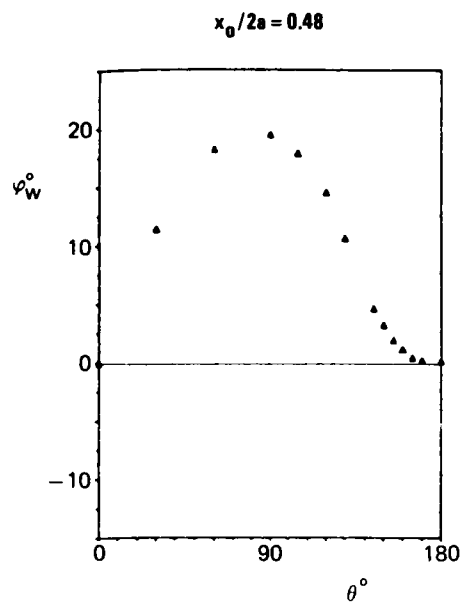
Measured displacement thickness



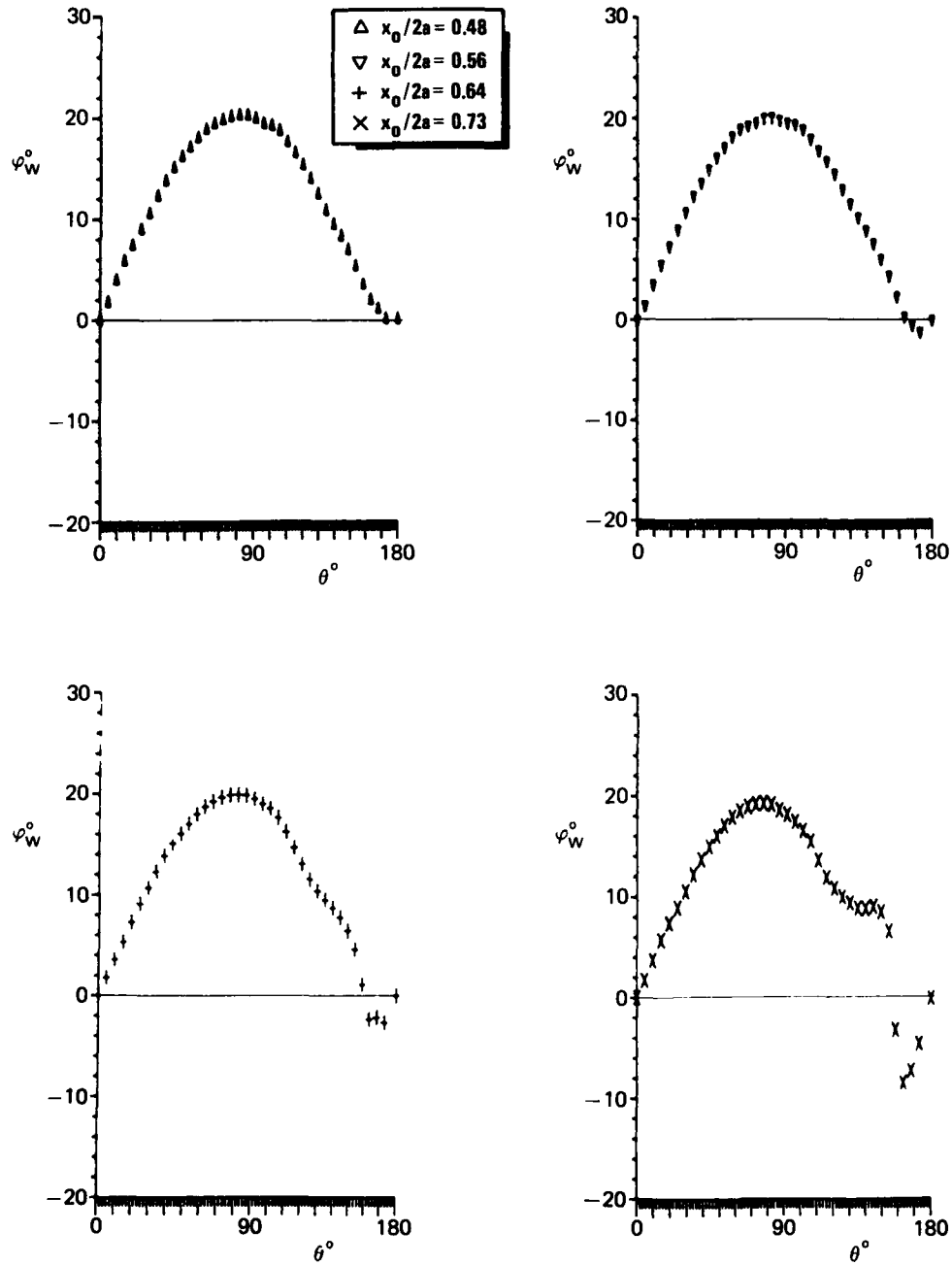
Calculated displacement thickness. NLR BOLA method
Case 2: Potential flow pressure distribution; initial conditions from Gebeci



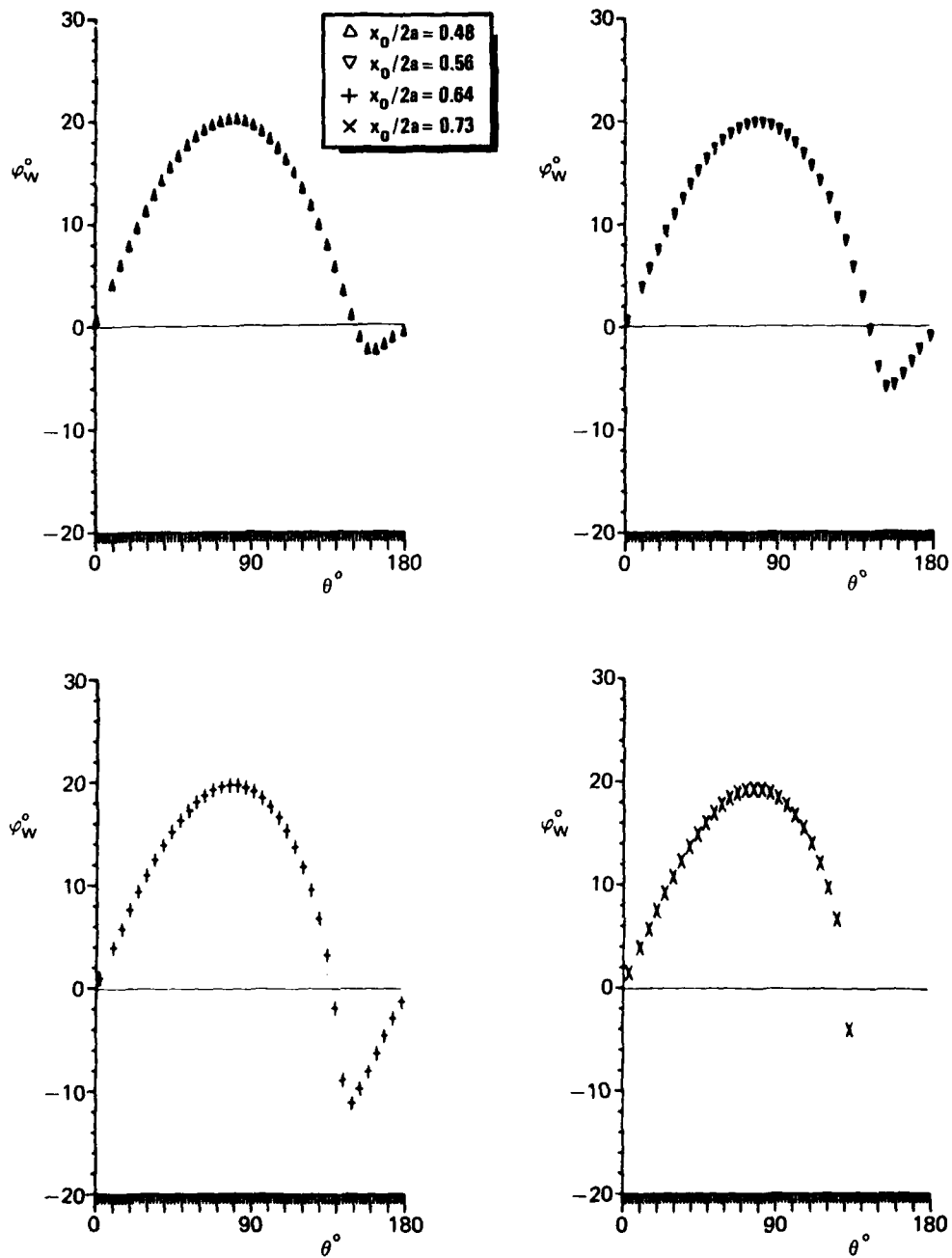
Calculated displacement thickness. NLR BOLA method
Case 3: Measured pressure distribution; initial conditions from Gleyzes



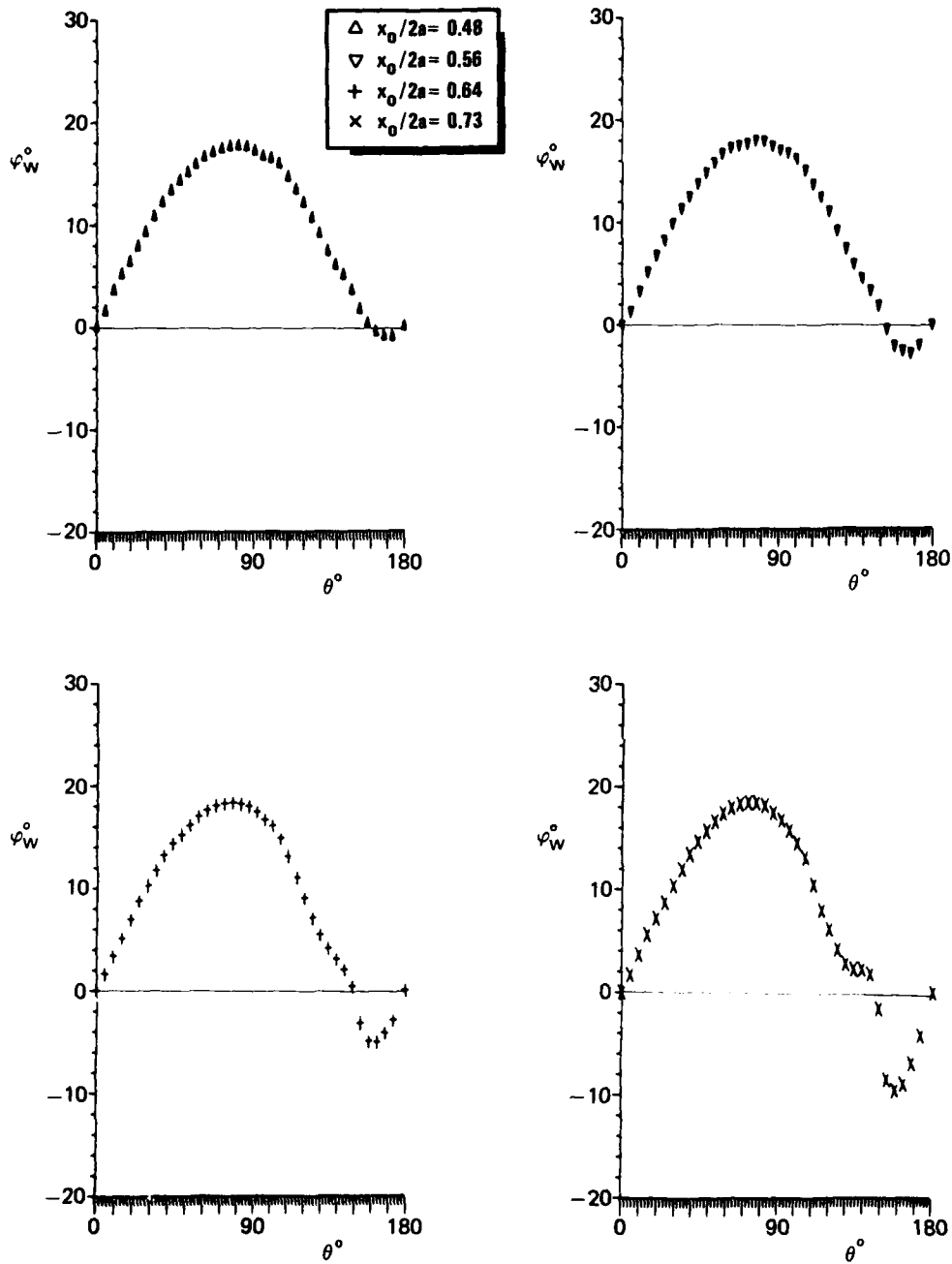
Measured wall stream angle



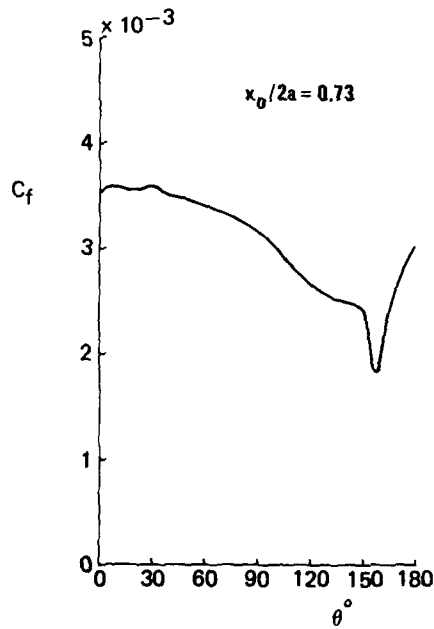
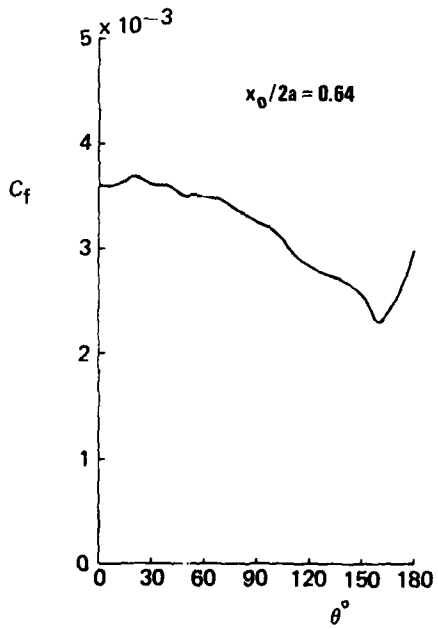
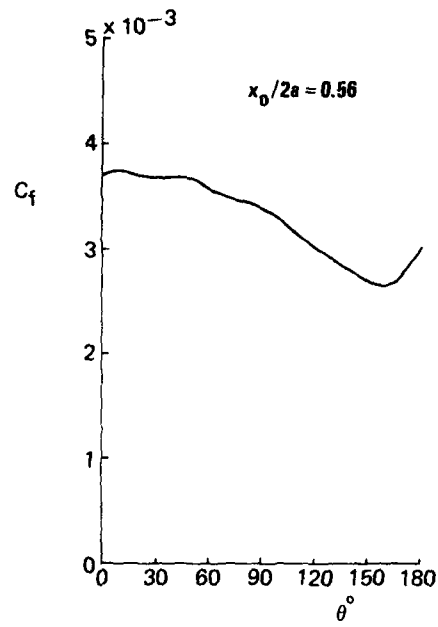
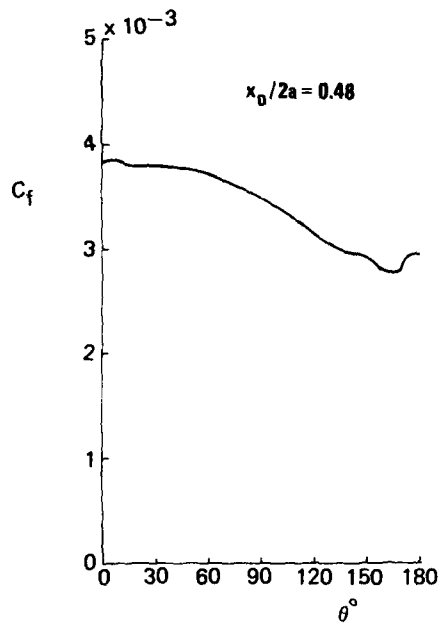
Calculated wall stream angle. NLR BOLA method
 Case 1: Measured pressure distribution; initial conditions from Cebeci



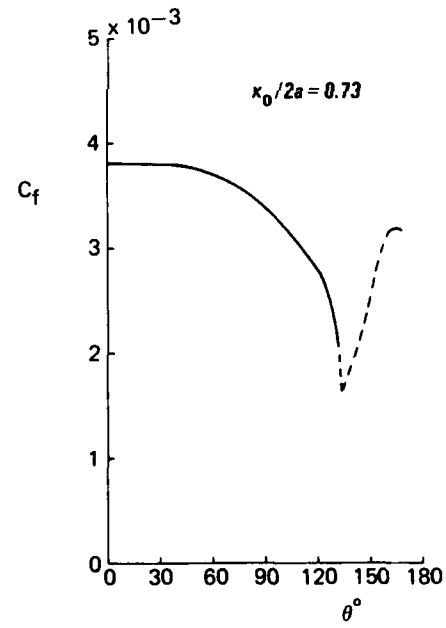
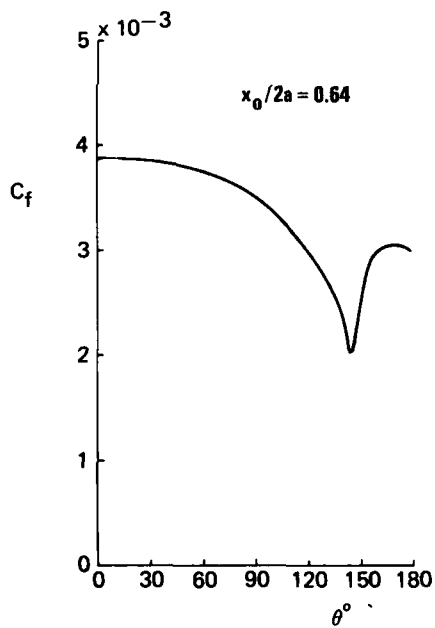
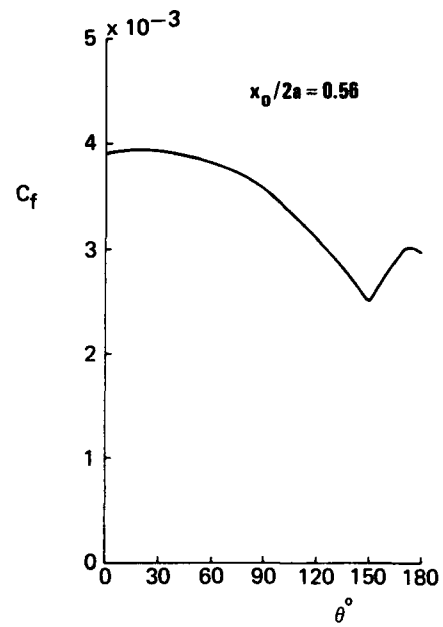
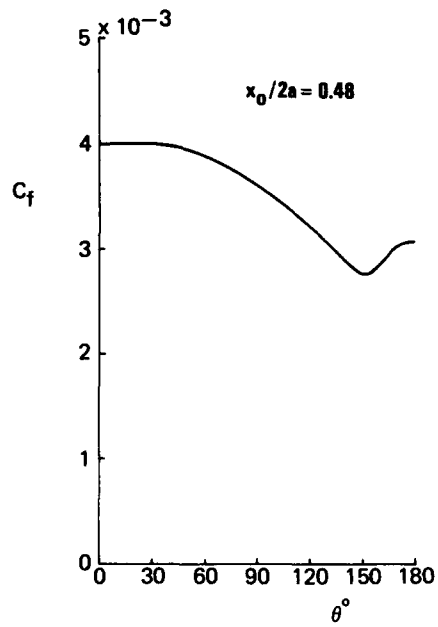
Calculated wall stream angle. NLR BOLA method
 Case 2: Potential flow pressure distribution; initial conditions from Cebeci



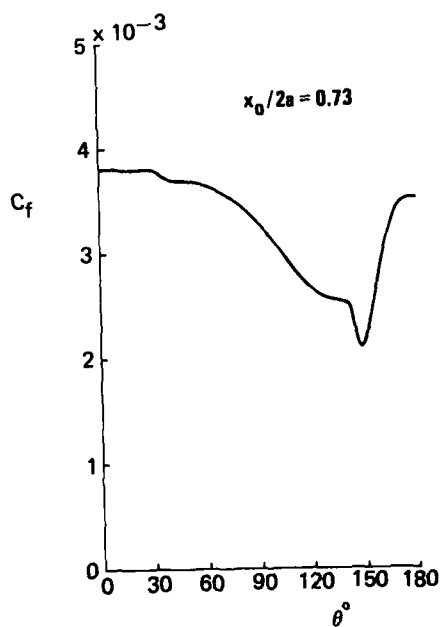
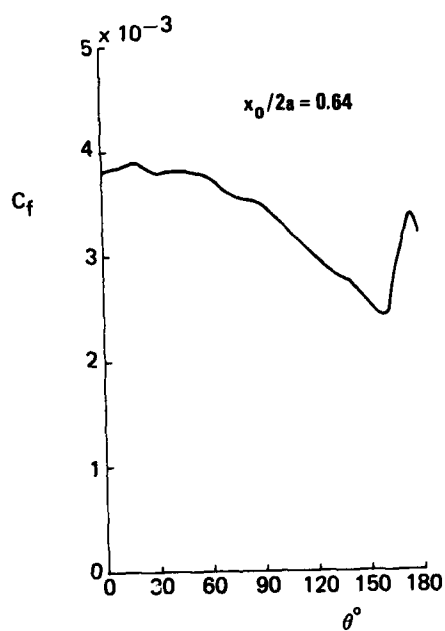
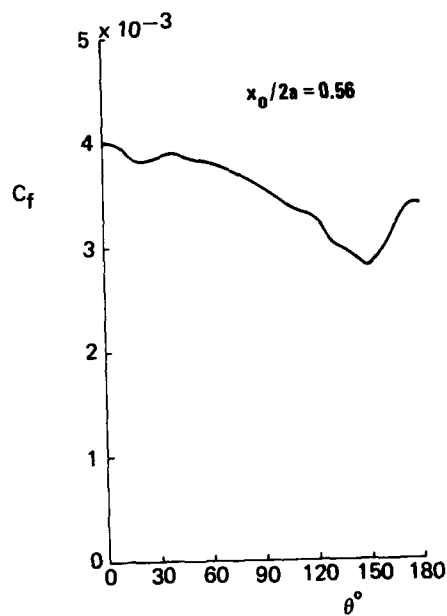
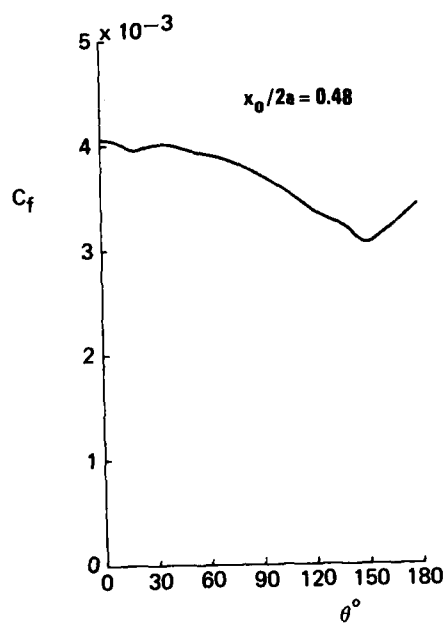
Calculated wall stream angle. NLR BOLA method
 Case 3: Measured pressure distribution; initial conditions from Gleyzes



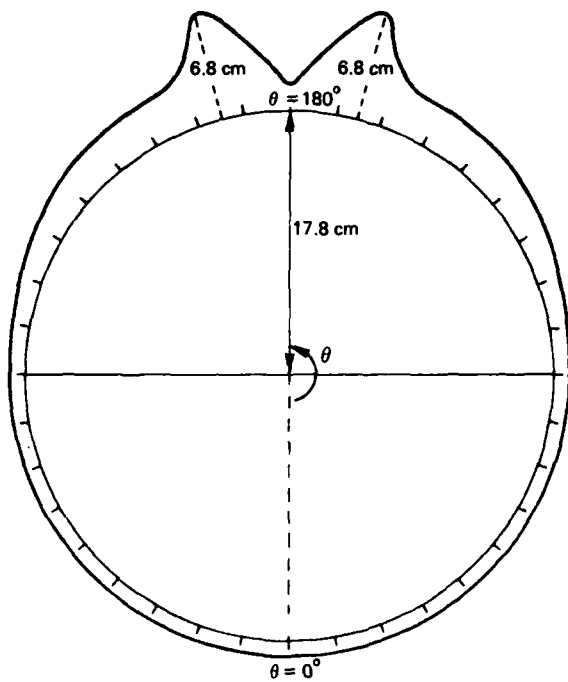
Calculated skin friction coefficient, NLR BOLA method
 Case 1: Measured pressure distribution; initial conditions from Cebeci



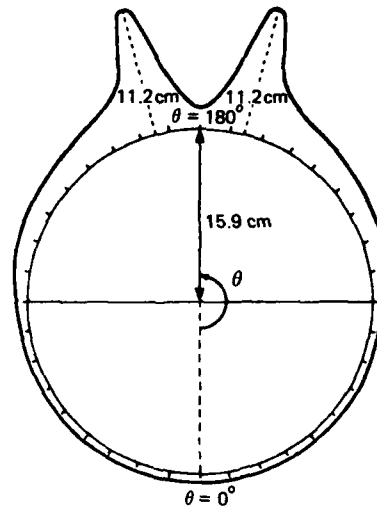
Calculated skin friction coefficient, NLR BOLA method
 Case 2: Potential flow pressure distribution; initial conditions from Cebeci



Calculated skin friction coefficient, NLR BOLA method
 Case 3: Measured pressure distribution; initial conditions from Gleyzes



$$x_0/2a = 0.73$$



$$x_0/2a = 0.80$$

Calculated boundary layer thickness. NLR BOLA method

170

REPORT DOCUMENTATION PAGE			
1. Recipient's Reference	2. Originator's Reference	3. Further Reference	4. Security Classification of Document
	AGARD-AR-255	ISBN 92-835-0560-3	UNCLASSIFIED
5. Originator	Advisory Group for Aerospace Research and Development North Atlantic Treaty Organization 7 rue Ancelle, 92200 Neuilly sur Seine, France		
6. Title	CALCULATION OF 3D SEPARATED TURBULENT FLOWS IN BOUNDARY LAYER LIMIT		
7. Presented at			
8. Author(s)/Editor(s) Various			9. Date May 1990
10. Author's/Editor's Address Various			11. Pages 144
12. Distribution Statement	This document is distributed in accordance with AGARD policies and regulations, which are outlined on the Outside Back Covers of all AGARD publications.		
13. Keywords/Descriptors			
<div style="display: flex; justify-content: space-between;"> <div> Boundary layer Turbulent flow Boundary layer separation </div> <div> Three dimensional flow; Computation </div> </div>			
14. Abstract			
<p>This report contains the results of a study conducted by Working Group 10 of the AGARD Fluid Dynamics Panel to investigate the limits of boundary layer methods, both the integral and field type formulations, for calculating three-dimensional turbulent separated flows. Test cases used to assess the boundary layer calculations included the DFVLR prolate spheroid at angle of attack and the NASA-Ames Wing C. Comparisons between boundary layer calculations and experimental data are presented for these test cases along with observations, conclusions and recommendations.</p>			

<p>AGARD Advisory Report No.255 Advisory Group for Aerospace Research and Development, NATO CALCULATION OF 3D SEPARATED TURBULENT FLOWS IN BOUNDARY LAYER LIMIT Published May 1990 144 pages</p> <p>This report contains the results of a study conducted by Working Group 10 of the AGARD Fluid Dynamics Panel to investigate the limits of boundary layer methods, both the integral and field type formulations, for calculating three-dimensional turbulent separated flows. Test cases used to assess the boundary layer calculations included the DFVLR prolate spheroid at angle of attack and the</p> <p>P.T.O.</p>	<p>AGARD-AR-255</p> <p>Boundary layer Turbulent flow Boundary layer separation Three dimensional flow Computation</p>	<p>AGARD Advisory Report No.255 Advisory Group for Aerospace Research and Development, NATO CALCULATION OF 3D SEPARATED TURBULENT FLOWS IN BOUNDARY LAYER LIMIT Published May 1990 144 pages</p> <p>This report contains the results of a study conducted by Working Group 10 of the AGARD Fluid Dynamics Panel to investigate the limits of boundary layer methods, both the integral and field type formulations, for calculating three-dimensional turbulent separated flows. Test cases used to assess the boundary layer calculations included the DFVLR prolate spheroid at angle of attack and the</p> <p>P.T.O.</p>	<p>AGARD-AR-255</p> <p>Boundary layer Turbulent flow Boundary layer separation Three dimensional flow Computation</p>
<p>AGARD Advisory Report No.255 Advisory Group for Aerospace Research and Development, NATO CALCULATION OF 3D SEPARATED TURBULENT FLOWS IN BOUNDARY LAYER LIMIT Published May 1990 144 pages</p> <p>This report contains the results of a study conducted by Working Group 10 of the AGARD Fluid Dynamics Panel to investigate the limits of boundary layer methods, both the integral and field type formulations, for calculating three-dimensional turbulent separated flows. Test cases used to assess the boundary layer calculations included the DFVLR prolate spheroid at angle of attack and the</p> <p>P.T.O.</p>	<p>AGARD-AR-255</p> <p>Boundary layer Turbulent flow Boundary layer separation Three dimensional flow Computation</p>	<p>AGARD Advisory Report No.255 Advisory Group for Aerospace Research and Development, NATO CALCULATION OF 3D SEPARATED TURBULENT FLOWS IN BOUNDARY LAYER LIMIT Published May 1990 144 pages</p> <p>This report contains the results of a study conducted by Working Group 10 of the AGARD Fluid Dynamics Panel to investigate the limits of boundary layer methods, both the integral and field type formulations, for calculating three-dimensional turbulent separated flows. Test cases used to assess the boundary layer calculations included the DFVLR prolate spheroid at angle of attack and the</p> <p>P.T.O.</p>	<p>AGARD-AR-255</p> <p>Boundary layer Turbulent flow Boundary layer separation Three dimensional flow Computation</p>

<p>NASA-Ames Wing C. Comparisons between boundary layer calculations and experimental data are presented for these test cases along with observations, conclusions and recommendations.</p> <p>ISBN 92-825-0560-3</p>	<p>NASA-Ames Wing C. Comparisons between boundary layer calculations and experimental data are presented for these test cases along with observations, conclusions and recommendations.</p> <p>ISBN 92-825-0560-3</p>
<p>NASA-Ames Wing C. Comparisons between boundary layer calculations and experimental data are presented for these test cases along with observations, conclusions and recommendations.</p> <p>ISBN 92-825-0560-3</p>	<p>NASA-Ames Wing C. Comparisons between boundary layer calculations and experimental data are presented for these test cases along with observations, conclusions and recommendations.</p> <p>ISBN 92-825-0560-3</p>

AGARD

NATO OTAN

**7 rue Ancelle • 92200 NEUILLY-SUR-SEINE
FRANCE**

Telephone (1)47.38.57.00 • Telex 610 176

**DISTRIBUTION OF UNCLASSIFIED
AGARD PUBLICATIONS**

AGARD does NOT hold stocks of AGARD publications at the above address for general distribution. Initial distribution of AGARD publications is made to AGARD Member Nations through the following National Distribution Centres. Further copies are sometimes available from these Centres, but if not may be purchased in Microfiche or Photocopy form from the Sales Agencies listed below.

NATIONAL DISTRIBUTION CENTRES

BELGIUM

Coordonnateur AGARD - VSL
Etat-Major de la Force Aérienne
Quartier Reine Elisabeth
Rue d'Evere, 1140 Bruxelles

CANADA

Director Scientific Information Services
Dept of National Defence
Ottawa, Ontario K1A 0K2

DENMARK

Danish
Ved IC
2100

FRANCE

O.N.E.
29 Av
92320

GERMAN

Fach
Karl
D-75

GREECE

Helle
Air V
Scien
Deke
Deke

ICELAND

Dire
c/o Flugma
Reykjavik

ITALY

Aeronautica Militare
Ufficio del Delegato Nazionale all'AGARD
3 Piazzale Adenauer
00144 Roma/EUR

LUXEMBOURG

See Belgium

NETHERLANDS

Netherlands Delegation to AGARD
National Aerospace Laboratory, NLR
Kluyverweg 1
2629 HS Delft

NORWAY

Norwegian Defence Research Establishment
Attn: Biblioteket

Postage and Fees Paid
National Aeronautics and
Space Administration
NASA-461

Official Business
Penalty for Private Use \$300



GARD

NASA

National Aeronautics and
Space Administration

Washington, D.C.
20546

**SPECIAL FOURTH CLASS MAIL
BOOK**

L1 001 AGARDAR255900622S002672D
DEPT OF DEFENSE
DEFENSE TECHNICAL INFORMATION CENTER
DTIC-PDAD
CAMERON STATION BLDG 5
ALEXANDRIA VA 223046145

Glasgow G4 0CA

UNITED STATES

National Aeronautics and Space Administration (NASA)
Langley Research Center
M/S 180
Hampton, Virginia 23665

**THE UNITED STATES NATIONAL DISTRIBUTION CENTRE (NASA) DOES NOT HOLD
STOCKS OF AGARD PUBLICATIONS, AND APPLICATIONS FOR COPIES SHOULD BE MADE
DIRECT TO THE NATIONAL TECHNICAL INFORMATION SERVICE (NTIS) AT THE ADDRESS BELOW.**

SALES AGENCIES

National Technical
Information Service (NTIS)
5285 Port Royal Road
Springfield
Virginia 22161, USA

ESA/Information Retrieval Service
European Space Agency
10, rue Mario Nikis
75015 Paris, France

The British Library
Document Supply Centre
Boston Spa, Wetherby
West Yorkshire LS23 7BQ
England

Requests for microfiche or photocopies of AGARD documents should include the AGARD serial number, title, author or editor, and publication date. Requests to NTIS should include the NASA accession report number. Full bibliographical references and abstracts of AGARD publications are given in the following journals:

Scientific and Technical Aerospace Reports (STAR)
published by NASA Scientific and Technical
Information Branch
NASA Headquarters (NIT-40)
Washington D.C. 20546, USA

Government Reports Announcements (GRA)
published by the National Technical
Information Services, Springfield
Virginia 22161, USA

**Printed by Specialised Printing Services Limited
40 Chigwell Lane, Loughton, Essex IG10 3TZ**

ISBN 92-835-0560-3